Quantitative Photothermal Heating and Cooling Measurements of Engineered Nanoparticles in an Optical Trap

Paden Bernard Roder

A dissertation
submitted in partial fulfillment of the
requirements for the degree of

Doctor of Philosophy

University of Washington

2015

Reading Committee:

Peter J. Pauzauskie, Chair

E. James Davis

Miqin Zhang

Bruce J. Hinds

Program Authorized to Offer Degree:
Materials Science and Engineering

University of Washington

Abstract

Quantitative Photothermal Heating and Cooling Measurements of Engineered Nanoparticles in an Optical Trap

Paden Bernard Roder

Chair of the Supervisory Committee:
Prof. Dr. Peter J. Pauzauskie
Materials Science and Engineering

Laser tweezers and optical trapping has provided scientists and engineers a unique way to study the wealth of phenomena that materials exhibit at the micro- and nanoscale, much of which remains mysterious. Of particular interest is the interplay between light absorption and subsequent heat generation of laser-irradiated materials, especially due to recent interest in developing nanoscale materials for use as agents for photothermal cancer treatments. An introduction to optical trapping physics and laser tweezers are given in Chapter 1 and 2 of this thesis, respectively. The remaining chapters, summarized below, describe the theoretical basis of laser heating of one-dimensional nanostructures and experiments in which optically-trapped nanostructures are studied using techniques developed for a laser tweezer.

In Chapter 3, we delve into the fundamentals of laser heating of one-dimensional materials by developing an analytical model of pulsed laser heating of uniform and tapered supported nanowires and compare calculations with experimental data to comment on the effects that the material's physical, optical, and thermal parameters have on its heating and cooling rates. We then consider closed-form analytical solutions for the temperature rise within infinite circular cylinders with nanometer-scale diameters irradiated at right angles by TM-polarized continuous-wave laser sources, which allows for analysis of laser-heated nanowires in a solvated environment. The infinite nanowire analysis will then be extended to the optical

heating of laser-irradiated finite nanowires in the framework of a laser tweezer, which enables predictive capabilities and direct comparison with laser trapping experiments.

An effective method for determining optically-trapped particle temperatures as well as the temperature gradient in the surrounding medium will be discussed in Chapter 4. By combining laser tweezer calibration techniques, forward-scattered light power spectrum analysis, and hot Brownian motion theory, we attempt to measure realistic temperatures at the surface of an optically-trapped particle while properly accounting for inhomogeneous temperature fields generated by the optical trap. In Chapter 5, this technique is then applied to measure the temperature of engineered gold- and silicon-implanted silicon nanowires to rigorously study the effect ion implantation has on silicon nanowire photothermal efficiencies. Silicon nanowire photothermal efficiencies are shown to drastically increase by implanting with gold ions and cause superheating of water of over 200 °C at the trap site, suggesting potential application as agents for photothermal cancer therapies.

Chapter 6 describes the hydrothermal synthesis and optical trapping of engineered YLF nanoparticles doped with Yb^{3+} ions. Laser tweezer experiments using the developed temperature extraction techniques and hot Brownian motion analysis show the first observation of particles undergoing recently hypothesized cold Brownian motion and local laser refrigeration in a condensed phase via anti-Stokes photoluminescence. Furthermore, YLF nanoparticles codoped with Er^{3+} and Yb^{3+} ions are also developed and their intense visible upconversion of the NIR trapping laser is used to monitor its internal lattice temperature using ratiometric thermography. The results suggest the potential of these materials to investigate kinetics and temperature sensitivity of basic cellular processes, or to act as simultaneous theranostic-hypothermia agents to identify and treat cancerous tissues.

Finally, Chapter 7 presents a summary of the salient conclusions of the reported studies. The chapter concludes with a short discussion of my personal experience with being a member of a new research group and setting up the Pauzauskie laboratory.

TABLE OF CONTENTS

Page

ACRONYMS

AFM: atomic force microscope

(LA-)APT: (laser-assisted) atom-probe tomography

BF: bright field

CBM: cold Brownian motion

DDA: discrete dipole approximation

DI: deionized

EDX: energy-dispersive x-ray spectroscopy

EMT: effective medium theory

FDTD: finite-difference time domain

FTIR: Fourier transform infrared

FWHM: full width at half maximum

HAADF: high-angle annular dark field

HBM: hot Brownian motion

HIM: helium ion microscope

LEAP: local electrode atom probe

MACE: metal-assisted chemical etching

MDR: morphology-dependent resonance

MEEP: MIT electromagnetic equation propagation

NA: numerical aperture

NIR: near infrared

NW: nanowire

PL: photoluminescence

PSD: power spectral density

PT: photothermal

QPD: quadrant photodiode

SAED: select-area electron diffraction

SEM: scanning electron microscope

SINW: silicon nanowire

SRIM: stopping range of ions in matter

TE/TM: transverse electric / transverse magnetic

(HR-S)TEM: (high resolution-scanning) transmission electron microscope

TERS: tip-enhanced Raman spectroscopy

UHV: ultra-high vacuum

VAT: volume averaging theory

YAG: yttrium aluminum garnet

YLF: yttrium lithium fluoride

LIST OF FIGURES

Figure Number Page

LIST OF TABLES

ACKNOWLEDGMENTS

First, I would like to thank my advisor, Professor Peter J. Pauzauskie, for entrusting me with his vision for the lab and fostering me along this scientific journey over the last five years. A large fraction of what I have come to understand about science and engineering is a direct consequence of his guidance, encouragement, and persistence to challenge and expand my intellectual limits. His insights, dedication, and curiosity have acted as a constant source of inspiration during my graduate studies and will continue to act as a standard moving forward.

Likewise, I would also like to thank Professor Emeritus E. James Davis, who has been an incredible coadvisor and collaborator with the Pauzauskie lab. Jim's intellectual wherewithal and capacity to construct theoretical frameworks for incredibly complex problems has been a privilege to behold and has contributed immeasurably to the results and understanding of the research presented in this thesis. Yet, what I appreciate most about Jim is his seemingly infinite amount of wisdom, joy, and stories that I have been fortunate enough to experience during our weekly theory meetings throughout the last five years.

The results presented in this thesis could not have been possible without the momentous efforts of many fiends and colleagues with whom I have had the pleasure of working. I have been continuously surprised and humbled by the intelligence, ingenuity, and inventiveness of the fellow graduate students in the Pauzauskie lab, which in the end has inspired me during my research and has helped shape me into a better scientist and engineer. Therefore, I would like to thank Frances Hocutt, Zach Rousslang, Bennett Smith, Xuezhe Zhou, Shamus O'Keefe, Jennifer Hanson, Sandeep Manandhar, Mark Brunson, Matthew Lim, Matthew Crane, and Automm Lombardo for all of their help, discussion, and advice. I would also like to thank all of the undergraduate and masters students that I have had the privilege of mentoring throughout the years for all of their help and contributions to the lab.

If I have learned one thing during my graduate career it is that there is no such thing as absolute knowledge. Answers to questions simply lead to more informed and interesting questions. Yet, there is one thing that I contend I do know absolutely: that I have the most amazing set of friends and family in the world. Unfortunately, there is no way I could ever adequately convey my appreciation and gratitude that I have for them and all that they have done for me. Therefore, I simply would like to thank all of my friends and family, especially my grandparents (Charles and Eloise (Loy) Roder, Bernard (Saint) and Gayle Freeburg, Robert and Bernice Syndergaard), parents (Shane Roder Sr., Christy Freeburg Syndergaard, Phil Syndergaard), and siblings (Skyler Roder, Shane Roder Jr., Shawn Syndergaard, Alison Syndergaard Huckaby), for all of their love and support throughout the years. I would particularly like to thank my mother, who put in an endless amount of love and effort to ensure I had access to all of the opportunities needed to get to where I am today.

Lastly, I want to thank my fiancée, Sydney Stoker, for all of her love, support, and encouragement over the last seven years. Despite all of my best efforts to seek out the mysteries and unravel the wonders of this marvelous universe we all find ourselves in, I am yet to find anything as intrinsically beautiful as Sydney. She personally inspires me to be better everyday and I relish the thought of continuing this lifelong journey with her by my side.

DEDICATION

To Mom, for everything.

Chapter 1

INTRODUCTION

1.1 Motivation

Over the last 5 years in the Pauzauskie lab, my research has focused on devising new approaches and techniques to use laser tweezers to study novel, engineered materials at the micro- and nanoscale. Laser tweezers (a.k.a. laser traps, optical traps) are one of a very few tools that allow for careful and precise manipulation, characterization, and sensing of individual particles isolated from surfaces and interfaces in various types of environments, be it in vacuum, gas, solvent, or even biological media and cells. To this day, scientists and engineers are constantly finding new ways to implement laser tweezers to elucidate the mysteries in the fields of biology, medicine, microelectronics, refrigeration, climate change, and many others. While laser tweezers have proven to be very unique and powerful tools, there continues to exist areas where experiments using laser tweezers can be improved.

As an apposite example, laser tweezers are well suited for studying the binding strength and kinetics of cellular organisms as the forces that these materials can administer are in the same regime that laser tweezers can sense and transduce (10^{-9}-10^{-12} newtons). Typically, these experiments are performed by chemically tethering an optically-trapped microbead to the cellular organism of interest and observing how the organism pushes and pulls on the tethered microbead. The organism's motion affects the motion and position of the optically-trapped microbead, which can be ascertained by monitoring the forward-scattered laser light using a position-sensitive photodetector. How these measurements can be made and used to measure forces is detailed later in this chapter in Sec. 1.2.

Yet, a prevalent assumption that is made during these measurements is that the optically-trapped microbead does not photothermally heat. This assumption allows for the contribution of the thermal energy to the kinetics of the system to be ignored, thereby simplifying the analysis of the forward-scattered laser signal when determining the applied forces of the organism on the optically-trapped microbead. Scientists who perform these experiments carefully choose the material of the microbead as well as the laser wavelength in order to minimize absorption of the laser by the microbead, consequently minimizing the photothermal heating of the microbead. Still, irradiances at the trapping site are very large (on the order of MW/cm^2), causing even inefficiently absorbing particles to moderately heat photothermally during a laser trapping experiment. Possessing the ability to determine the thermal contribution of an optically-trapped particle to the system would allow for a more accurate description of the true forces and dynamics present during an experiment.

Furthermore, it is worth noting that the utility of determining temperatures of optically-trapped particles in a laser tweezer is not limited to informing those in the optical trapping community; there are many fields of study that are interested in photothermally heating and refrigerating micro- and nanoscale materials for various applications. Some example applications include photothermal cancer agents, vibration-free cryogens, and selective particle sorting. Moreover, many material properties are temperature dependent: knowing the temperature of isolated optically-trapped particles enables careful and accurate characterization at a single particle level rather than through bulk or ensemble measurements.

In short, having access to the temperature of optically-trapped particles helps inform ongoing experiments in the trapping community as well as opens up many new and exciting possibilities for future research directions and applications. In the remainder of this thesis, I will outline my efforts in explicating and implementing methods and techniques for accurately determining temperatures of optically-trapped particles.

1.2 Fundamentals of optical trapping

The experiments, analysis, and results of this thesis hinge critically on understanding how temperature, particle morphology, and thermal/optical properties of both the particle and the solvent affect the dynamics of a particle in an optical trap. In this section, we will set the stage by reviewing the history of observing optical forces and how optical trapping came about. Then, we will and review the fundamentals of optical forces and derive the dynamics of a particle in an optical trap.

1.2.1 Historical context

When deriving the energy and stress of electromagnetic radiation in his 1873 treatise on electricity and magnetism [1], James Clerk Maxwell stated *"... in a medium in which waves are propagated there is a pressure in the direction normal to the waves, and numerically equal to the energy in unit of volume"* He went on to predicted that this pressure could be experimentally observed using a balance, a flat body, and sunlight. This idea that light could exert pressure on objects was at the time exciting and controversial. Yet, scientists still used this new concept to explain phenomena that previously had unknown origins. For instance, in 1892 Pyotr Nikolaevich Lebedev (transliterated as Peter Lebedew) applied the concept of radiation pressure to discern the solar repulsion of comet tails [2]. Later in 1900, Svante Arrhenius likewise used radiation pressure to explain the aurora borealis [3]. However, it wasn't until 1901 that radiation pressure was first observed experimentally by Ernest Nichols and Gordon Hull [4] by cleverly using a torsional balance and thermal light sources, shown in Fig. 1.1. Despite this prodigious result, experts during that time remained skeptical of radiation pressure due to the fact that the interaction was so minute. In fact, John Henry Poynting stated at his presidential address of the British Physical Society in 1905 that[5] *"A very short experience in attempting to measure these forces is sufficient to make one realize their extreme minuteness – a minuteness which appears to put them beyond consideration in terrestrial affairs."*

Almost 40 years went by until a 22 year old Columbia University undergraduate student, Arthur Ashkin, became interested in radiation pressure. At that time in 1944, he was working for Sid Millman at the Columbia Radiation Laboratory designing a high-powered megawatt 3cm X-band pulsed "Rising Sun" magnetron for the US Army during World War II [6]. At such high powers, Ashkin pondered whether he could detect the pulses from the magnetron by

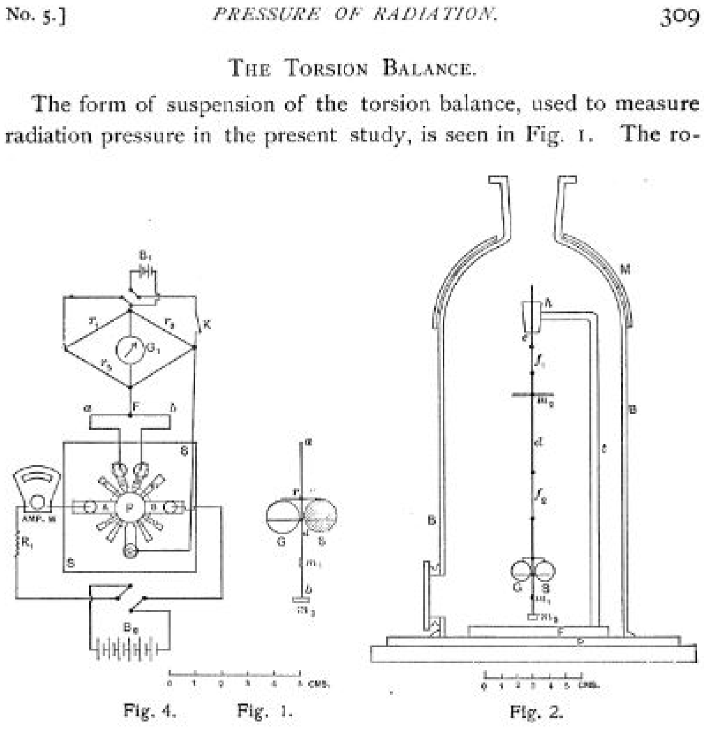

No. 5.] PRESSURE OF RADIATION. 309

THE TORSION BALANCE.

The form of suspension of the torsion balance, used to measure radiation pressure in the present study, is seen in Fig. 1. The ro-

Fig. 4. Fig. 1. Fig. 2.

Figure 1.1: A diagram of the famous torsional balance that was used by Ernest Nichols and Gordon Hull to detect the radiation pressure of light. Reproduced with permission from [4].

observing deflections of [6] *"an old electromagnetic telephone earpiece consisting of a metallic vibration receiver plate and some magnetic pickup coils."* When the signal was observed on his oscilloscope, Ashkin interpreted the result as radiation pressure on the metallic receiver. Even though he was excited by the result, Ashkin decided not to pursue the experiment any further[6].

In the late 1960s, Ashkin (now working at Bell Labs) again had his interest in radiation pressure piqued. At a conference, he witnessed a talk about unascertained "runners and bouncers:" small particles that exhibited erratic motion in a laser cavity. Speakers at the conference suggested these particles could be moving due to radiation pressure of the stimulated radiation inside of the cavity. By performing a quick back-of-the-envelope calculation,

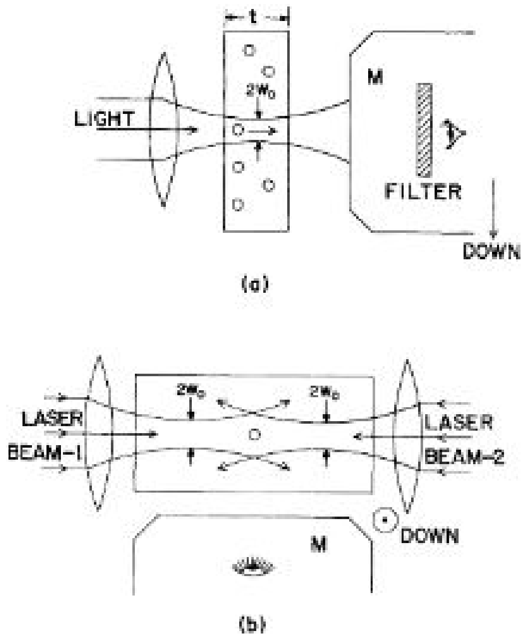

FIG. 1. (a) Geometry of glass cell, $t = 120\ \mu\text{m}$, for observing micron particle motions in a focused laser beam with a microscope M. (b) The trapping of a high-index particle in a stable optical well. Note position of the TEM$_{00}$-mode beam waists.

Figure 1.2: Arthur Ashkin's first publication on the effect of radiation pressure on micro-sized particles in solution. Reproduced with permission from [7].

Ashkin found that the forces required to move the particles were insufficient to cause the erratic motion of the runners and bouncers. Yet, Ashkin reasoned that a focused laser may provide sufficient radiation pressure to small microparticles in water to cause directed movement. In fact, Ashkin was the first to observe that small polystyrene microbeads (2.5μm diameter) could be pushed along in the propagation direction of the incident laser [6]. Moreover, he was surprised to observe that the microbeads were attracted towards the center of the focused laser[6]. This simple experiment ultimately gave rise to two different, yet similar, research fields: laser cooling of atoms, and laser trapping of small particles. The former field of laser cooling of atoms was picked up and championed by Ashkin's partner Steven Chu, who went on to win the Nobel Prize in Physics in 1997. Ashkin focused on the latter field of laser trapping of small particles and went on to develop the laser tweezer.

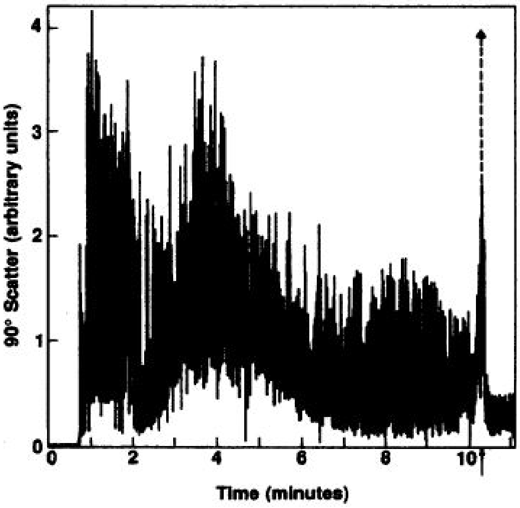

Figure 1.3: Figure in Arthur Ashkin's publication on optically-trapped tobacco mosaic viruses and E. coli. The arrow represents where the trapping laser power was increased and the decrease in scattered signal indicates the loss of cellular content of the trapped bacterium. Reproduced with permission from [8].

The single-beam laser tweezer (as opposed to the dual beam or levitation laser traps) was originally designed for atom trapping experiments. In order to test the single-beam laser tweezer, Ashkin trapped sub-micron colloidal silica particles[9] with a 514nm argon laser. After the successful experiment, Ashkin attempted trapping rod-like tobacco mosaic viruses[8] (TMV) and made an interesting observation: the seemingly self-propelled bacteria in solution would become immobilized in the trap and then seemingly die, shown in Fig. 1.3. Ashkin determined that the death of the trapped bacterium was a result of "optocution" due to high cellular absorption of light at 514nm. Ashkin [10, 11] found that optocution could be mitigated by employing laser sources with near-infrared (NIR) wavelengths which lay in the cellular transparency window. By trapping with NIR wavelengths, Ashkin found it was possible to non-invasively study and manipulate living organisms.

To this day, laser tweezers are still primarily used for biological experiments to study fundamental cellular processes like mitosis and biological motors [12, 13]. However, the last couple of decades have shown that laser tweezers have utility in various other applications and fields, such as 3D nanoparticle manipulation and fabrication [14], single particle Raman and photoluminescence spectroscopy[15, 16], and photonic force microscopy [17].

1.2.2 Trapping forces from a focused laser

As experimentally verified by Nichols and Hull[4], light exerts a force via transfer of momentum during scattering events. Understanding how light can exert these forces on a material in both a quantitative and qualitative sense can give insight into how an optical trap works at a fundamental level. In the most general sense, the time-averaged force from the scattering of an electromagnetic field off of an object is equal and opposite to the momentum carried by the electromagnetic field itself[18]. Therefore, one simply needs to enclose the particle in some volume and integrate the light momentum flux over the volume's surface **S**. The flux in the light momentum is related to the scattered fields, and the relationship between the electromagnetic forces and mechanical momentum is given by the Maxwell stress tensor $\mathbf{T_M}$[18]. The total time-averaged optical force $\langle \mathbf{F_{tot}} \rangle$ on a particle then becomes

$$\langle \mathbf{F_{tot}} \rangle = \int_S \langle \mathbf{T_M} \rangle \cdot d\mathbf{S}. \tag{1.1}$$

Determining the scattered fields analytically from Maxwell's equations can be a pestiferous task, often requiring simulation methods such as discrete dipole approximation (DDA)[19] or complex algorithms such as the T-matrix method[20] to solve for them.

Obtaining an analytical solution for the total time-averaged optical force can be drastically simplified, and therefore more easily understood, if we limit ourselves to spherical particles in certain size regimes: where the radius of the sphere (a) is much larger than the wavelength of light (λ), and where the radius of the sphere is much smaller than the wavelength of light.

In the regime where $a \gg \lambda$, the conditions for Mie scattering are satisfied and optical forces on the particle can be found using simple ray optics. Assuming that the sphere has a refractive index greater than the surrounding medium, the transfer of light's momentum to the sphere can then be shown by (1) absorption and back-scattering of light, thereby imparting a force in the incident direction of the light, and (2) light refracting through the sphere, thereby imparting a force in the opposite direction of the refracted beam (Fig. 1.4). Traditionally, the total force ($\mathbf{F_{tot}}$) is separated into two components, $\mathbf{F_{scatt}}$ and $\mathbf{F_{grad}}$, corresponding to the absorption/back-scattering and refraction of the incident light, respectively.

The scattering force $\mathbf{F_{scatt}}$ (often referred to as the radiation pressure) is normally the dominant force component and is in the direction of the propagating beam, as shown in Fig. 1.4b. The gradient force $\mathbf{F_{grad}}$ is normally zero in a light field of uniform intensity as an equal number of photons refract in opposite directions, subsequently canceling their force contributions. However, in an inhomogeneous light field where there exists an intensity gradient (Fig. 1.4a), more photons in the intense region will refract than in the less intense region, resulting in a net force in the direction of the intensity gradient (Fig. 1.4c). Consequently, the sphere will be attracted to the maximum of the intensity gradient where there is no net force from the gradient component (Fig. 1.4d) and any perturbation from the equilibrium will result in a restoring force towards the gradient maximum.

The optical forces $\mathbf{F_{scatt}}$ and $\mathbf{F_{grad}}$ can likewise be defined in the regime where $a \ll \lambda$. In this regime, the conditions for Rayleigh scattering are satisfied and the sphere can be treated as a point dipole or a collection of point dipoles. In this case, the total time-averaged optical force is known[21] and is given by

$$\langle \mathbf{F_{tot}} \rangle = \frac{1}{2} \operatorname{Re} \left(\sum_{j=x,y,z} \alpha E_j \nabla E_j^* \right), \tag{1.2}$$

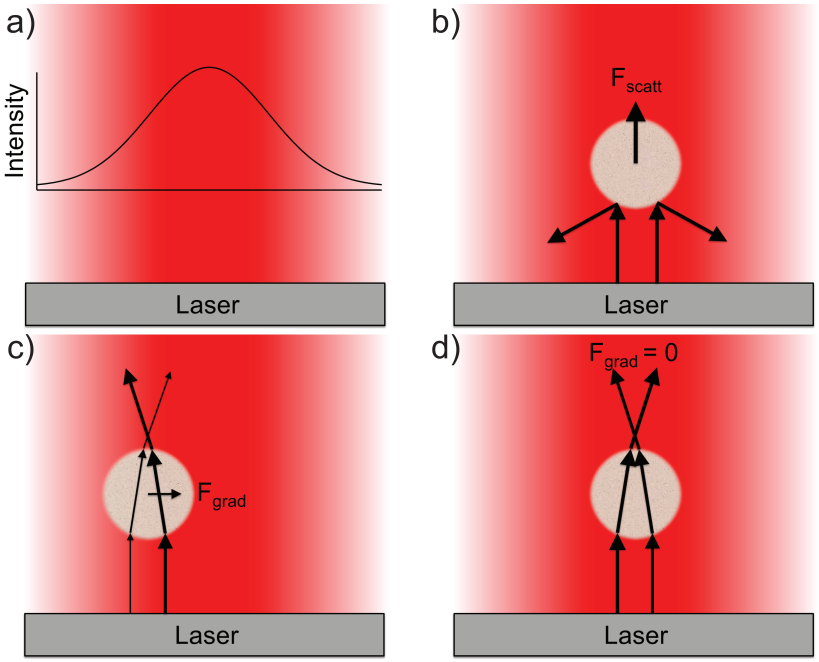

Figure 1.4: Illustration of optical forces on a spherical particle in the ray optics (Mie, $a \gg \lambda$) regime. a) Gaussian distribution of light intensity from an unfocused laser. b) Radiation pressure ($\mathbf{F_{scatt}}$) in the direction of light propagation from back-scattered and absorbed light. The gradient force ($\mathbf{F_{grad}}$) points towards the intensity gradient when positioned off the gradient maximum (c) and is zero when positioned on the gradient maximum (d).

where E_j is the electric field components of the light and

$$\alpha = \frac{\alpha_0}{1 - \frac{ik^3\alpha_0}{6\pi\varepsilon_0}}. \tag{1.3}$$

In Eq. 1.3, α is the sphere's electric polarizability, k is the light's wavevector, ε_0 is vacuum permittivity, and α_0 is the point-like particle polarizability given by the Clausius–Mossotti relation[22, 23]

$$\alpha_0 = 4\pi\varepsilon_0 a^3 \left(\frac{\varepsilon - 1}{\varepsilon + 2}\right), \tag{1.4}$$

where ε is the relative permittivity. Furthermore, Eq. 1.2 can be expanded and expressed as [23]

$$\langle \mathbf{F_{tot}} \rangle = \underbrace{\frac{1}{4}\,\mathrm{Re}\,(\alpha)\,\nabla\,|\mathbf{E}|^2}_{F_{grad}} + \underbrace{\frac{\sigma}{2c}\,\mathrm{Re}\,(\mathbf{E}\times\mathbf{H}^*)}_{F_{scatt}}, \tag{1.5}$$

where σ is the extinction cross-section, c is the speed of light in vacuum, $\mathbf{E}$ is the electric field, and $\mathbf{H}$ is the magnetic field. As a reminder, the electric field amplitude associated with light is related to the intensity I by

$$I = \frac{1}{2}\,\mathrm{Re}\,(\mathbf{E}\times\mathbf{H}^*) = \frac{c\varepsilon_0 n}{2}\,|\mathbf{E}|^2\,, \tag{1.6}$$

where n is the complex refractive index of the medium in which the light is propagating. By considering Eqs. 1.5 and 1.6, we see that the radiation pressure $\mathbf{F_{scatt}}$ is determined by absorption and reradiation (σ) of the light by the sphere and scales linearly with the intensity ($\mathrm{Re}\,(\mathbf{E}\times\mathbf{H}^*)$) of the laser. Moreover, the gradient force $\mathbf{F_{grad}}$ is generated by the fact that an light-induced dipole, governed by $\mathrm{Re}\,(\alpha)$, interacts with an inhomogeneous electric field gradient ($\nabla\,|\mathbf{E}|^2$).

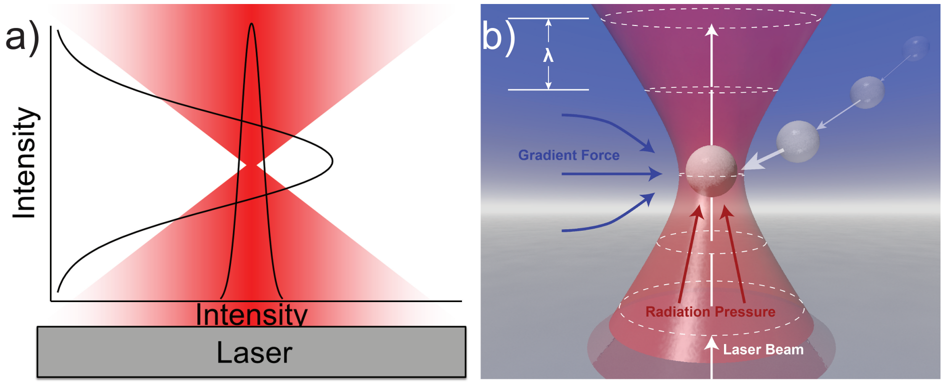

Figure 1.5: Illustration of the optical trapping forces on a spherical particle. a) For trapping, a large intensity gradient must be established in both the transverse and longitudinal directions. b) Near the laser focus, there exists sufficient field gradients and the restoring gradient force overcomes the repulsive scattering force forming a stable optical trap.

Independent of the size regime we describe the optical forces in, it remains that in order to achieve optical trapping of a particle, two conditions must be met: (1) there must exist a light intensity gradient in all spatial dimensions (transverse as well as parallel to the direction of beam propagation, Fig. 1.5a), and (2) the subsequent gradient force $\mathbf{F_{grad}}$ must be sufficiently large to overcome the radiation pressure $\mathbf{F_{scatt}}$. To obtain large electric field gradients, typically an overfilled, high numerical aperature (NA) objective is used to focus a TEM_{00} laser to obtain a diffraction-limited focus. The high NA objective ensures a large gradient in the longitudinal direction and the diffraction-limited focus maximizes the gradient in the focal plane.

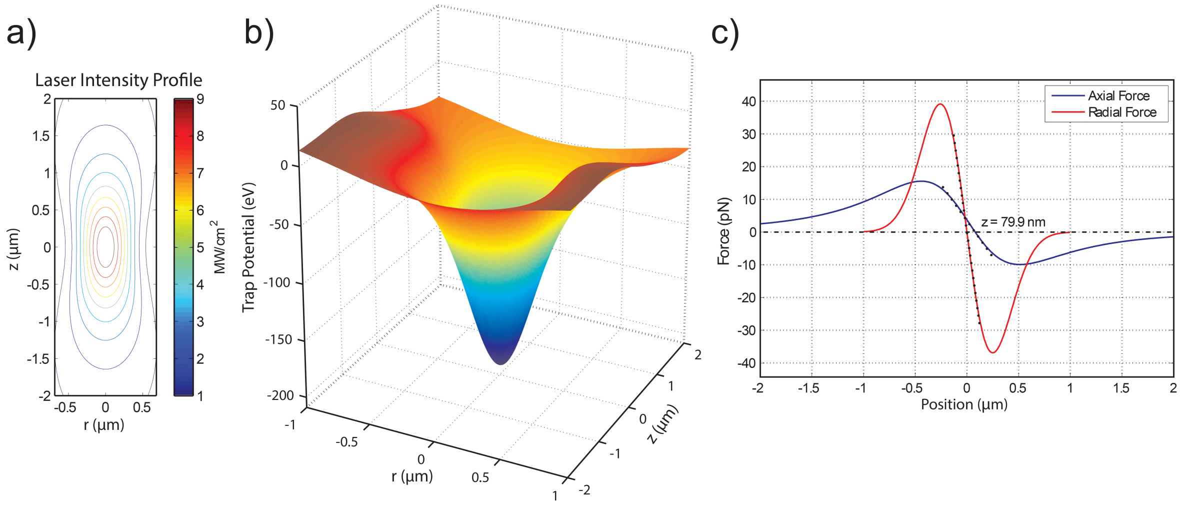

Figure 1.6: Results of the simulated potential well (b) and trapping forces (c) on a 1 μm diameter silica sphere in water for a 975nm wavelength laser (a) focused to a 1 μm spot with an irradiance of 10 MW/cm^2. The resulting trapping potential well in (b) has a depth of -200 eV, resulting in a trapping stiffness (c) of k_r = 229.3 pN/μm and k_z = 43.7 pN/μm with a maximum trapping force of 40 pN in the transverse direction and 15 pN in the axial direction. The equilibrium position for the silica sphere is at r = 0 nm, z = 79.9 nm.

Using Eqs. 1.2-1.6, it becomes possible to predict the optical trapping forces that exist when trapping a spherical particle in the Rayleigh regime. Assuming a 10 MW/cm^2 trapping laser irradiance with a focal spot diameter of 1μm and a wavelength of $\lambda = 975$nm for a 1μm diameter silica sphere in water, Fig. 1.6 shows the results of a simulation of the resulting optical trap potential well (Fig. 1.6b) as well as the axial (z) and radial (r) restoring forces (Fig. 1.6c). It is evident that the intensity gradient for a focused TEM$_{00}$ is larger in the transverse direction (r) than in the direction of axial beam propagation (z). The restoring force of the silica bead back to its equilibrium position is therefore greater in the transverse direction than in the axial direction, as shown in Fig. 1.6c. Since the restoring force is linear for displacements roughly less than 150nm from the equilibrium position (due to the fact that the trap potential well is harmonic for these displacements, as shown in Fig. 1.6c), the force is often modeled as a spring force

$$F_{trap}(r) = -k_r r \tag{1.7}$$

and

$$F_{trap}(z) = -k_z z, \tag{1.8}$$

where k_r and k_z are termed the trap stiffness for transverse and axial displacements, respectively. For the silica sphere simulation, the trap stiffnesses are $k_r = 229.3$ pN/μm and $k_z = 43.7$ pN/μm with a maximum trapping force of 40 pN in the transverse direction and 15 pN in the axial direction. Moreover, as shown in Fig. 1.6c, the equilibrium position of the silica sphere is at r = 0 nm in the transverse direction, but is slightly offset at z = 79.9 nm in the axial direction. The offset stems from the radiation pressure pushing the sphere away from the maximum electric field gradient in the axial direction.

1.2.3 Dynamics of an optically trapped particle

When small particles are dispersed in an incompressible fluid, they undergo random (stochastic) displacements (Brownian motion) due to thermal fluctuations in the fluid which can be accurately described by fluctuating hydrodynamics[24]. The thermal fluctuations contribute equally to the motion of the particles for each degree of freedom. For high-symmetry particles like spheres, the degrees of freedom are the center-of-mass translational motion in the orthogonal basis directions (x,y,z). For particles with lower symmetry like cylinders, angular fluctuations are also taken into account. However, for an optically trapped particle, the particle is constrained to the harmonic potential well (Fig. 1.6b). We can describe the time evolution of a subset of the degrees of freedom of this constrained stochastic system via the Langevin equation. For translational displacements in the x-direction, the Langevin equation is given by

$$m\ddot{x}(t) = F_{g,x}(t) + F_{drag,x}(t) + F_{trap,x}(t) + F_{Brown,x}(t), \tag{1.9}$$

where m is the particle mass, F_g is the gravitational force, F_{drag} is the Stokes' drag, F_{trap} is the trapping force, and F_{Brown} stochastic thermal force.

From Einstein's seminal derivations on Brownian motion[25], we have the equation of the stochastic velocity $\dot{x}_s$ of a particle in a thermal field

$$\dot{x}_s(t) = \sqrt{2D}\varsigma(t), \tag{1.10}$$

where

$$D = \frac{k_B T}{\gamma(T)}. \tag{1.11}$$

In Eq. 1.11, D is the diffusion coefficient, $\gamma(T)$ is the temperature-dependent Stokes' drag coefficient, and $\varsigma(t)$ is a random white noise process. It is informative to recognize that $\gamma(T)$ is the product of a morphology-dependent term g and the temperature-dependent viscosity of the solvent $\eta(T)$

$$\gamma(T) = g\eta(T). \tag{1.12}$$

As an example, a sphere with radius a has morphology-dependent g coefficient of $g = 6\pi a$. Using Eqs. 1.10 and 1.11, we can solve for the stochastic thermal force

$$F_{Brown}(t) = \gamma(T)\dot{x}_s = \gamma(T)\sqrt{2D}\varsigma(t). \tag{1.13}$$

Furthermore, the Stokes' drag for a particle in a fluid is given by

$$F_{drag}(t) = \gamma(T)\dot{x}(t). \tag{1.14}$$

As shown in the previous section, for small displacements from the optical trap equilibrium position, the trapping force is of the form $F_{trap}(t) = -k_x x(t)$. Dropping the (t) for simplicity, the Langevin equation (Eq. 1.9) becomes

$$m\ddot{x} = mg - \gamma(T)\dot{x} - k_x x + \gamma(T)\sqrt{2D}\varsigma. \tag{1.15}$$

For a particle in Brownian motion, the characteristic time t_c for loss of kinetic energy through drag is given by[24]

$$t_c = \frac{m}{\gamma(T)}. \tag{1.16}$$

In Eq. 1.16, t_c is typically 2-3 orders of magnitude shorter than experimental sampling times, assuming 10-100 kHz sampling rates. Consequently, the inertial terms in Eq. 1.9 can be neglected[24]. By dropping the inertial terms in Eq. 1.9, we obtain

$$0 = -\gamma(T)\dot{x} - k_x x + \gamma(T)\sqrt{2D}\varsigma, \tag{1.17}$$

and therefore

$$\gamma(T)\sqrt{2D}\varsigma = \gamma(T)\dot{x} + k_x x. \tag{1.18}$$

Dividing both sides of Eq. 1.18 by Stokes' drag coefficient $\gamma(T)$, we get

$$\sqrt{2D}\varsigma = \dot{x} + \frac{k_x}{\gamma(T)}x. \tag{1.19}$$

Defining the relaxation frequency as $f_r \equiv k_x/\gamma(T)$ and the corner frequency as $f_c \equiv f_r/2\pi$, Eq. 1.19 becomes

$$\sqrt{2D}\varsigma = \dot{x} + 2\pi f_c x. \tag{1.20}$$

Equation 1.20 is the characteristic equation for the dynamics of an optically trapped particle. This treatment is often referred to as the Einstein−Ornstein−Uhlenbeck theory of Brownian motion. However, Eq. 1.20 can be cumbersome to fit to experimental data.

Therefore, the dynamics of an optically trapped particle is often determined by analyzing its characteristic power spectrum. For discrete time measurements t_m, the Fourier transform of Eq. 1.20 is

$$\tilde{x}_n = \frac{\sqrt{2D}\tilde{\varsigma}_n}{f_r - i2\pi f_n}, \tag{1.21}$$

where n is an integer, $f_n \equiv n/t_m$ is the discrete sample frequency, $\tilde{x}_n$ is the Fourier transform of x, and $\tilde{\varsigma}_n$ is the Fourier transform of ς. The discrete power spectrum S_n is then given by

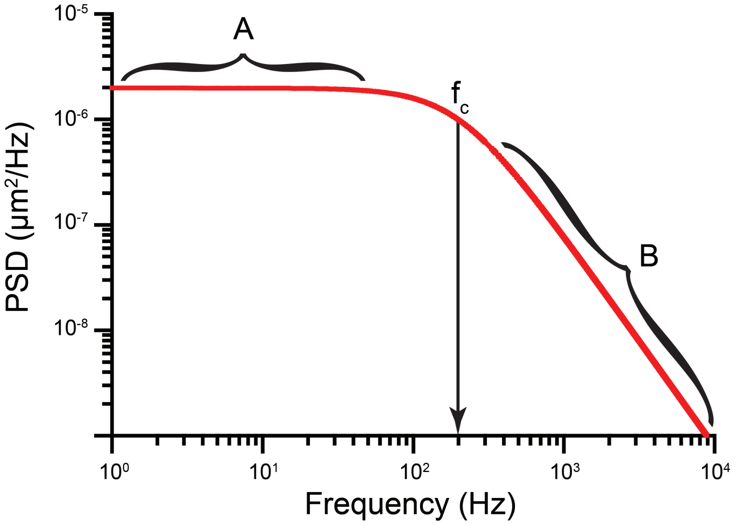

Figure 1.7: Plot of an example power spectrum S(f) showing its Lorentzian form. In the low frequency regime (f≪f$_c$, region A), the power spectrum is approximately constant. In the high frequency regime (f≫f$_c$, region B), the power spectrum falls off with a $\frac{1}{f^2}$ dependence. Plotted on a log-log scale, the high-frequency region shows a characteristic constant decrease with slope = -2.

$$S_n = \frac{\mid \tilde{x}_n \mid^2}{t_m} = \frac{D}{2\pi^2 t_m} \frac{\mid \tilde{\varsigma}_n \mid^2}{(f_c^2 + f_n^2)}. \tag{1.22}$$

If we take the expectation value of Eq. 1.22 and take advantage of the fact that $\langle \mid \tilde{\varsigma}_n \mid^2 \rangle =$

$\sqrt{2}t_m$, we obtain the power spectrum

$$S(f_n) = \frac{(\frac{\sqrt{2}D}{2\pi^2})}{(f_c^2 + f_n^2)}, \tag{1.23}$$

which takes the form of a Lorentzian function. For $n > 0$ and dropping the n subscript, we obtain the characteristic power spectrum of the particle in an optical trap, given by

$$S(f) = \frac{D}{2\pi^2(f_c^2 + f^2)}. \tag{1.24}$$

The characteristic power spectrum given in Eq. 1.24 and shown in Fig. 1.7 has units of [m^2/Hz] and contains information of the thermal energy of the system (D,$\gamma(T)$), the stiffness of the optical trap (f_c), and the morphology of the trapped particle ($\gamma(T)$). In the next chapter, we will review how to experimentally obtain and analyze the power spectrum of a trapped particle in a laser tweezer setup to determine parameters of interest.

Chapter 2

EXPERIMENTAL DETECTION OF TRAPPED PARTICLE DYNAMICS

2.1 Introduction

Now that we have a grasp of the dynamics of a particle in an optical trap, the challenge becomes experimentally obtaining those dynamics. In this chapter, we will detail the key components of a laser tweezer system. We will then delve into obtaining trapped particle dynamics by detecting forward-scattered laser light in the back focal plane of the laser tweezer. Since the detection device generates a voltage signal, we will then cover how to calibrate the generated voltage signals to obtain time-dependent particle displacement signals. Lastly, we will apply our understanding of the dynamics of the system to develop multiple methods for ascertaining the temperature of optically trapped particles.

2.2 Laser tweezer configuration

As mentioned previously, a crude laser trap can be obtained by simply focusing a laser with a high NA objective. However, for most trapping experiments, it is important to have the capability to incorporate multiple lasers, move the sample with high precision, control the temperature of the trapping environment, image the trapped particle, collect trapped particle photoluminescence, and collect forward-scattered light with a laser-sensitive position detector. As an example of a typical laser tweezer system, a schematic of the Pauzauskie lab laser tweezer is provided in Fig. 2.1.

First, the laser sources must be coupled into the beam train. Care must be taken to ensure that the optics in the system are rated for the wavelengths of the lasers that are being coupled into the system in order to avoid unwanted absorption, heating, and reflections. Furthermore,

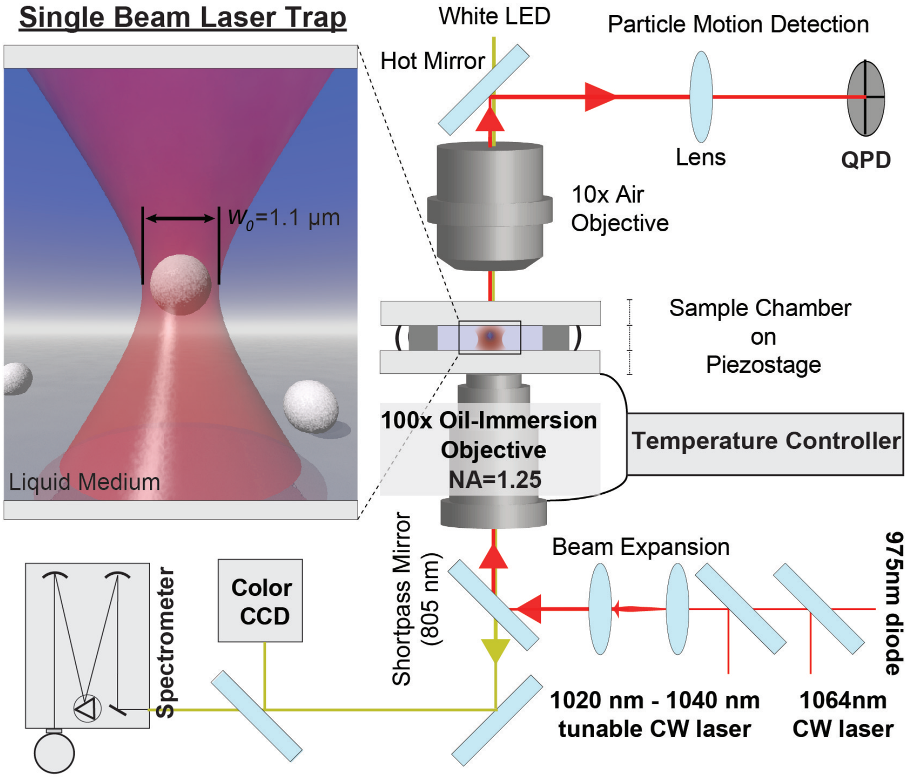

Figure 2.1: Schematic of the Pauzauskie lab laser tweezer.

laser sources are typically TEM$_{00}$ mode in order to obtain a diffraction-limited focus with the maximum of the electric field gradient at the focal spot. Once the beams are co-aligned, they are then sent into the beam expanding region where the lasers pass through a Galilean telescope to increase the spot size to a diameter such that the $1/e^2$ intesity points of the gaussian intensity distribution match the focusing objective aperture[26]. The light on the periphery of the beam contributes primarily to the axial gradient force, whereas the light at the center of the beam is primarily responsible for the scattering force. Therefore, by overfilling the objective lens, we can maximize the ratio F_{grad}/F_{scatt}, thereby maximizing the trapping efficiency[27].

After passing through the expansion region, the beam is then sent through a high NA focusing objective lens. Typically, water- and oil-immersion objectives are used to further increase the focusing angle and thereby increasing the axial trap stiffness. Transparent sample chambers containing micro- and nanoparticles suspended in a solvent are then put in contact with the oil-immersion objective so that the particles are in proximity to the focal plane. Since the working distance of the objective is very small ($\sim$200μm), the sample chamber surface that is in contact with the objective needs to be very thin. Sample chambers are thus often prepared by dispersing several microliters of the particle/solvent dispersion by a pipette into a chamber consisting of a glass slide and a thin glass coverslip. The edges of the glass slide and the glass coverslip are then sealed with a 150μm$-$thick adhesive spacer. Alternatively, a temperature-controlled perfusion chamber can be used in lieu of a glass slide chamber if solvent exchange or temperature control during trapping experiments is desired. The chamber is placed on a piezostage to enable manipulation of trapped particles in all dimensions with a resolution of $\sim$5nm in closed feedback mode.

Once passed through the sample chamber, the diverging beam is then collected by a condenser lens. When a particle is held in the laser trap, the forward-scattered light that is collected by the condenser lens carries information on the displacement of the particle in the laser trap. For small particles in the Rayleigh regime, this can be understood as the spherical scattered waves from the dipole/particle interfering with the unscattered laser that produces constructive or destructive interference in the back focal plane that depends on the position of the dipole/particle with respect to the trap position. For large particles in the Mie regime, there is no interference effects. Yet, the beam is still modulated by the position of the particle in the trap due to refraction and scattering. Therefore, the displacement of the particle in the laser trap can be ascertained using a position-sensitive photodetector in the back focal plane. Details on obtaining and analyzing signals from the photodector are discussed in the next section.

The condenser lens can also be used to illuminate the sample during trapping experiments for real-time imaging. Dichroic (hot) and long-/shortpass mirrors can be used to selectively direct trapping lasers while allowing illumination and excitation sources to pass without damaging detectors with the high intensity laser source (see Fig. 2.1). Furthermore, long- and shortpass mirrors can be used to collect Raman and photoluminescence signals, enabling unique capabilities for optical characterization of individual particles. Lastly, it is worth noting that other components can be introduced into the tweezer setup to accomplish targeted tasks. As an example, the mirror that directs the lasers into the beam expanding region can be replaced with a galvomirror, allowing for time splitting of a single laser beam into multiple beams separated by a given distance.

2.3 Determining optically trapped particle dynamics from forward-scattered light

Once a laser tweezer has been built and the laser turned on, optically trapping and manipulating micro- and nanoparticles becomes a relatively straightforward task given that they comply with the trapping requirements outlined in Sec. 1.2.2. As mentioned above, the forward-scattered light from the trapped particle is then collected by the condenser lens and sent onto a quadrant photodiode (QPD) in the back focal plane to monitor the deflection of the trapping beam due to the motion of the optically-trapped particle as discussed in Sec. 1.2.3. The QPD is well-suited to rapidly detect small perturbations in the forward-scattered light, allowing for typical sampling frequencies of 100 kHz and corresponding particle displacement sensitivity of less than a nanometer. The absolute position of an optically-trapped particle is proportional to the photovoltage produced on each quadrant (Q1-Q4) of the QPD and is given by

$$V_x = (Q1 + Q4) - (Q2 + Q3)\,, \tag{2.1}$$

$$V_y = (Q1 + Q2) - (Q3 + Q4)\,, \tag{2.2}$$

$$V_z = V_{sum} = Q1 + Q2 + Q3 + Q4. \tag{2.3}$$

The motion of a particle in the optical trap corresponds to a shift in the forward-scattered light's intensity upon the QPD, as illustrated in Fig. 2.3. However, the effect that the trapped particle's motion has on the forward-scattered light is morphology dependent and

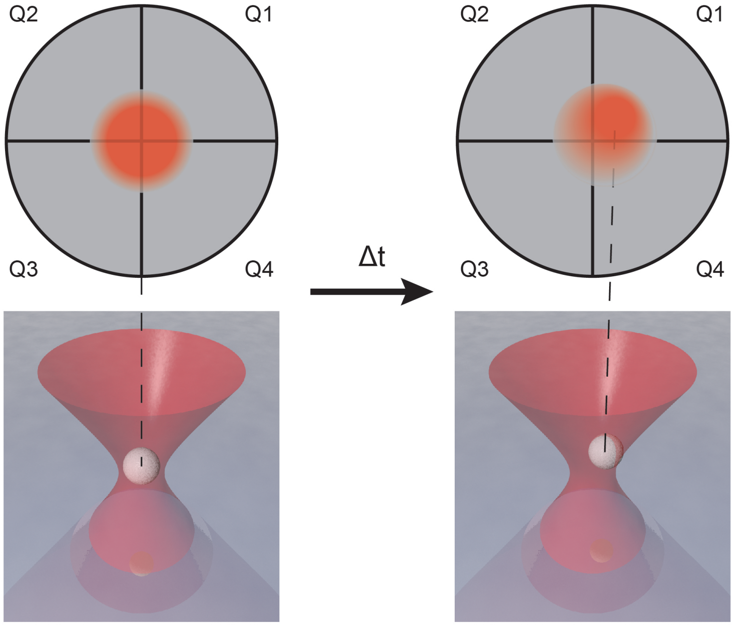

Figure 2.2: Illustration of the time-dependent shift in forward-scattered light intensity upon a quadrant photodiode (QPD) array in the back focal plane of a laser tweezer due to the motion of a spherical particle in an optical trap.

therefore the size and shape of the particle needs to be considered.

For particles with high symmetry such as spheres, the QPD photovoltage signals $V_{x,y,z}$ generated by the forward-scattered trapping laser is directly proportional to the time-dependent center-of-mass displacement $d_{x,y,z}(t)$ of the trapped particle. That is to say,

$$d_{x,y,z}(t) = \beta_{x,y,z} V_{x,y,z}(t), \tag{2.4}$$

where β is the proportionality constant (often termed the calibration coefficient) that converts voltage to displacement. Details on methods for determining β to calibrate voltage signals generated by the QPD is covered in Sec. 2.4. Therefore, if the calibration constants are known, the dynamics of trapped spherical particles can be determined by following the analysis detailed in Sec. 1.2.3.

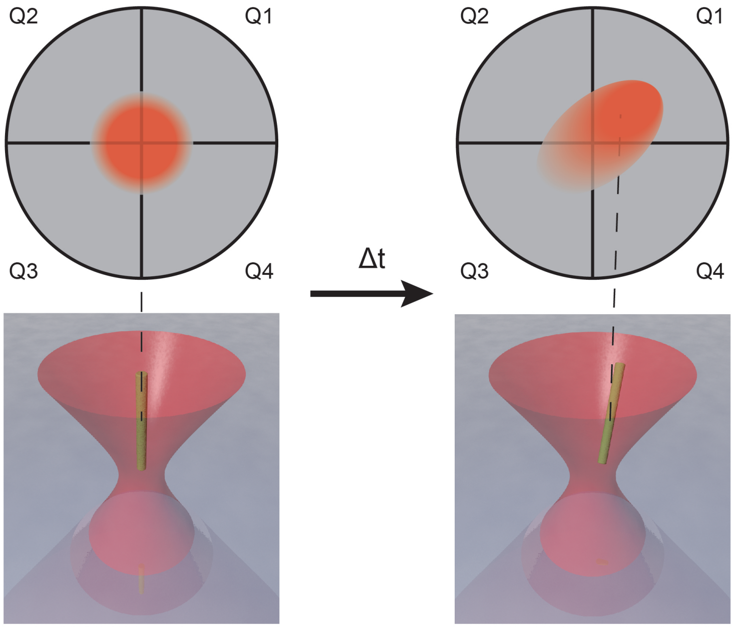

Figure 2.3: Illustration of the time-dependent shift in forward-scattered light intensity upon a quadrant photodiode (QPD) array in the back focal plane of a laser tweezer due to the motion of a cylindrical particle in an optical trap.

For particles with lower symmetry such as cylinders, the QPD photovoltage signal $V_{x,y,z}$ generated by the forward-scattered trapping laser is directly proportional to the time-dependent center-of-mass displacement $d_{x,y,z}(t)$ convoluted with the angular projections of rotational fluctuations $\Theta_{x,y}(t)$ of the trapped particle. The magnitude of the contribution of the angular fluctuations to the intensity change of the forward-scattered light scales by the length L of the cylinder. Consequently, the QPD photovoltage signals are given by

$$V_{x,y}(t) = \beta_{x,y}\left[d_{x,y}(t) + L\Theta_{x,y}(t)\right], \tag{2.5}$$

$$V_z(t) = \beta_z d_z(t). \tag{2.6}$$

Here, the angular projection $\Theta_x(t) = \theta(t)\cos(\phi(t))$ and $\Theta_y(t) = \theta(t)\sin(\phi(t))$, where $\theta(t)$ is the azimuthal angle in the xy-plane and $\phi(t)$ is the polar angle from the positive z-axis; both of which fluctuate in time. The convolution of the angular and translational motions must be considered when extracting relevant system properties. As the angular and translational motions are typically weakly interacting[28], they give rise to separate power spectra that can be found by fitting the corresponding calibrated QPD photovoltage power spectrum to a double Lorentzian. That is, Eq. 1.24 is modified to be given by

$$S(f) = \frac{D_d}{2\pi^2(f_{c,d}^2 + f^2)} + \frac{D_\Theta}{2\pi^2(f_{c,\Theta}^2 + f^2)}. \tag{2.7}$$

As illustrated in Fig. 2.4, corner frequencies that result from angular fluctuations ($f_{c,\Theta}$) are typically on the order of 10 Hz, whereas those from center-of-mass translational motion ($f_{c,d}$) are typically on the order of 100-1000 Hz.

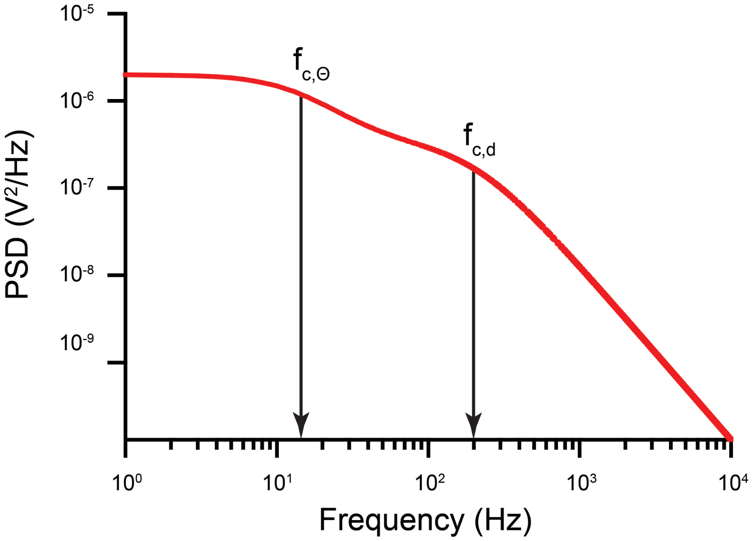

Figure 2.4: Plot of an example power spectrum S(f) with convoluted center-of-mass translational motion (d) as well as angular fluctuations (Θ), resulting in a double Lorentzian profile as described by Eq. 2.7.

Alternatively, the angular and translational contributions to the QPD photovoltage signal can be deconvoluted by finding the autocorrelation of the signal[29–31]. The autocorrelation of the QPD signal is given by

$$C(\tau) = \langle V(t)V(t+\tau)\rangle, \tag{2.8}$$

where τ = t - t_0 is the time lag offset between the signal and itself. Furthermore, it should be noted that the autocorrelation and the power spectrum are Fourier conjugates. That is,

$$S(f) = \int_{-\infty}^{\infty} C(\tau)e^{-2\pi i f\tau}d\tau. \tag{2.9}$$

Therefore, one could also fit the autocorrelation of convoluted QPD photovoltage signals to a double exponential to deconvolute the center-of-mass motion from the angular fluctuations, but there is no distinct advantage to this method over the double Lorentzian power spectrum method.

2.3.1 Further signal processing considerations

Caution must be exercised when applying the analysis of Sec. 1.2.3 to experimentally obtained QPD signals, as the data acquisition is discrete and finite. For an experiment, the QPD is sampled with a frequency f_s for a time t_m. Typical values for these parameters are on the order of f_s = 100 kHz for t_m = 1 second. Here, the time between sampling events is $\Delta t = \frac{1}{f_s}$ = 10 μs and any sampling time is given by $t_j = j\Delta t$. For discretely-sampled signals, aliasing occurs for frequencies greater than the Nyquist frequency ($f_{Ny} = \frac{f_s}{2}$). Therefore, it is imperative to only fit signals over frequencies less than f_{Ny}. Furthermore, QPD power spectra will generally exhibit increased noise at low frequencies (f < 5 Hz). It is then advantageous to limit data analysis of QPD power spectra over frequencies $5 < f < f_{Ny}$ Hz.

The analysis described in Sec. 1.2.3 also assumes that the QPD photovoltage signals $V_{x,y}$ are independent of one another and that each quadrant of the QPD (Q1-Q4) has equal sensitivity. In fact, this would be the case if the trapping potential was perfectly symmetric about the beam axis. However, in practice this is often not the case. The lack of rotational symmetry in the optical trap can cause crosstalk between the QPD quadrants. Consequently, V$_x$ and V$_y$ are not independent of one another. The crosstalk can be minimized by mathematically transforming our QPD axes such that one direction lies along the major axis of the beam asymmetry and the other along the minor axis. As derived by Berg-Sorensen and Flyvbjerg[24], this transformation is realized by solving for the constants a and b in

$$\begin{aligned} S_{x'} &= S_x + 2aS_{xy} + a^2 S_y, \\ S_{y'} &= S_y + 2bS_{xy} + b^2 S_x, \\ S_{x'y'} &= (1+ab)\, S_{xy} + bS_x + aS_y \end{aligned} \tag{2.10}$$

that minimize the equation

$$\sum_f \frac{S^2_{x'y'}(f)}{S_x S_y}. \tag{2.11}$$

This then generates orthogonal QPD photovoltage signals in a coordinate frame that minimizes cross talk, given by

$$\begin{aligned} V_{x'}(t) &= V_x(t) + aV_y(t), \\ V_{y'}(t) &= V_y(t) + bV_x(t). \end{aligned} \tag{2.12}$$

Lastly, it is important to note that the Lorentzian form of the power spectrum given in Eqs. 1.24 and 2.7 assume continous sampling rather than finite sampling. Again Berg-Sorensen and Flyvbjerg[24] found that the exact form of the power spectrum from a finite-sampled QPD is given by

$$S(f) = \frac{(\Delta x)^2 \, \Delta t}{\left[1 + c^2 - 2c\cos\left(\frac{2\pi f}{f_s}\right)\right]}, \tag{2.13}$$

where

$$c = \exp\left[-\frac{\pi f_c}{f_{Ny}}\right], \tag{2.14}$$

and

$$\Delta x = \sqrt{\left(\frac{(1-c^2)\, D}{2\pi f_c}\right)}. \tag{2.15}$$

Least-squares fitting can be done with Eq. 2.13 and the solution is valid for QPD power spectra data for frequencies $0 < \mathrm{f} \leq \mathrm{f}_{Ny}$.

2.4 Calibration of position-sensitive detector in the back focal plane

As mentioned in Sec. 2.3, in order to obtain absolute displacement data from an optically trapped particle from the QPD photovoltage signals of a laser tweezer, the calibration coefficient β from Eq. 2.4 must be determined for the trapping setup. There are numerous ways available to calibrate a laser tweezer setup. A comprehensive comparison of calibration techniques has been covered by Sarshar et al.[32] and serves as a helpful guide for choosing a suitable technique for any particular application. For the laser tweezer in the Pauzauskie group, we follow a method developed by Tolić-Nørrelykke et al[33].

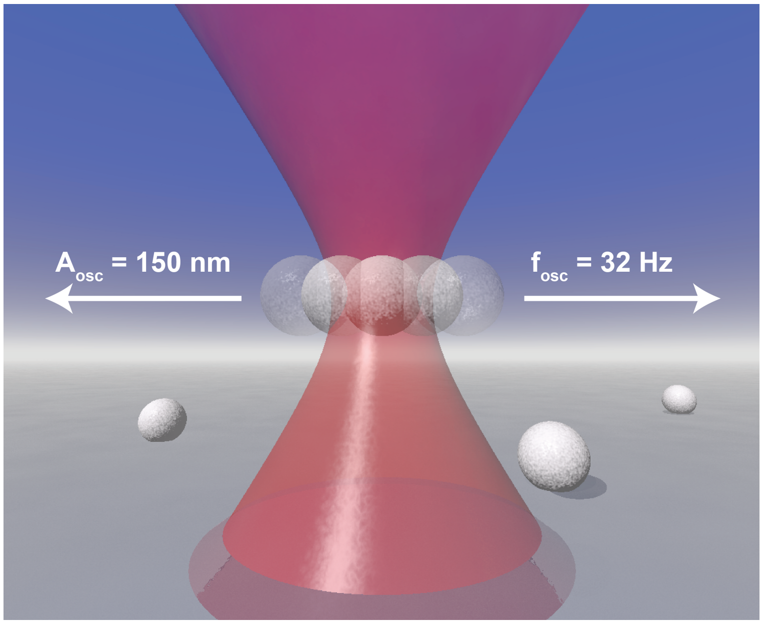

Figure 2.5: Illustration showing the piezostage oscillation method[33] for calibrating the QPD photovoltage signals.

In this method, the piezostage that holds the sample is oscillated in the x and y directions at a known frequency and amplitude (Fig. 2.5). The piezostage therefore obtains a time-dependent position function given by

$$x_{osc} = A_{osc} \sin\left(2\pi f_{osc} t\right), \tag{2.16}$$

where A_{osc} and f_{osc} are the oscillation amplitude and frequency, respectively. The velocity of the oscillating stage, and therefore the fluid in the sample chamber, is then given by $v_{osc} = \dot{x}_{osc}$ and subsequently modifies the drag force term in the Langevin equation (Eq. 1.14) becoming

$$F_{drag}(t) = \gamma(T)\left[\dot{x}(t) + v_{osc}(t)\right]. \tag{2.17}$$

Consequently, the power spectrum of the QPD photovoltage signal in the direction of oscillation becomes

$$\begin{aligned} S_{tot}(f) &= S(f) + S_{osc}(f) \\ &= \frac{D}{\pi^2\left(f_c^2 + f^2\right)} + \frac{A_{osc}^2}{2\left(1 + f_c^2/f_{osc}^2\right)}\delta\left(f, f_{osc}\right), \end{aligned} \tag{2.18}$$

where $\delta\left(f, f_{osc}\right)$ is the Kronecker delta function. Figure 2.6 shows an example experimental power spectrum of an optically trapped particle that has been oscillated at an amplitude A_{osc} = 150 nm and a frequency f_{osc} = 32 Hz.

We therefore know that the trapped particle should experience an additional increase in its motion at the oscillation frequency of

$$W_{th}\left(f_{osc}\right) = \frac{A_{osc}^2}{2\left(1 + f_c^2/f_{osc}^2\right)}, \tag{2.19}$$

which has physical units of [m^2]. Furthermore, we can experimentally determine the increase in the power spectrum as shown in Fig. 2.6, which has units of [V^2]. Hence, we can obtain the calibration coefficient β (having units of [m/V]) by taking the square root of the ratio of W_{th} to W_{exp}. That is,

$$\beta = \sqrt{\frac{W_{th}}{W_{exp}}}. \tag{2.20}$$

As the QPD photovoltage signal is dependent on the laser power as well as the size, shape, and optical properties of the particle in the laser trap, it is important to note that the

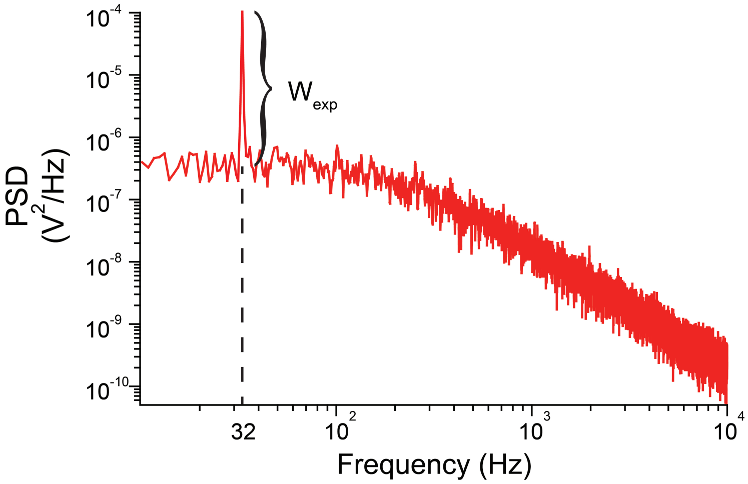

Figure 2.6: Example QPD photovoltage power spectrum resulting from oscillating an optically trapped particle at a frequency of 32 Hz and amplitude of 150 nm resulting in a peak at the oscillation frequency of magnitude W_{exp}.

calibration coefficient β will change as any of these parameters change. With that in mind, this calibration method can then be applied to obtain absolute quantitative parameters such as the trapping force, the particle diffusion coefficient, or particle size via power spectrum analysis of the QPD photovoltage signals.

2.5 Temperature extraction methods

With an understanding of the relevant physics that govern the dynamics of an optically trapped particle as well as a method to quantitatively monitor those dynamics via power spectrum analysis of QPD photovoltage signals, we can now study the photothermal responses of individual engineered nanoparticles with a laser tweezer system. Determining the local temperature of laser-irradiated micro- and nanoparticles in aqueous media is important in many areas of research, including photothermal cancer therapy[34, 35], particle tracking[36], and targeted drug payload delivery[37]. Laser traps have been used to measure the temperature of individually trapped particles, using both direct signal processing methods[31–33, 38, 39], as well as indirect experimental methods[40, 41]. Here, we outline methods developed during my PhD research in the Pauzauskie lab to extract the temperature from optically trapped particles: 1) a ratio method for low-absorbing particles, and 2) the piezostage method for absolute temperature measurements.

2.5.1 Ratio method for temperature changes with low-absorbing particles

We recall from Eqs. 1.24, 2.7, and 2.13 that a diffusion coefficient D can be obtained by applying non-linear least squares fitting on an experimental QPD photovoltage signal power spectrum. We further recall that the diffusion coefficient is related to the local temperature, particle size, particle morphology, and the local solvent by Eqs. 1.11 and 1.12. Assuming the QPD signals are uncalibrated, we can rearrange Eqs. 1.11 and 1.12 to obtain

$$\widetilde{\left(\frac{T}{\eta(T)}\right)} = \frac{gD^V}{k_B}, \tag{2.21}$$

where D^V is the uncalibrated diffusion coefficient in units of [V^2/s]. The function $T/\eta(T)$ is known for multiple solvents for typical as well as superheated temperatures (e.g. H_2O[42, 43] and D_2O[43]). However, Eq. 2.21 is marked with a tilde since the units are not in [$K/\mu Pa \cdot s$] due to the diffusion coefficient D^V being uncalibrated and having units of [V^2/s].

One way to avoid signal calibration and obtain temperatures with proper units is to take the ratio of the uncalibrated diffusion coefficient from QPD photovoltage signals V_x and V_y that have been normalized to the sum signal $V_z = V_{sum}$ (Eq. 2.3). Normalization to the sum signal is performed to ensure that the calibration coefficients are equal at different laser powers[44]. If we constrain our analysis to low absorbing particles, we can make a reasonable first order assumption that the heating of the trapped particle at low trapping powers is negligible, and therefore $T = T_{room}$. Therefore, if we take the ratio of two assumed calibrated diffusion coefficients obtained at different laser powers, we obtain

$$\frac{D_2}{D_1} = \frac{[k_B T_2/g\eta(T_2)]}{[k_B T_1/g\eta(T_1)]}\frac{\beta_2^2}{\beta_1^2}. \tag{2.22}$$

If measurement 1 is done at low powers ($T_1 = T_{room}$) and the QPD photovoltage x or y signals are normalized to the sum signal ($\beta_1 = \beta_2 = \beta$), then rearranging Eq. 2.22 for $T_2/\eta(T_2)$ we get

$$\frac{T_2}{\eta(T_2)} = \frac{D_2}{D_1}\frac{T_{room}}{\eta(T_{room})}. \tag{2.23}$$

We see from Eq. 2.23 that the calibration coefficients cancel each other out. Therefore, it is unneccesary that calibrated diffusion coefficients are used and instead uncalibrated diffusion coefficients (D^V) can be used. Since the value of $T_{room}/\eta(T_{room})$ is typically a known quantity (Fig. 2.7b), one simply needs to extract the uncalibrated diffusion coefficients from normalized QPD photovoltage signals at different laser powers to determine the value $T_2/\eta(T_2)$. For most trapping solvents, the viscosity as a function of temperature is typically well modeled by the equation

$$\eta(T) = \eta_\infty \exp\left[\frac{A}{(T - T_{VF})}\right]. \tag{2.24}$$

The fitting parameters A, η_∞, and T_{VF} are obtained by performing nonlinear least-squares fitting on temperature-dependent viscosity data[42, 43] which are used to produce the fits shown in Fig. 2.7a. As the temperature-dependence of $\eta(T)$ is known for most typical trapping solvents, the value $T_2/\eta(T_2)$ can then be compared to the function $f(T) = T/\eta(T)$ (Fig. 2.7b) to determine the final temperature T_2.

A nice feature of this method is that temperature changes can be obtained without having to know the size and morphology of the trapped particle and without calibrating the trap. However, there are also multiple drawbacks to this method. For one, even for low laser powers and non-absorbing particles, the large fields at the focus are likely non-negligible and therefore the base temperature T_1 is likely a few degrees higher than the temperature of the chamber. One way to mitigate this is to use D_2O as a trapping solvent, as it has been shown to minimally absorb NIR wavelengths[45]. Furthermore, as the ratio is based on two separate experimentally fit signals, errors in the extracted fit parameters propagate giving rise to large error bars. Still, the method has been shown to give results that are consistent with previously reported temperature changes of trapped silicon nanowires[31].

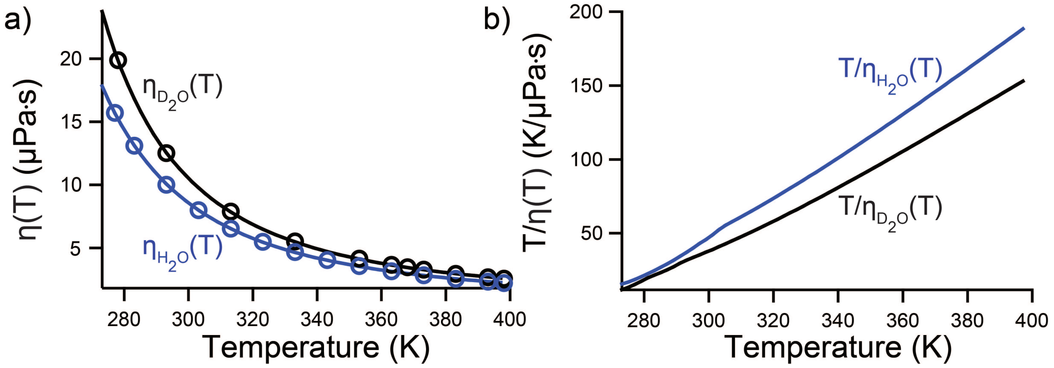

Figure 2.7: a) Plots showing temperature-dependent viscosity data (circles) and fits to Eq. 2.24 (lines) for H_2O (η_{H_2O}(T), blue) and D_2O (η_{D_2O}(T), black). The fitting parameters for H_2O are A = 528.8 K, η_∞ = 27.21 μPa·s, and T_{VF} = 146.7 K. The fitting parameters for D_2O are A = 470.1 K, η_∞ = 35.48 μPa·s, and T_{VF} = 161.3 K. b) Corresponding plots of T/η(T).

2.5.2 Piezostage oscillation method for absolute temperatures

Rather than restricting our temperature analysis to low-absorbing particles and relative temperature changes using normalized QPD photovoltage signals, it is often beneficial to find the absolute temperature of a generic trapped particle. In order to obtain the absolute temperature, the QPD photovoltage signals must be properly calibrated using the methods described in Sec 2.4. Once the QPD signals are calibrated, absolute temperatures can be obtained by multiplying Eq. 2.21 by the square of the extracted calibration coefficient β to obtain the function T/η(T), shown in Eq. 2.25.

$$\frac{T}{\eta(T)} = \frac{gD^V}{k_B}\beta^2 \tag{2.25}$$

In this case, the tilde has been dropped from Eq. 2.21 to signify that the units are correct due to QPD signal calibration. This method is beneficial in that it allows for an absolute particle temperature for a generic trapped particle, as long as there is viscosity data for the temperature range of interest. However, its key drawback is that the size of the particle must be known in order to calculate the temperature. Errors in the size of the trapped particle result in increased confidence intervals of the extracted temperature.

Chapter 3

PREDICTING TEMPERATURES OF LASER IRRADIATED NANOWIRES

3.1 Introduction

Before we perform temperature extraction trapping experiments on engineered particles, it is important to understand the mechanisms that lead to photothermal heating, identify the key heating parameters, and predict the temperatures of optically trapped particles. In this chapter, we will develop multiple models that will allow us to predict the temperatures of laser irradiated one-dimensional nanoparticles (i.e. nanowires). We will start off by describing the general approach to solving for the internal temperature of a laser irradiated nanoparticle. This approach will then be applied to 3 distinct cases: 1) pulsed laser heating of bound nanowires in vacuum, 2) laser heating of infinite nanowires in solution, and 3) laser heating of finite nanowires in solution. Lastly, we will apply the developed model to predict the temperature of optically trapped silicon nanowires and compare our predictions to experimental temperatures extracted using the methods described in Sec. 2.5.1.

3.2 Approaching the heating problem

The temperature (T) of a material is determined by the amount of energy in the form of heat (H) in the material. Heat and temperature are related by the expression

$$H = C_p m T, \tag{3.1}$$

where C_p is the specific heat capacity with units $\left[\frac{\mathrm{J}}{\mathrm{kg \cdot K}}\right]$, and m is the mass of the material. The volumetric thermal energy density (ρ_E) of a material can then be found by dividing Eq.

3.1 by a volume element (V) of the material, shown as

$$\rho_E = C_p \frac{m}{V} T = C_p \rho T, \tag{3.2}$$

where ρ is the mass density. Moreover, the rate at which heat transfers in a material is expressed by

$$\dot{H} = \frac{\partial H}{\partial t}. \tag{3.3}$$

The heat flux μ can then be defined at the heat transfer rate $\dot{\mathrm{H}}$ through an area element A, or

$$\mu = \dot{H}/A. \tag{3.4}$$

Suppose that we have a volume element V in some material. For a system with no heat source or sink, conservation of energy then requires that a change of the thermal energy density ρ_E within the volume element over an arbitrary time interval must be equal to a corresponding net heat flux μ through the boundaries of the volume element. If we shrink the volume element and time interval to become infinitesimal, this relationship then becomes

$$\frac{\partial \rho_E}{\partial t} + \nabla \mu = 0, \tag{3.5}$$

where ∇ is the spatial gradient operator. Equation 3.5 is often written as

$$C_p \rho \frac{\partial T}{\partial t} = -\nabla \mu. \tag{3.6}$$

Furthermore, the Fourier's law of heat conduction tells us that the heat flux μ at a point in a material is proportional to the spatial temperature gradient at that point, where the proportionality constant is called the thermal conductivity κ which describes the material's ability to conduct heat. This then implies that

$$\mu = -\kappa \nabla T \tag{3.7}$$

Substituting Eq. 3.7 into the right-hand side of Eq. 3.6, we obtain the heat conduction equation for a system with no heat source or sink

$$C_p \rho \frac{\partial T}{\partial t} = \kappa \nabla^2 T. \tag{3.8}$$

To account for a system with a heat source or sink, Eq. 3.8 is altered by adding a volumetric heating rate term (S) to the right-hand side

$$C_p\rho\frac{\partial T}{\partial t} = \kappa\nabla^2 T + S, \tag{3.9}$$

where S has units of $\left[\frac{\mathrm{W}}{\mathrm{m}^3}\right]$.

When attempting to predict the temperature of laser-irradiated nanowires, Eq. 3.9 must be solved. Here, the volumetric heating rate S is determined from the laser absorption by nanowire which generates heat. Furthermore, Eq. 3.9 can only be solved by applying appropriate boundary conditions which are dependent upon the framework of the problem. Yet, without knowing the nature of the problem, it is still illuminating to discuss the general approach we will take to solving Eq. 3.9.

First, the heating source S from the laser needs to be determined. In this case, electromagnetic energy from the laser is being absorbed by the nanowire which subsequently establishes internal electric fields within the nanowire. These internal electric fields then exert forces on charges within the material and act to Joule heat the nanowire. For special cases such as a infinite, uniform-diameter nanowire irradiated with a monochromatic planewave, the distribution of the internal electric fields within the nanowire can be solved analytically and the source can therefore be derived. If the internal electric fields are assumed to be uniform, the source can be found by taking the average absorbed energy of the incident laser by using a calculated absorption efficiency coefficient. If the internal electric fields of the nanowire are not able to be calculated, they can nevertheless be simulated by using computational techniques such as finite-difference time domain, discrete dipole approximation, or finite element methods.

Once the source term S has been determined, the next step is to turn Eq. 3.9 dimensionless by transforming the relevant variables in the equation into dimensionless variables. Nondimensionalization is not a necessary step but still important in that it makes it easier to recognize functional forms to determine when certain mathematical techniques can be applied as well as allows for determining which parameters play important or negligible roles in your problem. Furthermore, analyzing a dimensionless equation can give a better idea as to how the fundamental time, length, and (in our case) temperature scales for the problem.

With Eq. 3.9 now nondimensionalized, the solution of the dimensionless homogeneous equation (neglecting the source term) is then assumed to be a product of multiple functions with separate independent variables. Typically, one of the functions is dependent on the dimensionless time variable and the other functions are each dependent on a dimensionless spatial variable. When this assumed product solution is inserted into the dimensionless heat conduction equation, we can alter the resulting equation so that the time and spatial variables occur on different sides of the equation, thereby implying that each side is equal to a constant value. This sets up an eigenvalue problem for both the spatial and temporal sides of the equation. For the models we will look at, we will show that the solutions to the spatial differential eigenvalue equation can be cast into a regular Sturm-Liouville form with appropriate boundary conditions which ensures real increasing eigenvalues with corresponding unique eigenfunctions which form an orthogonal basis.

The spatial eigenfunction series solutions are the same for the homogenous as well as the inhomogeneous (including the source term) equations. Therefore, we apply the same separation of variables method for the solution of the inhomogeneous equation, only now we know the spatial eigenfunction series solutions. Plugging in the assumed product solution of the inhomogeneous equation and rearranging such that the dimensionless source term is on the right-hand side of the equation, we then take advantage of the orthogonality of the spatial series solutions by multiplying both sides by the product of the spatial series solutions with an appropriate weighting factor and integrating over the dimensionless variable space. Following this operation, dividing by the squared norms of the spatial eigenfunctions results in a differential equation of the temporal function on the left-hand side and a multiple integral of the product of the orthonormal spatial eigenfunctions, the dimensionless source term, and the appropriate weighting factor on the right-hand side of the equation. The temporal differential equation on the left-hand side can be solved by applying an exponential integrating factor and integrating over the dimensionless time variable on both sides of the equation. After dividing both sides by an exponential prefactor, the temporal solution to the product solution is found. With the temporal solution found, the complete dimensionless temperature solution to the inhomogeneous solution can then be analytically solved and a time- and spatial-dependent physical temperature for the laser-irradiated nanowire can be calculated.

3.3 Pulsed laser heating of supported nanowires

The first framework we will apply our above analysis to is that of a tapered nanowire in vacuum supported at its base by a temperature-controlled surface irradiated by a pulsed laser at the nanowire tip. This is admittedly not a directly relevant framework for laser heating of nanowires in an optical trap, but it allows us to comment on time-dependent pulsed heating of both uniform and non-uniform nanowires where heat transport is limited to one direction by a heat sink at the nanowire's base. Furthermore, this system is almost identical to the setup of a laser-assisted atom probe experiment.

Laser-assisted atom-probe tomography (LA-APT) and the local electrode atom probe (LEAP) tomograph play an important role in the characterization of semiconductor nanomaterials. This involves the use of voltage and laser pulses to field evaporate ions from the tip of needle-like specimens[46], such as silicon nanowires[47, 48]. Use of a local electrode geometry decreases the fields needed for ion evaporation and increases the pulse rate that can be attained. For these experiments, it is desirable to achieve high evaporation rates to permit a wide range of parameters to be explored. In semiconductor applications, the parameters of interest include growth rates, compositions, dopant concentrations, and material geometries[49].

Numerous experimental and theoretical studies of the time-dependent tip temperature, temperature distribution, and cooling time for a voltage- or laser-pulsed field ion microscope specimen have been published. Numerical computations include those of Bunton et al.[46], Seidman and Scanlan[50], Liu and Tsong[51], Liu et al.[52], and, more recently, Perea et al.[48]. Most of the analyses use a one-dimensional heat conduction model, usually assuming constant thermal properties. Using a pump-probe scheme to scan the lattice temperature of a metallic tip after the laser pulse, Vurpillot et al.[53] concluded that the one-dimensional model is valid, at least on the nanosecond time scale.

However, the earlier analyses do not take into account adequately the dependence of the thermal conductivity of the specimen on the size of the specimen. Volz and Chen[54] pointed out that the effective thermal conductivity of small structures is a function of both boundary and internal phonon scattering and that the small cross section of nanowires leads to a significant reduction of the thermal conductivity compared to bulk material. They used a molecular dynamics method to explore the thermal conductivity of nanowires. Li et al.[55] measured the thermal conductivity of silicon nanowires as a function of diameter and temperature, and Perea et al.[48] used those results in an analysis of the tip temperature and cooling time of silicon nanowires. They did not model the time-dependent temperature distribution during the period of the pulse, but they numerically computed the decay of the tip temperature during the cooling period for silicon nanowires of uniform diameter and for tapered wires.

The purpose of this section is to present an analytical approach to predicting peak temperatures as well as heating and cooling rates of one-dimensional structures that are irradiated by a laser pulse. The analysis takes into account the size-dependency of thermal parameters and generalizes system variables such as specimen size, shape, and optical properties which provides a powerful tool for identifying the key parameters and variables that affect heat generation and dissipation in a system of interest. For the application of the theory we focus on silicon specimens with the aim of determining the effects of taper angle, thermal properties, and laser wavelength and polarization on peak specimen temperature and their heating and cooling rate. Comparison with previous numerical calculations as well as experimental data will allow us to comment on the relative importance of the morphological, optical, and thermal parameters of the system.

The remainder of the section is organized as follows. In Sec. 3.3.1 the general theoretical model is presented. The model is then applied to uniform radius wires in Sec. 3.3.2 as well as wires with tapered radii in Sec. 3.3.3, where radius-dependent thermal properties are appropriately treated. Simulations for crystalline silicon and amorphous silicon nanowires that show the dependencies of taper angle and thermal properties on peak specimen temperature and cooling rates are detailed in Sec. 3.3.4. The model is then used to simulate and comment on LA-APT experimental data which is presented and discussed in Sec. 3.3.5. Finally, Sec. 3.3.6 and 3.3.7 summarizes the results and points out some interesting future applications.

3.3.1 Initial setup of the model

Consider the tapered wire with the geometry shown in Fig. 3.1. Although the beam axis is often shifted by a small angle from the normal to the sample axis, that angle is small. Here, we shall consider the beam axis to be 7° from normal to the specimen axis with the center of the beam intersecting the tip of the specimen. For a Gaussian beam having irradiance I_0 at the centerline, the z-dependent irradiance is given by

$$I(z) = I_0 \exp\left[-\frac{2z^2}{w_0^2}\right], \tag{3.10}$$

in which w_0 is the beam waist. The centerline irradiance is related to the beam power by

$$P_0 = \frac{1}{2}\pi I_0 w_0^2. \tag{3.11}$$

For one-dimensional heat conduction (neglecting radiation heat transfer to or from the surfaces) the energy equation for the period during the pulse is given by

$$\rho C_p \frac{\partial T}{\partial t} = \frac{1}{r^2}\frac{\partial}{\partial z}\left(\kappa r^2 \frac{\partial T}{\partial z}\right) + \frac{S(z)}{r^2}, \tag{3.12}$$

where the heat source function for a Gaussian beam is

$$\frac{S(z)}{r^2} = \frac{2Q_{abs}}{\pi r} I_0 \exp\left[-\frac{2z^2}{w_0^2}\right]. \tag{3.13}$$

Equation 3.12 is the analog of Eq. 3.9 detailed in Sec. 3.2 and can be derived by considering the energy balance shown in Fig. 3.2, which is given by

$$\pi r^2 dz \rho C_p \frac{\partial T}{\partial t} = \left(\pi r^2 q_z|_z - \pi r^2 q_z|_{z+dz}\right) + I(z) Q_{abs}(r) 2r dz. \tag{3.14}$$

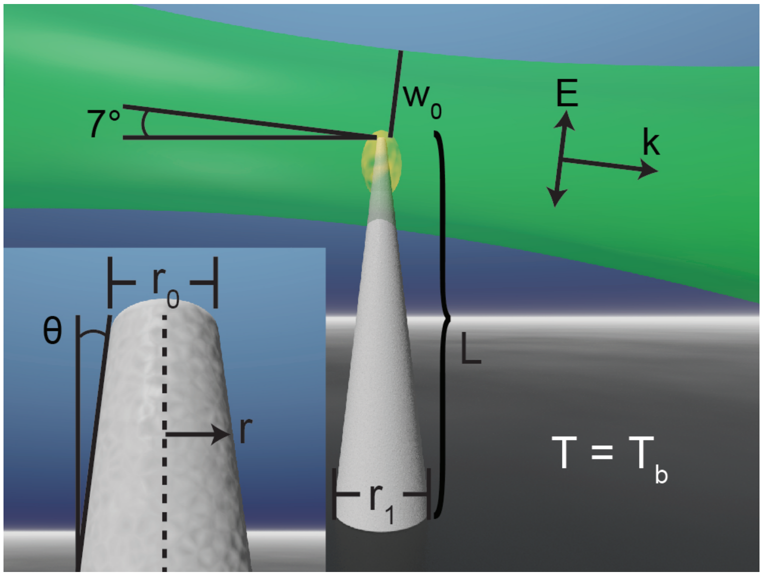

Figure 3.1: Configuration of a tapered wire irradiated by a focused pulsed laser with a Gaussian intensity profile.

In the model, after the pulse implies that S(z) = 0. For a tapered wire the absorption efficiency, Q_{abs}, is a function of z since the radius changes with z. To obtain the local Q_{abs} we shall apply Mie theory for a long rod of constant radius illuminated by a planewave at an incidence angle of 7° to approximate Q_{abs} at each axial position, that is, we model a conical rod as a stack of cylinders with varying radii as did Bodganowicz et al.[56, 57]. We must also make an assumption about the polarization of the laser beam to compute Q_{abs}, but we first examine the special case of a wire with a uniform diameter.

3.3.2 Uniform nanowires

For a wire with $r = r_0 =$ constant, the energy equation reduces to

$$\rho C_p \frac{\partial T}{\partial t} = \frac{\partial}{\partial z}\left(\kappa \frac{\partial T}{\partial z}\right) + \frac{2Q_{abs}}{\pi r_0} I_0 \exp\left[-\frac{2z^2}{w_0^2}\right]. \qquad (3.15)$$

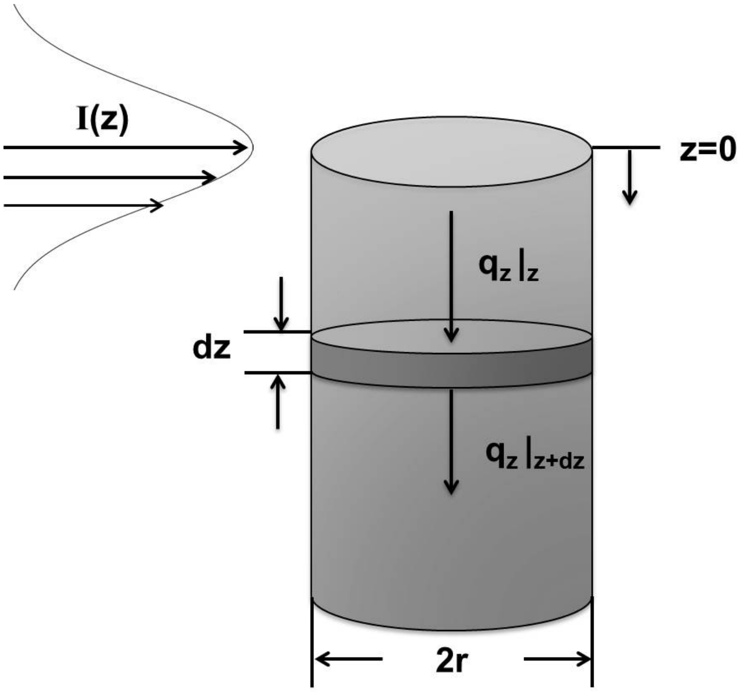

Figure 3.2: Schematic showing one-dimensional heat transfer with a heating source from a pulsed laser with a Gaussian intensity distribution.

It is important to note that the thermal diffusivity, $\alpha = \kappa/\rho \mathrm{C}_p$, is temperature dependent as both κ and C_p have a strong temperature dependence. As we shall show, the choice of which temperature we select for the thermal properties affects the time scale of the heating and cooling process, which involves the thermal diffusivity, and the maximum temperature, which depends on the thermal conductivity. Consequently, it is convenient to approximate the thermal properties as constant evaluated at the mean of the wire temperature at the end of the laser pulse in the irradiated region.

Thus, for constant α we introduce nondimensional variables and parameters to give

$$\frac{\partial \Theta}{\partial \tau} = \frac{\partial^2 \Theta}{\partial \zeta^2} + S^*(\zeta). \tag{3.16}$$

The nondimensional terms are given by

$$\Theta = \frac{T - T_b}{T_b}, \tau = \frac{\alpha}{L^2}t, \zeta = \frac{z}{L}, S^*(\zeta) = \frac{2L^2 Q_{abs} I_0}{\pi r_0 \kappa T_b} \exp\left[-\frac{2L^2\zeta^2}{w_0^2}\right]. \tag{3.17}$$

The boundary conditions are

$$\Theta(\zeta_1, \tau) = 0, \frac{\partial \Theta}{\partial \zeta}(\zeta_0, \tau) = 0. \tag{3.18}$$

Using the separated variables product solution, we assume a solution of the form

$$\Theta(\zeta, \tau) = \sum_{n=1}^{\infty} F_n(\tau) G_n(\zeta). \tag{3.19}$$

The orthonormal eigenfunctions are given by

$$G_n(\zeta) = \sqrt{2}\cos(\gamma_n \zeta) = \sqrt{2}\cos\left[(2n-1)\frac{\pi}{2}\zeta\right], n = 1, 2, 3, ... \tag{3.20}$$

Substituting the assumed solution in the energy equation and applying orthogonality, one obtains

$$\Psi_n = \frac{dF_n(\tau)}{d\tau} + \gamma_n^2 F_n(\tau) = \sqrt{2}\int_0^1 S^*(\zeta')\cos(\gamma_n \zeta')d\zeta'. \tag{3.21}$$

The integral Ψ_n is readily obtained using Matlab or any appropriate numerical method, and we note that it involves the absorption coefficient.

If the irradiance I_0 is constant during the pulse, Eq. 3.21 can be integrated to yield the solution

$$\Theta(\zeta, \tau) = \sqrt{2}\sum_{n=1}^{\infty} \frac{\left(1 - e^{-\gamma_n^2 \tau}\right)}{\gamma_n^2} \Psi_n \cos(\gamma_n \zeta) \tag{3.22}$$

for $\tau \leq \Delta\tau$, in which $\Delta\tau$ is the dimensionless pulse width defined by $\Delta\tau = \alpha \Delta \mathrm{t}/\mathrm{L}^2$.

Likewise, the solution for the cooling period is given by

$$\Theta^*(\zeta, \tau) = \sqrt{2}\sum_{n=1}^{\infty} e^{-\gamma_n^2(\tau - \Delta\tau)} \frac{\left(1 - e^{-\gamma_n^2 \Delta\tau}\right)}{\gamma_n^2} \Psi_n \cos(\gamma_n \zeta) \tag{3.23}$$

for $\tau \geq \Delta\tau$.

3.3.3 Tapered nanowires

The analysis of tapered specimens is more complicated because the thermal conductivity depends on the radius as well as the temperature and the absorption coefficient also depends on the radius, but some approximations can be made to facilitate solution. To account for the dependence on radius, thermal conductivity data in the range of sizes and temperatures of interest here can be fitted to an equation of the form

$$\kappa = \kappa_0 \left(\frac{r}{r_0}\right)^m, \tag{3.24}$$

in which m is a constant. Therefore, the energy equation becomes

$$\frac{\partial T}{\partial t} = \frac{\alpha_0}{r_0^m r^2}\frac{\partial}{\partial z}\left(r^{2+m}\frac{\partial T}{\partial z}\right) + \frac{S(z)}{\rho C_p}. \tag{3.25}$$

For the geometry shown in Fig. 3.1 the radius is related to the axial position by

$$r = r_0 + z\tan(\theta). \tag{3.26}$$

Using Eq. 3.26 and applying the chain rule for derivatives to eliminate z, we obtain

$$\frac{\partial T}{\partial t} = \frac{\alpha_0 \tan^2(\theta)}{r_0^m r^2}\frac{\partial}{\partial r}\left(r^{2+m}\frac{\partial T}{\partial r}\right) + \frac{S(r)}{\rho C_p}. \tag{3.27}$$

In this case we can introduce dimensionless variable and parameters defined by

$$\Theta = \frac{T - T_b}{T_b}, \xi = \frac{r}{r_0}, \tau = \frac{\alpha_0 \tan^2(\theta)}{r_0^2}t, \tag{3.28}$$

where α_0 is an effective thermal diffusivity given by $\alpha_0 = \kappa_0/\rho \mathrm{C}_p$. Using Eq. 3.27 the energy equation transforms to

$$\frac{\partial \Theta}{\partial \tau} = \frac{1}{\xi^2}\frac{\partial}{\partial \xi}\left(\xi^{2+m}\frac{\partial \Theta}{\partial \xi}\right) + S^*(\xi), \tag{3.29}$$

where the dimensionless source function is

$$S^*(\xi) = \frac{2r_0 I_0 Q_{abs}(\xi)}{\pi \kappa_0 T_b \xi \tan^2(\theta)} \exp\left\{-2\left[\frac{r_0(\xi - 1)}{w_0 \tan(\theta)}\right]^2\right\}. \tag{3.30}$$

Again we apply a separated variable product solution of the form

$$\Theta(\xi, \tau) = \sum_{n=1}^{\infty} f_n(\tau) g_n(\xi). \tag{3.31}$$

The eigenfunctions satisfy the Sturm-Liouville problem

$$\frac{d}{d\xi}\left(\xi^{2+m}\frac{dg_n}{d\xi}\right)+\lambda_n^2\xi^2 g_n=0, \tag{3.32}$$

with boundary conditions

$$\frac{dg_n}{\xi}(\xi_0)=0, g_n(\xi_1)=0, \tag{3.33}$$

where λ_n are the real eigenvalues, $\xi_0 = 1$, and $\xi_1 = 1+(\mathrm{L}/\mathrm{r}_0)\tan(\theta)$.

The eigenfunctions that satisfy this problem are given by

$$g_n(\xi)=\xi^{-\frac{m+1}{2}}Z_p\left[\frac{2\lambda_n}{2-m}\xi^{\frac{2-m}{2}}\right], \tag{3.34}$$

where p $= -\sqrt{(m+1)^2}/(m-2)$, and $Z_p(x)$ takes on one of two forms depending on the value of p. For p equal to 0 or a positive integer,

$$Z_p(x)=AJ_p(x)+BY_p(x). \tag{3.35}$$

For all other values of p,

$$Z_p(x)=AJ_p(x)+BJ_{-p}(x). \tag{3.36}$$

Restricting our analysis to the former case (p=0,1,2,...), Eq. 3.34 becomes

$$g_n(\xi)=\xi^{-\frac{m+1}{2}}\left[J_p\left(\frac{2\lambda_n}{2-m}\xi^{\frac{2-m}{2}}\right)+B_nY_p\left(\frac{2\lambda_n}{2-m}\xi^{\frac{2-m}{2}}\right)\right], \tag{3.37}$$

in which the boundary condition at the wire base yields

$$B_n=-\frac{J_p\left(\frac{2\lambda_n}{2-m}\xi_1^{\frac{2-m}{2}}\right)}{Y_p\left(\frac{2\lambda_n}{2-m}\xi_1^{\frac{2-m}{2}}\right)}. \tag{3.38}$$

Defining the norms of the eigenfunctions as

$$\|g_n\|^2=\int_{\xi_0}^{\xi_1}\xi'^2 g_n^2(\xi')d\xi', \tag{3.39}$$

the orthonormal eigenfunctions are defined by

$$u_n(\xi)=\frac{g_n(\xi)}{\|g_n\|}. \tag{3.40}$$

Given that Ψ_n is defined as

$$\Psi_n = \frac{2r_0 I_0}{\pi \kappa_0 T_b \tan^2(\theta)} \int_{\xi_0}^{\xi_1} \xi' Q_{abs}(\xi') \exp\left[-\frac{2r_0^2 \left(\xi' - 1\right)^2}{w_0^2 \tan^2(\theta)}\right] u_n(\xi') d\xi', \tag{3.41}$$

the solution for the heating period ($\tau \leq \Delta\tau$) becomes

$$\Theta(\xi, \tau) = \sum_{n=1}^{\infty} \frac{\left(1 - e^{-\lambda_n^2 \tau}\right)}{\lambda_n^2} \Psi_n u_n(\xi). \tag{3.42}$$

For the cooling period ($\tau \geq \Delta\tau$) the solution is given by

$$\Theta^*(\xi, \tau) = \sum_{n=1}^{\infty} e^{-\lambda_n^2(\tau - \Delta\tau)} \frac{\left(1 - e^{-\lambda_n^2 \Delta\tau}\right)}{\lambda_n^2} \Psi_n u_n(\xi). \tag{3.43}$$

3.3.4 Simulations

Crystalline silicon nanowires

In the analysis presented above we have considered the effective thermal diffusivity, α_0, to be constant having some mean value in the temperature range encountered. To examine the effect of such an assumption we compared our results with those of Perea et al.[48] who used a numerical solution of the energy equation to take into account the temperature and size dependence of the thermal conductivity. They assumed an initial condition of the temperature distribution for the cooling period to be Gaussian, which, as we show below, is questionable for tapered samples. They used a pulsed laser with a wavelength of 532 nm, a pulse frequency of 100 kHz, a pulse width of 10 ps, and a pulse energy ranging from 20 to 100 pJ ($2 \leq P_0 \leq 10$ W). The representative silicon nanowire specimen had a tip diameter of 30 nm ($r_0 = 15$ nm) and a length, L, of 10 μm. The Gaussian beam was reported to have a spot size of 1 μm at FWHM. For these conditions one obtains $w_0 = 0.849$ μm, and centerline irradiances from 1.765x10^{12} to 8.826x10^{12} W/m^2. The taper angle varied from 0° to 4°.

For the simulation of heat transfer for crystalline silicon nanowires in vacuum, we used a complex refractive index of n = 4.136 + 0.010205i[58] and specific heat data reported by Flubacher et al.[59]. Furthermore, using the results of Li et al.[55], we performed a nonlinear least-squares fit of the size-dependent thermal conductivity data to determine the exponent, m, in Eq. 3.24, obtaining m = 1. For temperatures greater than about 70 K the temperature-dependent values of κ_0 scatter about $\kappa_0 = 12$ W/m·K. In this case, the eigenfunctions $g_n(\xi)$ for the tapered wire given by Eq. 3.37 become

$$g_n(\xi) = \xi^{-1}\left[J_2\left(2\lambda_n\sqrt{\xi}\right) + B_n Y_2\left(2\lambda_n\sqrt{\xi}\right)\right], \tag{3.44}$$

where

$$B_n = -\frac{J_2\left(2\lambda_n\sqrt{\xi_1}\right)}{Y_2\left(2\lambda_n\sqrt{\xi_1}\right)}. \tag{3.45}$$

From the boundary condition at the tip, the eigenvalues satisfy the transcendental equation

$$0 = 2\left[J_2\left(2\lambda_n\sqrt{\xi_0}\right) + B_n Y_2\left(2\lambda_n\sqrt{\xi_0}\right)\right] - \lambda_n\sqrt{\xi_0}\left[J_1\left(2\lambda_n\sqrt{\xi_0}\right) + B_n Y_1\left(2\lambda_n\sqrt{\xi_0}\right)\right]. \tag{3.46}$$

Table 3.1 lists the first few eigenvalues and norms for nanowire tapers of 1°, 2°, and 4°. Furthermore, we note that the integral in Eq. 3.41 involves the radius-dependent absorption coefficient. Since the radius varies substantially with a tapered wire we need to consider how

Table 3.1: A partial list of eigenvalues and norms used for silicon nanowire simulations presented in Sec. 3.3.4.

		n				
		1	**2**	**3**	**4**	**5**
θ=1°	$\boldsymbol{\lambda_n}$	0.5820	1.0203	1.4793	1.9592	2.4529
	$\|\|\mathbf{g_n}\|\|$	1.5458	1.1512	1.0130	1.3339	525.3549
θ=2°	$\boldsymbol{\lambda_n}$	0.3769	0.6558	0.9358	1.2217	1.5137
	$\|\|\mathbf{g_n}\|\|$	2.4108	1.8313	1.4969	1.2838	1.1883
θ=4°	$\boldsymbol{\lambda_n}$	0.2497	0.4329	0.6141	0.7958	0.9790
	$\|\|\mathbf{g_n}\|\|$	3.6423	2.8014	2.3457	2.0387	1.8119

Q_{abs} changes over the length of the wire, which is presented in Fig. 3.3a for a beam that is polarized parallel with the wire axis (TM) and with a wavelength of 532 nm. The taper angle has a large effect on Q_{abs}, and morphology-dependent resonances are seen in the absorption profiles for angles greater than 1° (for diameters greater than 60 nm). Since the resonances are superposed on the irradiance of the Gaussian beam, the heating is highly non-uniform; a result also demonstrated in the simulations of Koelling et al.[60] and which appear in the scanning electron micrographs of Kelly et al.[61].

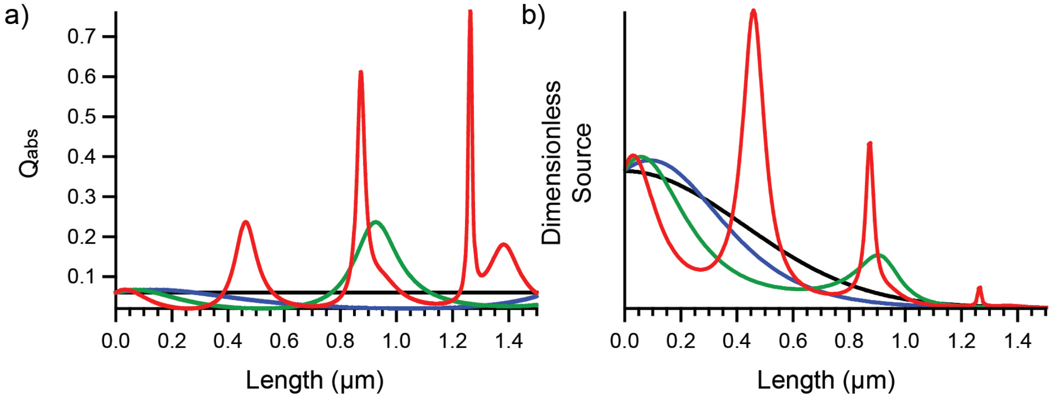

Figure 3.3: a) Absorption efficiency Q_{abs} of silicon nanowires with taper angles of $\theta = 0°$(black), 1°(blue), 2°(green), and 4°(red) in vacuum irradiated with a 532nm wavelength TM-polarized laser at 7° incidence. b) Dimensionless source functions (Eq. 3.30, normalized to the wire tip value) showing Q_{abs} resonances superposed with the irradiance of the Gaussian beam.

This effect can be understood by considering the corresponding dimensionless source functions defined by Eq. 3.30, presented in Fig. 3.3b. To help qualitatively compare the heating source profiles, the dimensionless source functions in Fig. 3.3b have been normalized to the wire tip value. For the wire with uniform diameter the source function has the expected Gaussian profile, but significant distortion of that profile arises for tapered specimens. In the computations of the source function we assumed the laser power to be 6.5W so that the tip temperature at the end of the pulse matched the value of 250K assumed by Perea et al.[48] for the wire with uniform diameter. The axial temperature distribution for the wire with $r_0 = 15$ nm has the Gaussian profile assumed by Perea et al., but that is not the case for the tapered wires as shown in Fig. 3.4. Consequently, the initial condition of a Gaussian temperature distribution used in their computations for the tapered wires is not optimal. Furthermore, if the same laser power is used for uniform and tapered wires, the tip temperature at the end of the laser pulse varies with the taper angle.

The tip temperature calculated for uniform diameter and tapered silicon wires during the heating and cooling periods are presented in Fig. 3.4. For the tapered wires the tip temperature falls to the base temperature of 70K within 100 ns, but that for the uniform diameter wire takes an order of magnitude longer to decay to the base temperature. In all cases, however, the base temperature is reached well before the next pulse occurs for a pulse frequency of 100 kHz (10 μs).

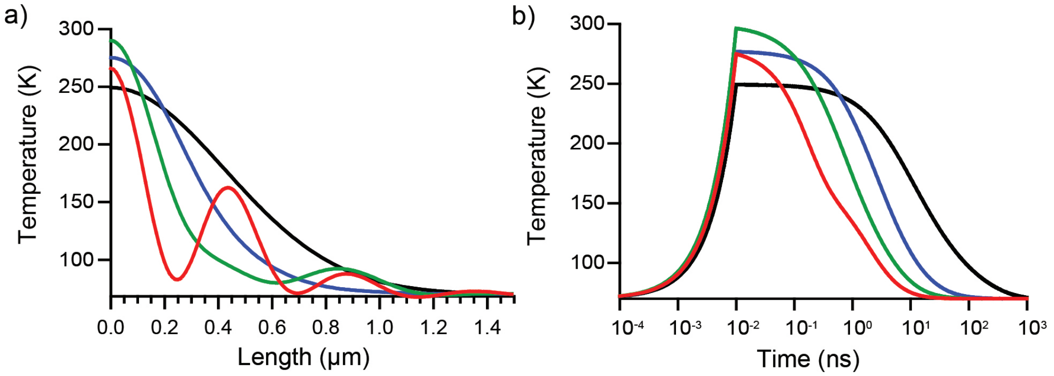

Figure 3.4: a) Results for the axial temperature distributions taken at the end of the 6.5W laser pulse for silicon nanowires with taper angles of $\theta = 0°$(black), 1°(blue), 2°(green), and 4°(red). b) Corresponding temperatures at the nanowire tip for the heating and cooling periods for the various wire shapes.

The results calculated of our analysis are compared with the numerical results of Perea et al.[48] for the identical system in Fig. 3.5. We predict larger rates of cooling even for the uniform diameter wire, which can be explained by how the appropriate choice of temperature-dependent thermal parameters affects the cooling time scale defined by Eq. (3.28). It is not clear what temperature-dependent thermal parameters were used in the numerical computations of Perea and his co-workers, but the faster cooling rates in our analysis suggest the choice of a thermal diffusivity was less than that of our simulations.

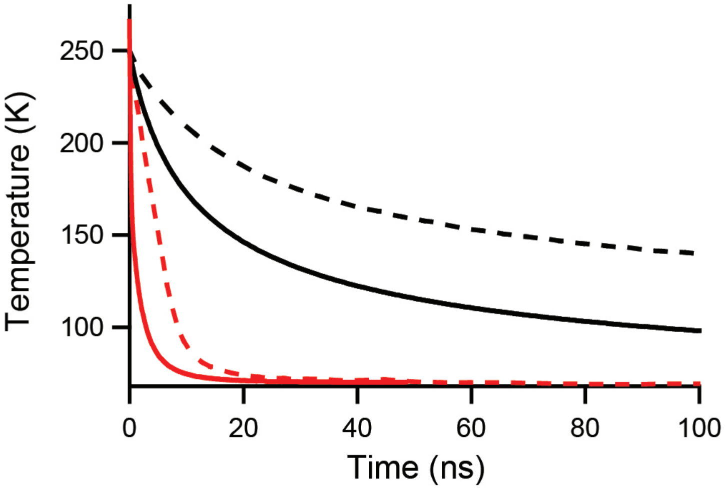

Figure 3.5: Comparison between our results (solid lines) and the results of Perea et al.[48](dashed lines) of the temperatures at the silicon nanowire tip for the cooling periods for taper angles of $\theta = 0°$(black) and 4°(red).

One cannot expect the temperatures for tapered wires from Perea et al. to agree with our results because of the effects of morphology-dependent resonances (MDRs) on the initial conditions used in the computations, but the decay times show similar trends. It is clear from Fig. 3.4 that the initial temperatures used for the cooling period are not Gaussian as assumed by Perea et al.

Amorphous silicon nanowires

We also simulated heating and cooling of amorphous silicon nanowires. There is much greater uncertainty about the thermal properties of amorphous silicon (a-Si and a-Si:H) than there is for crystalline silicon as indicated by the review by Cahill et al.[62] and the data of Zink et al.[63]. In the absence of data on nanowires of a-Si, and particularly on the size dependence, we have taken m = 0 and $\kappa = \kappa_0 = 1$ W/m·K in Eq. 3.24 for the heating and cooling calculations for amorphous nanowires. We used a complex refractive index of n = 4.4272 + 0.87758i[58] and heat capacity data reported by Zink et al.[63], using the mean value of α_0 as discussed above. In this case, the eigenfunctions $g_n(\xi)$ for the tapered wire become

$$g_n(\xi) = \frac{1}{\sqrt{\xi}}\left[J_{\frac{1}{2}}\left(\lambda_n\xi\right) + B_n J_{-\frac{1}{2}}\left(\lambda_n\xi\right)\right], \tag{3.47}$$

where

$$B_n = -\frac{J_{\frac{1}{2}}\left(\lambda_n\xi_1\right)}{J_{-\frac{1}{2}}\left(\lambda_n\xi_1\right)}. \tag{3.48}$$

Since $J_{1/2}(z) = (2/\pi z)^{1/2}\sin(z)$ and $J_{-1/2}(z) = (2/\pi z)^{1/2}\cos(z)$, the boundary condition at the wire tip can be written in terms of trigonometric functions to yield the following transcendental equation that the eigenvalues must satisfy

$$\begin{aligned} 0 &= \sin\left(\lambda_n\xi_0\right) + B_n\cos\left(\lambda_n\xi_0\right) \\ &\quad - \lambda_n\xi_0\left[\cos\left(\lambda_n\xi_0\right) - B_n\sin\left(\lambda_n\xi_0\right)\right]. \end{aligned} \tag{3.49}$$

Table 3.2 lists the first few eigenvalues and norms for nanowire tapers of 1°, 2°, and 4°.

The low thermal conductivity of amorphous silicon ($\kappa_0 \approx 1$ W/m·K) and large Q_{abs} (Fig. 3.6a) lead to much higher tip temperatures at the end of a pulse compared with geometrically similar crystalline nanowires. For example, for a 30 nm diameter nanowire with the length and base temperature considered above for a crystalline nanowire the laser power is only 0.23 W to reach a tip temperature of 250K at the end of a pulse compared with 6.5 W for a crystalline sample. The dimensionless source functions for uniform and tapered amorphous silicon nanowires show comparable trends to those discussed for the crystalline case and are

Table 3.2: A partial list of eigenvalues and norms used for amorphous silicon nanowire simulations presented in Sec. 3.3.4.

		n				
		1	**2**	**3**	**4**	**5**
$\boldsymbol{\theta=1^\circ}$	$\lambda_{\mathbf{n}}$	0.2490	0.5001	0.7544	1.0119	1.2721
	$\|\|\mathbf{g_n}\|\|$	4.0100	2.8154	2.2891	2.0020	1.8583
$\boldsymbol{\theta=2^\circ}$	$\lambda_{\mathbf{n}}$	0.1294	0.2590	0.3889	0.5192	0.6500
	$\|\|\mathbf{g_n}\|\|$	7.7252	5.4556	4.4466	3.8444	3.4365
$\boldsymbol{\theta=4^\circ}$	$\lambda_{\mathbf{n}}$	0.0660	0.1320	0.1980	0.2640	0.3301
	$\|\|\mathbf{g_n}\|\|$	15.1563	10.7152	8.7464	7.5718	6.7695

presented in Fig. 3.6, resulting in nanowire temperature distributions shown in Fig. 3.7a. The time required for the tip temperature to decay to the base temperature of 70K (Fig. 3.7b) in this case is more than an order of magnitude greater than for the crystalline material and is close to the start of the next laser pulse, designated by the arrow labeled f_p in Fig. 3.7b.

3.3.5 Comparison to experimental observation

To explore the effects of thermal properties on the evaporation of ions using laser-assisted atom probe tomography (LA-APT) we performed experiments on single tapered nanowires of crystalline and amorphous silicon. The CAMECA LEAP 4000XHR LA-APT system was used for these experiments. A TM polarized focused pulsed UV laser (355nm wavelength) with a spot size of 1-5 microns, a 100 (amorphous silicon) or 200 (crystalline silicon) kHz pulse repetition rate, and 20pJ (2W) laser pulse was used in addition to a standing DC voltage to result in field evaporation of the specimen. The analysis was conducted in ultra-high vacuum (UHV) system (1.4x10^{-11} Torr) with a cryogenically cooled specimen maintained at T_b = 44.2K, and the applied DC voltage was controlled to maintain a uniform evaporation rate of

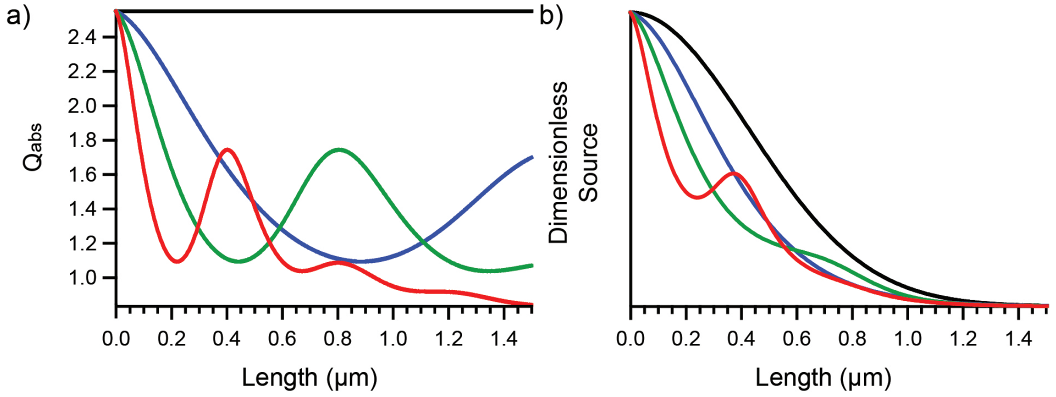

Figure 3.6: a) Absorption efficiency Q_{abs} of amorphous silicon nanowires with taper angles of $\theta = 0°$(black), 1°(blue), 2°(green), and 4°(red) in vacuum irradiated with a 532nm wavelength TM-polarized laser at 7° incidence. b) Corresponding dimensionless source functions (Eq. 3.30, normalized to the wire tip value) showing Q_{abs} resonances superposed with the irradiance of the Gaussian beam.

0.005 atoms/pulse throughout the length of the experiment.

For the silicon nanowires the tip radius r_0 was measured to be 12nm, and the shank angles were θ=9.6° for the crystalline sample and θ=12.2° for the amorphous silicon nanowire. For the heat transfer calculations the pulse width was taken to be 1 ps, and the lengths to be 10 μm. The Gaussian beam was considered to have a spot size of 1 μm at FWHM, resulting in a beam waist of $w_0 = 0.849$ μm. The absorption efficiency Q_{abs} was calculated using the 355 nm wavelength at an incidence angle of 7° with complex refractive indices for the silicon and amorphous silicon nanowires given by $n = 5.657 + 3.0186i$ and $n = 3.7414 + 2.7813i$[58], respectively.

Ion mass-to-charge state spectra (for $^{28}Si^{2+}$ - $^{30}Si^{2+}$) and calculated tip temperatures for the crystalline and amorphous samples are shown in Fig. 3.8. As the ion mass-to-charge spectra is generated by a time-of-flight detection technique, the mass-to-charge counts generated by the detector depends on time elapsed between the laser pulse and the detection

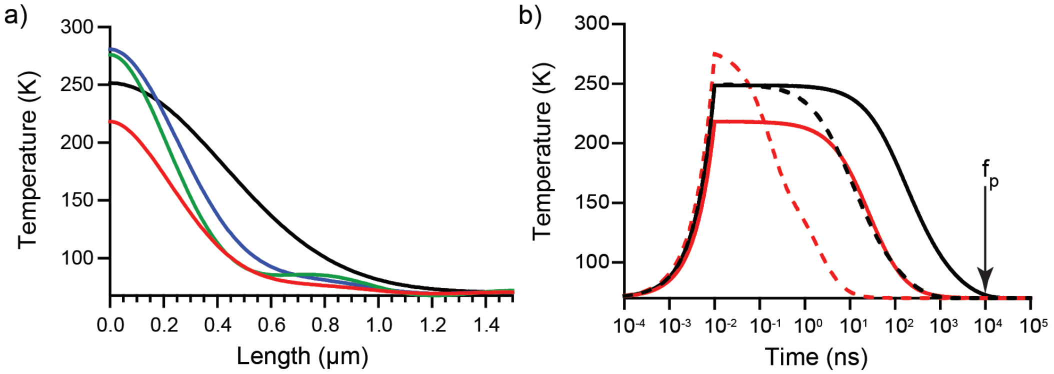

Figure 3.7: a) Results for the axial temperature distributions taken at the end of the 0.23W laser pulse for amorphous silicon nanowires with taper angles of $\theta = 0°$(black), 1°(blue), 2°(green), and 4°(red). b) Corresponding temperatures at the nanowire tip for the heating and cooling periods for $\theta = 0°$ and 4° taper angles. For comparison, results for the corresponding taper angles of silicon nanowires (dashed lines) show cooling rates orders of magnitudes larger than amorphous silicon nanowires, which approach cooling times of the pulse frequency interval f_p.

event[48]. Therefore, the longer the nanowire persists above a critical ion emission temperature after the initial laser pulse, the more spread in the ion mass-to-charge spectra is to be expected. As shown in Fig. 3.8, the increased spread in the ion mass-to-charge state spectrum of the amorphous silicon nanowire can be explained by a slower cooling rate and thereby prolonged time at higher temperatures.

3.3.6 Discussion of Results

The use of Eq. 3.24 for the dependence of the thermal conductivity on size appears to be adequate for the data of Li et al. [55] for crystalline silicon nanowires with radii greater than 25 nm, but it is not accurate for the smallest wires studied. It overpredicts κ for $r < 25$ nm. Furthermore, we note in Sec. 3.3.4 that there is uncertainty about the thermal properties of

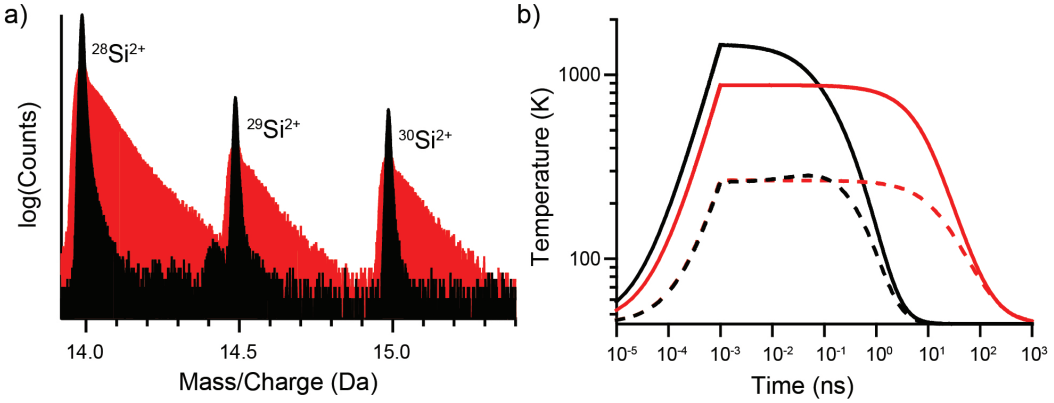

Figure 3.8: a) Time-of-flight mass-to-charge state spectrum of the $^{28}Si^{2+}$ - $^{30}Si^{2+}$ ions from the silicon nanowire (black) and amorphous silicon nanowire (red). b) Corresponding predicted temperatures at the nanowire tip of the heating and cooling periods for the experimental TM polarization (solid lines) and example TE polarization (dashed lines), showing the strong peak temperature dependence on polarization. The increased width of the amorphous silicon nanowire's Si^{2+} peaks are attributed to the decreased cooling rate of the nanowire.

amorphous silicon reported by Cahill et al.[62] and the data of Zink et al.[63]. The results of these investigators are for thin films of amorphous silicon deposited on substrates such as MgO or Si[62]. There is considerable scatter in the thermal conductivity data of various investigators for film thicknesses ranging from 0.33 μm to 50 μm near room temperature. Earlier data of Cahill et al.[64] show a plateau in the thermal conductivity versus temperature for $T > 50$ K with $\kappa \cong 1.8$ W/m·K whereas the temperature-dependent thermal conductivity reported by Pompe and Hegenbarth[65] show κ varying from about 0.4 to 1.8 W/m·K in the temperature range 10 K to 120 K. The thin film κ data for amorphous silicon presented in Figs. 5 and 6 of Cahill et al.[62] and Fig. 1 of Zink et al.[63] fall in the range 0.5 to 2 W/m·K. In this case, it is a reasonable assumption that the thermal conductivity has a relatively weak dependence on the radius.

Another important consideration for our analysis is the treatment of thermal parameters as independent of temperature. As noted in Sec. 3.3.2, the thermal diffusivity is a temperature dependent parameter as both κ and C_p typically have strong temperature dependencies. However, obtaining an analytical solution to Eq. 3.12 necessitates that the thermal parameters be independent of temperature. To account for this, the analysis for the temperature evolution of the laser pulsed system is iterated so that the constant temperature thermal properties are updated to better approximate the mean nanowire temperature at the end of the laser pulse in the irradiated region. This technique helps to mitigate the assumption of constant temperature thermal parameters, but the approximation becomes less appropriate as large thermal gradients are generated in the irradiated region.

The peak temperature of tapered wires is affected by MDRs as well as the polarization of the pulsed laser since Q_{abs} depends on the polarization. Figure 3.8b illustrates the sensitivity of the incident polarization on the resulting tip temperature of the specimen. Figure 3.9 shows the sensitivity of Q_{abs} to the polarization, and it varies by multiple orders of magnitude over the length of a wire. Therefore, the choice of the laser polarization plays a key role in modulating the specimen temperature during experiments.

3.3.7 Conclusion

An analytical model of pulsed laser heating of uniform and tapered supported nanowires has been presented, which takes into account size-dependent thermal parameters. The interplay between the specimen size, taper angle, thermal properties, and laser wavelength and polarization has been investigated by taking silicon nanowires as a representative example. We observe that the taper angle, the size-dependence of the thermal conductivity, and the choice of temperature that constant thermal parameters are evaluated at become increasingly important when determining the rate of heat generation and dissipation. Furthermore, we find that internal temperature distributions and peak specimen temperatures are highly sensitive to the incident laser polarization and subsequent MDRs. By comparing our simulation results with experimental data, we see that these effects on peak temperatures and cooling rates correspond to broadening in the produced ion mass spectra. The results can

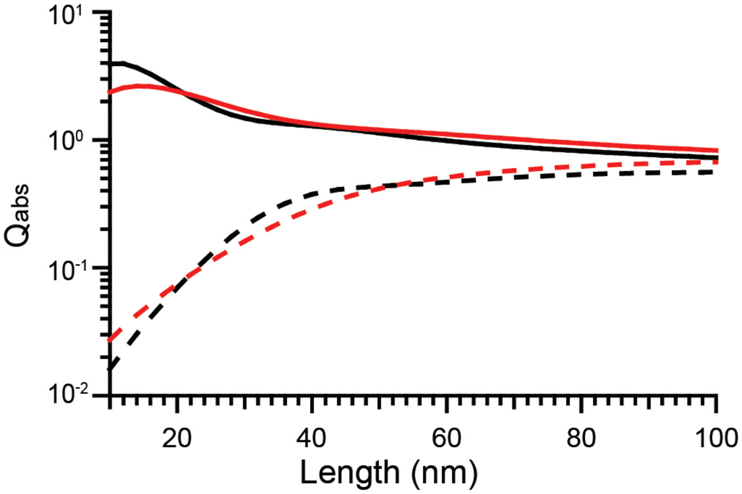

Figure 3.9: Absorption efficiency Q_{abs} diameter dependence of a silicon nanowire (black) and amorphous silicon nanowire (red) irradiated with a 355nm wavelength 7° from normal with TM (solid lines) and TE (dashed lines) polarizations.

thereby be used to predict the critical time it takes an pulsed specimen to cool to its base temperature prior to the next pulse, thereby informing ideal APT experimental parameters so that minimal fields for ion evaporation and maximum pulse rates can be attained.

Concerning alternative applications, another interesting extension would be to comment on experimental parameters needed to induce phase changes in laser pulsed nanowires[66]. Likewise, this analysis could be used to comment on heat generation and thermal effects of tip-enhanced spectroscopy for techniques such as nanoFTIR[67] and tip-enhanced raman spectroscopy (TERS)[68].

3.4 Laser heating of infinite nanowires

In the following section, closed-form analytical calculations are presented for the temperature rise within infinite circular cylinders with nanometer-scale diameters that are irradiated at right angles by a continuous-wave laser source polarized along the nanowires axis (TM-polarized). This framework is a closer approximation for laser heating of nanowires in an optical trap than the last section, but it is still does not perfectly mimic the experimental setup. However, this framework allows us to comment on laser-heated nanowires in a solvated environment, and we will see that the model gives an upper bound to nanowire temperatures that we would expect to observe during trapping experiments.

Solutions for the heat source are compared with numerical finite-difference time domain (FDTD) and with well-known Mie scattering cross sections for infinite cylinders. As was discussed in Sec. 3.3, the analysis also predicts that the maximum temperature increase is affected not only by the cylinder's composition, but also by MDRs that lead to significant spikes in the local temperature at particular diameters. Furthermore, silicon nanowires are observed to exhibit extremely uniform internal temperatures during electromagnetic heating to one part in 10^6, including cases where there are substantial fluctuations of the internal electric field source that generates the Joule-heating. For a highly absorbing material such as carbon, much higher temperatures are predicted, the internal temperature distribution is non-uniform, and MDRs are not encountered.

3.4.1 Initial setup and assumptions

If a long cylinder is suddenly exposed to an incident laser source, the temperature distribution in the cylinder is described by the energy equation Eq. 3.9, where the ∇^2 is the Laplacian in cylindrical coordinates. However, for a long (infinite) cylinder, heat transport in the z-direction is negligible and we get

$$\rho C_p \frac{\partial T}{\partial t} = \kappa \left[\frac{1}{r} \frac{\partial}{\partial r} \left(r \frac{\partial T}{\partial r} \right) + \frac{1}{r^2} \frac{\partial^2 T}{\partial \theta^2} \right] + S(r, \theta, t). \tag{3.50}$$

Although the heat source is a function of time, we shall consider it to be a function of only the spatial coordinates as we will focus on steady-state solutions where the source is constant in time. The coordinates of the system are shown in Fig. 3.10.

The boundary conditions for this system are given by the initial conditions

$$T(r, \theta, 0) = T_b, T(0, \theta, t) = \mathit{bounded}, \tag{3.51}$$

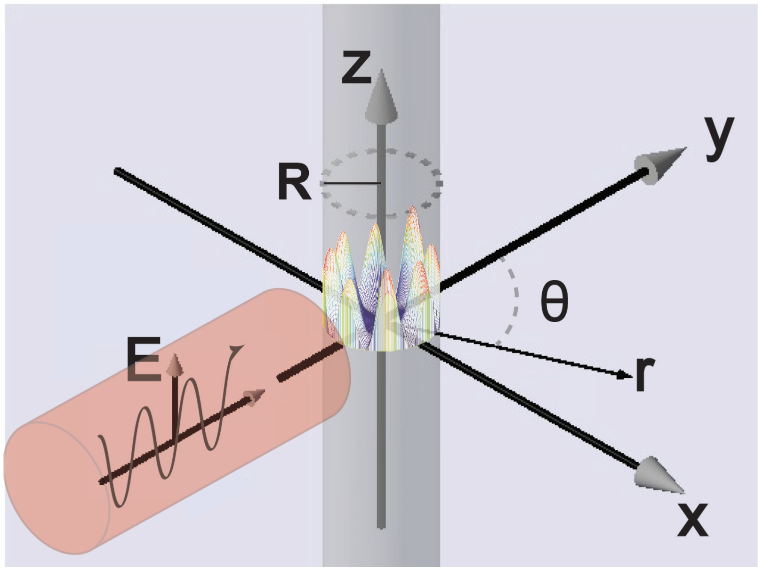

Figure 3.10: Schematic of the heat transfer framework for the infinite nanowire with a internal heating source from a TM-polarized continuous-wave laser.

a symmetry condition

$$\frac{\partial T}{\partial \theta}(r, 0, t) = 0, \tag{3.52}$$

and a convective heat transfer boundary condition at the surface

$$-\kappa \frac{\partial T}{\partial r}(R, \theta, t) = h[T(R, \theta, t) - T_b], \tag{3.53}$$

in which R is the cylinder radius, T_b is the temperature of the solvent far away from the cylinder, and h is a heat transfer coefficient that depends on the convective transport of heat to the surrounding solvent. Theory and empirical correlations for the heat transfer coefficient are usually written in terms of the Nusselt number which is defined by

$$\mathrm{Nu} = \frac{2Rh}{\kappa_s}, \tag{3.54}$$

where κ_s is the thermal conductivity of the surrounding solvent.

A representative correlation for the Nusselt number for free convection to and from horizontal cylinders is that of Churchill and Chu[69]. In the limit of no fluid flow over the surface, the result of the Nusselt number averaged over the surface of the cylinder is Nu = 0.36. McAdams[70] correlated a large amount of data for heating and cooling for air normal to cylinders. Their correlation for low Reynolds numbers is

$$\mathrm{Nu} = 0.32 + 0.43\mathrm{Re}^{0.52}, \tag{3.55}$$

where the Reynolds number is defined by

$$\mathrm{Re} = \frac{2R\rho v_\infty}{\mu_f}, \tag{3.56}$$

in which ρ is the density of the fluid, μ_f is its viscosity, and v_∞ is the fluids velocity. An alternate approximation is obtained by extrapolating data for low Reynolds number flow around the cylinder presented by Davies and Fisher[71]. This approach yields Nu = 0.30. For our analysis, we shall use the McAdams correlation, Eq. 3.55.

To make the energy equation Eq. 3.90 dimensionless, we introduce the non-dimensional variables given by

$$\Theta = \frac{(T - T_b)}{T_b}, \tag{3.57}$$

$$x = \frac{r}{R}, \tag{3.58}$$

$$\tau = \frac{\alpha t}{R^2}, \tag{3.59}$$

$$S^*(x,\theta) = \frac{R^2}{\kappa T_b} S(r,\theta), \tag{3.60}$$

where α is the thermal diffusivity of the cylinder.

Using these non-dimensional variables, the Eq. 3.90 transforms to

$$\frac{\partial\Theta}{\partial\tau} = \left[\frac{1}{x}\frac{\partial}{\partial x}\left(x\frac{\partial\Theta}{\partial x}\right) + \frac{1}{x^2}\frac{\partial^2\Theta}{\partial\theta^2}\right] + S^*(x,\theta). \tag{3.61}$$

The auxiliary conditions become

$$\Theta(x,\theta,0) = \frac{\partial\Theta}{\partial\theta}(x,0,\tau) = 0, \tag{3.62}$$

$$\Theta(0,\theta,\tau) = \mathit{bounded}, \tag{3.63}$$

$$\frac{\partial\Theta}{\partial x}(1,\theta,\tau) = -\mathrm{Bi}\Theta(1,\theta,\tau), \tag{3.64}$$

where Bi is the Biot number, which is related to the Nusselt number by

$$\mathrm{Bi} = \frac{\kappa_s}{\kappa}\frac{\mathrm{Nu}}{2}. \tag{3.65}$$

The Biot number is a measure of the ratio of the internal resistance to heat transfer to the external heat transfer resistance[72]. For Bi $\ll 1$, it can be anticipated that the internal temperature distribution is uniform or nearly uniform.

As found in Sec. 3.3, the generated electromagnetic fields inside of the cylinder depend on the polarization state of the incident laser beam, the orientation of the beam with respect to the axis of the cylinder, as well as other parameters considered below. For applications in particulate matter in the atmosphere and in particle suspensions in aqueous systems, the particle orientation with respect to the light source is random. For experimental studies using optical traps or electrodynamic levitation to suspend single particles, a laser source can be aligned to be parallel or perpendicular to the axis of a small rod. In general, any orientation of the rod with respect to the light beam can be analyzed by the theory presented here, but we shall confine our attention to a single orientation. Two special cases, initially outlined by van de Hulst[73], were also presented by Kerker[74] and Bohren and Huffman[75]. In these cases, it is assumed that the direction of propagation of a plane wave is normal to the axis of the cylinder (the z-axis). For Case I the incident electric field is parallel to the yz-plane (TM-polarized), and for Case II the incident electric field is perpendicular to the yz-plane (TE-polarized). For this analysis, we shall consider incident light with TM-polarization, but the theory can be extended to other orientations by using the internal electric field equations presented by van der Hulst, Kerker, and Bohren and Huffman to determine the heat source function.

The solutions of the light scattering problem reviewed by van de Hulst, Kerker and Bohren and Huffman are analytical solutions of the governing Maxwell equations. An alternate approach for the determination of the internal electric fields is by using numerical methods such as the finite-difference time-domain (FDTD) method[76]. We have applied the classical approach of van de Hulst and Bohren and Huffman as well as the FDTD approach to compute the internal electric field needed to calculate the internal heat source. For FDTD simulations, we used a freely available software through the MIT Electromagnetic Equation Propagation (MEEP) package[77].

Ruppin[78] calculated the electromagnetic energy density in an irradiated cylinder, and Liu et al.[79] presented plots of the electric field intensity for micro-cylinders for various complex refractive indices suspended in an absorbing gaseous medium. The motivation for the latter paper was to explore the effects of the energy absorption on the photophoretic force exerted on the rod by the electromagnetic irradiation. However, they did not compute the temperature field, which could be uniform (and thereby no photophoretic force) even if the internal energy source is non-uniform.

The volumetric rate of heat generation in the cylinder is given by Allen et al.[80] as

$$S = \frac{1}{2}\sigma\left(\mathbf{E_1}\cdot\mathbf{E_1}^*\right), \tag{3.66}$$

where $\mathbf{E_1}$ is the internal electric field vector, $\mathbf{E_1^*}$ is its complex conjugate, and σ is the electrical conductivity at optical frequencies of the cylinder which is given by

$$\sigma = \frac{4\pi \text{Re}\{N\}\text{Im}\{N\}}{\lambda\mu c}, \tag{3.67}$$

in which $N = n + ik$ is the complex refractive index of the cylinder, n = Re{N}, k = Im{N}, λ is the wavelength of the incident laser, μ is the magnetic permeability, and c is the speed of light in vacuum.

For the TM-polarized laser, the incident, internal, and scattered electric fields are given by Bohren and Huffman[75] as follows

$$\mathbf{E_i} = E_0\sum_{n=-\infty}^{\infty}(-i)^n e^{in\theta}J_n(\rho_s)\mathbf{e_z}, \tag{3.68}$$

$$\mathbf{E_1} = E_0\sum_{n=-\infty}^{\infty}(-i)^n e^{in\theta}d_n J_n(\rho_1)\mathbf{e_z}, \tag{3.69}$$

$$\mathbf{E_s} = -E_0\sum_{n=-\infty}^{\infty}(-i)^n e^{in\theta}b_n H_n(\rho_1)\mathbf{e_z}, \tag{3.70}$$

$$\tag{3.71}$$

where $i = \sqrt{-1}$, $\mathbf{e_z}$ is the unit vector in the z direction, and ρ_1 and ρ_s are defined by

$$\rho_1 = \grave{k}_1 r = \frac{2\pi}{\lambda} N r, \tag{3.72}$$

$$\rho_s = \grave{k}_s r = \frac{2\pi}{\lambda} N_s r, \tag{3.73}$$

where $\grave{k}_1$ and $\grave{k}_2$ are wavenumbers in the cylinder and in the surrounding solvent, respectively, and N_s is the complex index of refraction of the surrounding solvent. The functions $J_n(r)$ and $H_n(r)$ are Bessel and Hankel functions of the first kind, respectively. The amplitude E_0 of the electric vector is related to the irradiance I_{inc} of the incident laser by

$$E_0^2 = \frac{2c\varepsilon}{N_s} I_{inc}. \tag{3.74}$$

Liu et al.[79] showed that the internal field intensities for a TE-polarized wave are qualitatively and, to some extent, quantitatively similar to those for a TM wave. Consequently, we limit our analysis to the TM-polarized wave.

The coefficients b_n and d_n are obtained by applying appropriate boundary conditions on the electric and magnetic vectors at $r = R$ as discussed by Bohren and Huffman[75]. The results are

$$b_n = \frac{[J_n(\rho_1)J_n'(\rho_s) - mJ_n'(\rho_1)J_n(\rho_s)]}{[J_n(\rho_1)H_n'(\rho_s) - mJ_n'(\rho_1)H_n(\rho_s)]} \tag{3.75}$$

and

$$d_n = \frac{1}{m}\frac{[J_n(\rho_s)H_n'(\rho_s) - J_n'(\rho_s)H_n(\rho_s)]}{[J_n(\rho_1)H_n'(\rho_s) - mJ_n'(\rho_1)H_n(\rho_s)]}, \tag{3.76}$$

where $\mathrm{m} = \mathrm{N}/\mathrm{N}_s$.

Computations show that $d_{-n} = d_n$. Using these results in Eq 3.69, the internal electric vector becomes

$$\begin{aligned} \mathbf{E_1} = E_0 \Bigg\{ & d_0 J_0(\rho_1) - 2\sum_{j=1}^{\infty}(-1)^{j-1} d_{2j} J_{2j}(\rho_1)\cos(2j\theta) \\ & - i2\sum_{k=1}^{\infty}(-1)^{k-1} d_{2k-1} J_{2k-1}(\rho_1)\cos\left[(2k-1)\theta\right] \Bigg\} \mathbf{e_z}. \end{aligned} \tag{3.77}$$

Finally, the source function $S(r,\theta)$ is obtained by using Eq. 3.77 and the complex conjugate of $\mathbf{E_1}$ in Eq. 3.66.

Assuming a separated-variables product solution of the form

$$\Theta(x,\theta,\tau) = U(x)V(\theta)W(\tau), \tag{3.78}$$

the solution becomes

$$\Theta(x,\theta,\tau) = \sum_{j=1}^{\infty}\sum_{k=0}^{\infty} A_{jk}(\tau) J_k\left(\lambda_{j,k}x\right)\cos\left(k\theta\right), \tag{3.79}$$

where

$$A_{jk}(\tau) = \frac{2}{\pi}\frac{\left[1-e^{-\lambda_{j,k}^2\tau}\right]}{\lambda_{j,k}^2\|N_{jk}\|^2}\int_0^{\pi}\int_0^1 x' J_k\left(\lambda_{j,k}x'\right)\cos\left(k\theta'\right)S^*(x',\theta')dx'd\theta' \tag{3.80}$$

in which the prime over the independent variables indicates a dummy variable of integration, and the norm squared $\|N_{jk}\|^2$ of the eigenfunctions $J_k\left(\lambda_{j,k}x\right)$ is defined by

$$\|N_{jk}\|^2 = \int_0^1 x'\left[J_k\left(\lambda_{j,k}x'\right)\right]^2 dx'. \tag{3.81}$$

The eigenvalues $\lambda_{j,k}$ satisfy the boundary condition

$$\left.\frac{d}{dx}J_k\left(\lambda_{j,k}x\right)\right|_{x=1} = -\mathrm{Bi}J_k\left(\lambda_{j,k}\right), \tag{3.82}$$

which follows from Eq. 3.64.

The steady state solution is obtained by taking the limit as $\tau\to\infty$. The result is

$$\Theta(x,\theta) = \frac{2}{\pi}\sum_{j=1}^{\infty}\sum_{k=0}^{\infty}\left[\int_0^{\pi}\int_0^1 x' J_k(\lambda_{j,k}x')\cos\left(k\theta'\right)S^*(x',\theta')dx'd\theta'\right]\frac{J_k\left(\lambda_{j,k}x\right)\cos\left(k\theta\right)}{\lambda_{j,k}^2\|N_{jk}\|^2}. \tag{3.83}$$

To put some physical numbers on this result, for a silicon nanowire in water, the time required to reach steady state is of order 1ns - 1μs.

3.4.2 Results

As we did in Sec. 3.3, we will use silicon as our choice for the nanowire material. Furthermore, as we eventually want to comment on the heating of nanowires in an optical trap, we choose to use parameters that are common to laser trapping experiments such as water for our surrounding solvent as well as a NIR wavelength for the incident laser source. One common laser wavelength for NIR laser trapping is $\lambda = 980$ nm and at this wavelength the complex refractive index of silicon is given by N = $3.6014 + 0.0005259i$[58]. Here, we use the analysis described above to perform calculations for infinite cylinders with diameters ranging from 10 to 1000 nm. Again, we use experimental thermal conductivities from Li et al.[55] for the silicon nanowire simulations. Again, although in laser tweezer experiments the laser beam axis is parallel to the cylinder axis, it is informative to consider the configuration given that absorption is expected to be maximized when the electric field vector of the incident radiation is parallel to the cylinder's axis.

To compare source functions for various systems and parameters it is convenient to plot the internal source function normalized to the incident electric field amplitude $\left(\mathbf{E_1} \cdot \mathbf{E_1}^*\right)/E_0^2$. Sample source functions calculated using the analytical solution (Eq. 3.83) and the numerical FDTD MEEP solution for a silicon nanowire with a diameter of 500 nm in water are presented in Fig. 3.11. The MEEP results are shown at a time that is sufficient for the system to reach its steady state, since the FDTD approach solves the unsteady state system of equations. There is mutually consistent agreement between the analytical and numerical approaches, and for all results presented below the analytical solution was used. Furthermore, all calculations presented here were performed with an incident irradiance of 1 kW/cm^2 unless specified otherwise.

Normalized source functions for silicon nanowires in water are shown in Figs. 3.12a-c for rod diameters of 10, 536, and 1000 nm, and the corresponding dimensionless temperature distributions are presented in Figs. 3.12d-f. As expected, the internal electric field exhibits much more complex structure as the diameter increases due to the intricate wave interference and re-enforcement within the nanowire. However, for the case of silicon nanowires, the resulting internal temperature is very nearly uniform on the order of one part in 10^6 for all of the diameters considered. For a silicon nanowire with a diameter of 10 nm in water, Eq. 3.83 yields a very nearly uniform temperature distribution with $\Theta(x, \theta) \sim 2.5 \times 10^{-8}$. This implies that the nanowire temperature is that of the surrounding fluid. A uniform temperature is to be expected in this case because the Biot number is 0.0292, which is $\ll 1$. When the

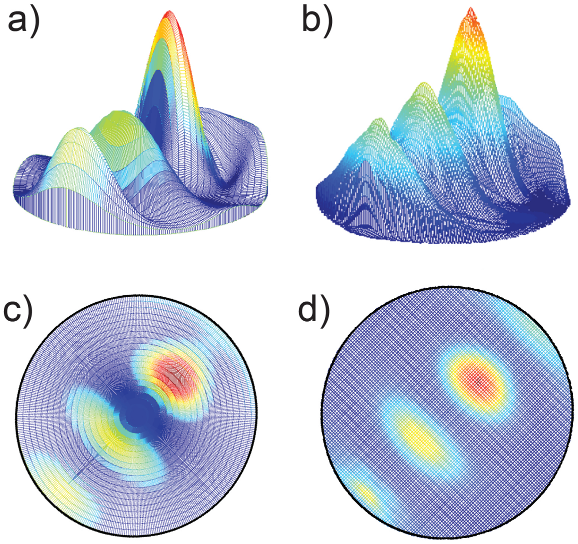

Figure 3.11: Comparison of the electric field distributions based on the closed-form analytical solution (a and c) and numerical FDTD MEEP simulation (b and d) for side views (a and b) and top-down views (c and d) for an infinitely long silicon cylinder with a diameter of 500 nm irradiated in water with a free-space wavelength of $\lambda = 980$ nm.

diameter is increased to 536 nm, Eq. 3.83 again yields a very nearly uniform temperature, as shown in Fig. 3.12e, with $\Theta(x,\theta) \sim 3.75\times10^{-4}$. Since Bi = 0.0012, a uniform temperature is again to be expected. That is also the case for a silicon nanowire diameter of 1000 nm. If the bulk thermal conductivity for silicon is used ($\kappa = 149$ W/m·K), Bi = 0.000658. Consequently, even though the heat source is highly non-uniform for this larger nanowire, the temperature distribution is very uniform with $\Theta(x,\theta) \sim 1.6\times10^{-4}$. The temperature increases as the size of the nanowire increases, but for the low Biot numbers associated with the silicon-water system the internal temperature is nearly completely uniform. Table 3.3 illustrates the uniformity of the internal temperature for silicon nanowires of various diameters in (a) air and (b) water. For both systems, the ratio (T_{max} - T_{min})/T_{avg} is very small. Consequently, even though the heat source may be highly asymmetric, these calculations lead to a counterintuitive prediction that heat conduction within the nanowire can lead to an extremely uniform internal temperature. The results for the intermediate size (536 nm) in Fig. 3.12b correspond to a MDR (whispering gallery mode) discussed further below.

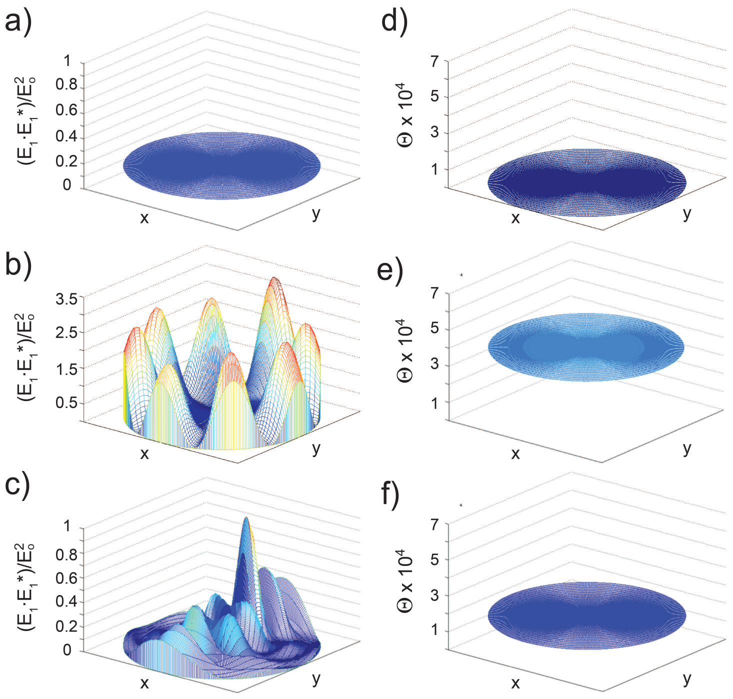

Figure 3.12: Plots of the calculated normalized cross-sectional electromagnetic heating source term $\left(\mathbf{E_1} \cdot \mathbf{E_1}^*\right)/E_0^2$ (a-c) and corresponding dimensionless cross-sectional temperatures $\Theta = (T - T_b)/T_b$ (d-f) for silicon nanowires in water with outer diameters of 10 nm (a and d), 536 nm (b and e), and 1 μm (c and f) irradiated at $I_{inc} = 1$ kW/cm^2 with a free-space wavelength of $\lambda = 980$ nm.

In contrast to silicon which is a weakly absorbing material due to its indirect bandgap, the calculated source functions are substantially different for strongly absorbing materials such as amorphous carbon. Pluchino et al.[81] measured the complex refractive index of

Table 3.3: Calculation of (T$_{max}$ - T$_{min}$)/T$_{avg}$ for various diameters of silicon in (a) air and (b) water.

(a)		(b)	
Diameter(nm)	$\frac{(T_{max}-T_{min})}{T_{avg}}$	**Diameter(nm)**	$\frac{(T_{max}-T_{min})}{T_{avg}}$
10	1.05E-09	10	1.38E-09
500	3.63E-08	500	5.69E-08
649.9*	2.40E-06	949*	2.02E-06
1000	1.79E-07	1000	2.00E-07

**- Denotes the diameter corresponding to a resonance condition leading to the highest calculated temperature.*

micrometer-sized spheres by levitating them in air using an electric field and illuminating them with a laser beam. They reported the refractive index of amorphous carbon spheres of radius ∼4 μm to be approximately given by N = 1.70+0.80i for a laser wavelength of 488 nm. The thermal conductivity of carbon at room temperature varies from 0.0159 W/m·K for amorphous carbon to 138 W/m·K for graphite, and 2,200 W/m·K for diamond.

Figure 3.13a shows the dimensionless source for an amorphous carbon rod with a diameter of 1 μm in water, and Fig. 3.13b shows the source for a carbon rod in air. The source functions are similar for the highly absorbing carbon rod with little penetration of the electromagnetic wave into the core of the rod. The lack of penetrating electromagnetic waves into the carbon rod prevents internal wave interference and thus there are no MDRs expected for the carbon case. The corresponding dimensionless temperature distributions are presented in Figs. 3.13c and 3.13d. In this case, the surrounding fluid was at 298 K, and λ = 488 nm. The temperature rise for the carbon rod in air is an order magnitude greater than in water. In contrast to silicon, a non-uniform temperature distribution within the rod is predicted for both cases of carbon, which could lead to photophoresis.

As is the case of spherical particles, it is well known that large internal electric fields

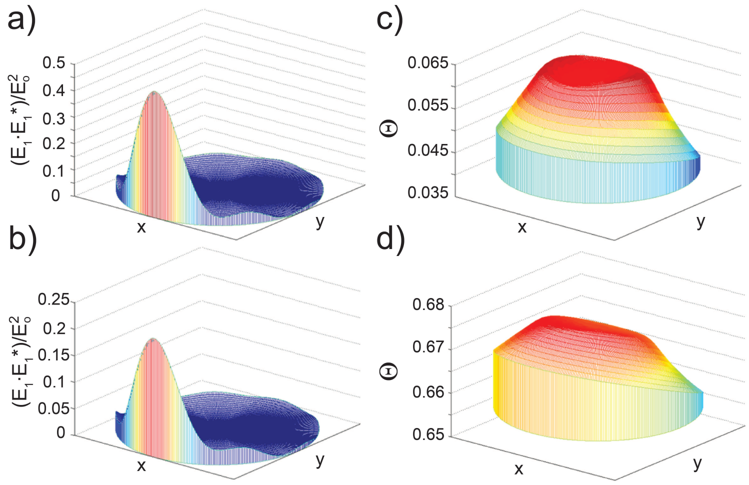

Figure 3.13: Plots of the calculated normalized cross-sectional electromagnetic heating source term $\left(\mathbf{E_1} \cdot \mathbf{E_1}^*\right)/E_0^2$ (a and b) and corresponding dimensionless cross-sectional temperatures Θ = (T - T$_b$)/T$_b$ (c and d) for carbon rods in water (a and c) and air (b and d) with an outer diameters of 1 μm irradiated at I$_{inc}$ = 1 kW/cm^2 with a free-space wavelength of λ = 488 nm. Unlike silicon, an appreciable variation in the dimensionless temperature is observed for the carbon material.

resulting from MDRs occur for particular nanowire diameters. Figure 3.14a shows how the dimensionless temperature normalized to the incident irradiance depends heavily on the nanowire's diameter. From Eq. 3.83, the definition of the source function (Eq. 3.66), and Eq. 3.74; the dimensionless temperature rise is proportional to the incident irradiance I$_{inc}$, assuming that the irradiance is in the regime of linear optics. For large I$_{inc}$, the temperature rise can be so large that the physical properties of the nanowire are not those at the surrounding temperature. Consequently, the computations of $\Theta(x, \theta)$ need to be modified when large temperature rises are predicted. Furthermore, for carbon rods in water, the rod temperature can be so high that boiling occurs and the Biot number becomes large.

As we did in Sec. 3.3, iterative calculations were performed for which an initial tempera-

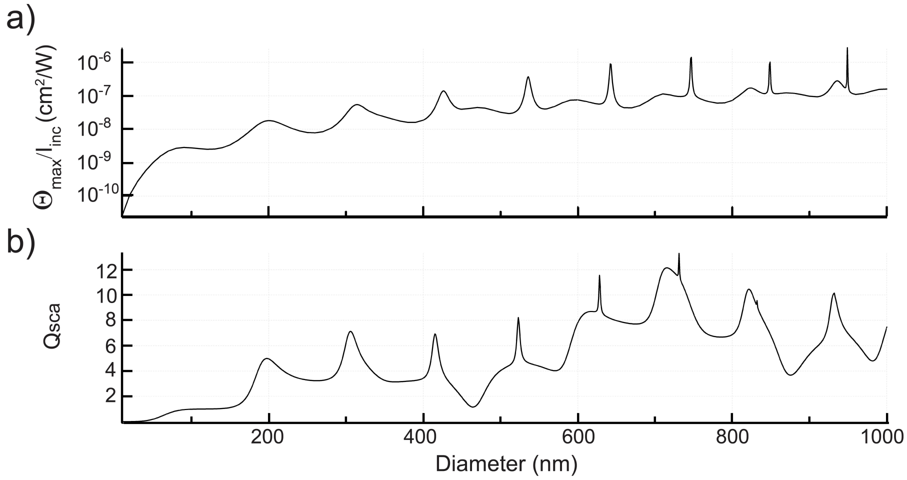

Figure 3.14: Comparison of calculated values for the maximum reduced temperatures of laser-heated silicon nanowires in water scaled by the incident irradiance with the calculated diameter-dependent scattering efficiency. a) Diameter-dependent maximum dimensionless temperature scaled by the incident irradiance of a crystalline silicon nanowire irradiated in water at a free-space wavelength of λ = 980 nm. b) Calculated scattering efficiency for a crystalline silicon nanowire in water irradiated at a free-space wavelength of λ = 980 nm as a function of nanowire diameter.

ture was calculated using thermal properties evaluated at T_b. Following each simulation, the thermal parameters were updated based on the predicted average temperature and a new simulation was performed until the newly calculated average temperature changed by less than 0.1°C. Table 3.4 presents the results of an example iterative simulation for pure silicon nanowires having diameters of 426 nm (a) and 420 nm (b) with an incident irradiance of 1 MW/cm^2. The former diameter corresponds to a MDR, which leads to a greater temperature rise than the off-resonance case. In both examples, the value of the maximum temperature within the nanowire was reached within three iterations. The thermal conductivities and refractive indices involved are also given in the table, and the temperature of the surrounding water (T_b) was assumed to be 298K.

Table 3.4: Temperature dependent convergence run (a) on resonance and (b) off resonance.

(a)

Dia (nm)	**$\varkappa_{eff}$ (W/m·K)**	**n_{eff}**	**k_{eff}**	**T_{max} (°C)**
426	60.5	3.6014	5.763E-04	67.3
426	49.0	3.6152	6.359E-04	66.6
426	49.2	3.6149	6.348E-04	66.6

(b)

Dia (nm)	**$\varkappa_{eff}$ (W/m·K)**	**n_{eff}**	**k_{eff}**	**T_{max} (°C)**
420	60.2	3.6014	5.763E-04	49.6
420	52.9	3.6094	6.102E-04	52.3
420	52.2	3.6103	6.140E-04	52.6
420	52.1	3.6104	6.145E-04	52.7

One clearly visible feature of these diameter-dependent calculations is the existence of temperature spikes due to MDRs of laser-irradiated cylinders in air and water when the nanowire diameter is larger than approximately 200 nm. Figure 3.14b presents calculated results for the scattering efficiency Q_{sca} and the maximum reduced temperature, Θ_{max}/I_{inc}, for silicon nanowires in water with diameters between 10 and 1000 nm. The scattering efficiency is given by[82]

$$Q_{sca} = \frac{\lambda}{\pi R} \sum_{n=-\infty}^{\infty} |b_n|^2. \tag{3.84}$$

It can be seen that the nanowires have several well-defined resonances at 427, 536, 642, 747, 849, and 949 nm, which appear in Q_{sca} as well as the temperature rise in Fig. 3.14. It is also interesting to note the absence of MDRs and a significant reduction in thermal heating observed for nanowires with diameters less than 100 nm. Simulations also show similar trends of temperature and scattering efficiencies for the silicon-air system. The calculated temperatures are higher in this case because of the lower thermal conductivity of the surrounding fluid. However, since the Biot numbers are smaller than for silicon-water, a more uniform temperature distribution within the cylinder is to be expected.

One area of interest for potential application of nanowires is in bioengineering, given that

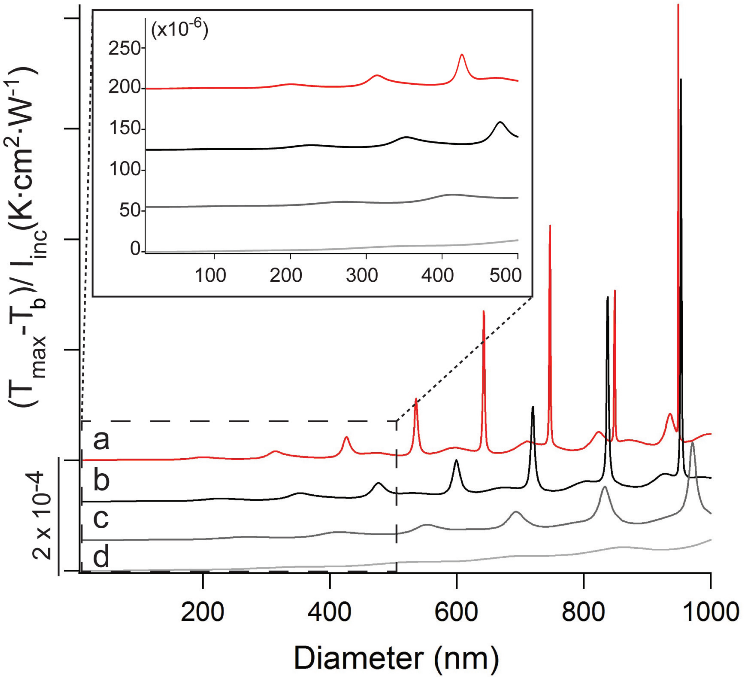

Figure 3.15: Diameter-dependent maximum temperature change, scaled by irradiance, of a porous crystalline silicon nanowire in water irradiated at a wavelength of λ = 980 nm with T$_b$ = 298K. (Inset) Expansion of the region between 10 and 500 nm. Plots a-d are offset and correspond to the (a) crystalline, (b) 25% porous, (c) 50% porous, and (d) 75% porous cases.

the nanowires are semiconducting and have high intrinsic surface areas[83]. In this case, the nanowire's thermal conductivity and the complex index of refraction depend on the porosity and pore structure. Therefore, these parameters can be modified by altering the porosity of the nanowire. We use this motivation to explore the effects of porosity on the heating of microporous silicon nanowires in water as shown in Fig. 3.15. Light scattering by voids within the porous silicon is an important consideration when calculating cavity resonances and is known to depend critically on the relative size between pores and the wavelength of incident radiation. Synchrotron-based grazing-incidence small angle x-ray scattering methods have been used to measure typical pore sizes below 5 nm for electrochemically etched porous silicon thin films[84] having porosities up to 45%. Based on this measurement of pore size, we use volume averaging theory (VAT)[85] to calculate the effective real and imaginary parts of the complex index of refraction given that the size parameter for the pores, defined by $\chi = \pi D/\lambda$, is much less than unity (<0.02). It should also be noted that this assumption is not appropriate for materials that have large pore sizes.

In the VAT approximation, the real and imaginary indices of refraction are given by

$$n_{eff} = \sqrt{\frac{1}{2}\left[A + \sqrt{A^2 + B^2}\right]}, \tag{3.85}$$

$$k_{eff} = \sqrt{\frac{1}{2}\left[-A + \sqrt{A^2 + B^2}\right]}, \tag{3.86}$$

where the coefficients A and B are defined by

$$A = \nu(n_s^2 - k_s^2) + (1 - \nu)(n^2 - k^2), \tag{3.87}$$

$$B = 2n_s k_s \nu + 2nk(1 - \nu), \tag{3.88}$$

where ν is the porosity of the composite.

Similarly, effective medium theory (EMT)[86] was used to calculate the effective thermal conductivity of a porous silicon-water composite system for various porosities (25, 50 and 75%) considering the sparsity of experimental data available for these materials. The effective thermal conductivity is given by

$$\begin{aligned}\kappa_{eff} = \frac{1}{4}\Big\{ & (3\nu - 1)\kappa_s + [3(1 - \nu) - 1]\kappa \\ & + \sqrt{(3\nu - 1)\kappa_s + \{[3(1 - \nu) - 1]\kappa\}^2 + 8\kappa\kappa_s}\Big\}. \end{aligned} \tag{3.89}$$

The most striking feature of these calculations is that extremely narrow MDRs continue to exist for nanowires with 25% porosity, indicating promising opportunities in the area of photothermal theranostic applications, such as drug loading. This is in stark contrast to the case of 75% porosity, in which the silicon nanowires no longer exhibit fine MDRs, likely due to the reduced reflectivity of an interface between water and a water/silicon composite that is 75% water. Also striking is the extremely low temperature rises predicted for nanowires with small diameters, irrespective of porosity as shown in the inset of Fig. 3.15. For example, even at extremely high irradiances, these calculations predict that the overall temperature rise in 10 nm diameter wires will be less than 1 °C for an indirect-gap material such as silicon.

3.5 Laser heating of finite nanowires

In this final theory section, we deal with optical heating of irradiated finite nanowires in the geometry that one would see in a laser tweezer setup. The derivation for this framework is very similar to the case of the infinite wire presented in Sec. 3.4. However, for the finite wire case, heat transport in the z-direction must be considered thereby necessitating additional boundary conditions. Furthermore, the laser source has also changed its propagation direction so that the laser is incident upon the end of the nanowire as it is during optical trapping experiments. This orientation complicates the analysis, however, since in this case there is no analytical relationship between the incident and internal fields. Therefore, numerical simulations are performed to determine the internal fields used for the heating source term in the analytical solution.

For the remainder of this section, we will derive the temperature solution for the framework described above. The model will then be applied to experimentally-trapped silicon nanowires to predict their temperature distribution during optical trapping. The temperatures that are predicted by the model will then be compared to experimentally-determined temperatures of the same silicon nanowires using techniques detailed in Sec. 2.5.1. Lastly, using both the model and experiments we will show how altering the silicon nanowires' optical and thermal properties via ion implantation can change the temperature of a trapped nanowire in a predictable manner.

3.5.1 Initial setup and assumptions

Again, the heating of a nanowire irradiated by a laser is described by the energy equation Eq. 3.9. Unlike the treatment in Sec. 3.4, here we must use the full Laplacian (∇^2) in cylindrical coordinates, which gives

$$\rho C_p \frac{\partial T}{\partial t} = \kappa \left[\frac{1}{r}\frac{\partial}{\partial r}\left(r \frac{\partial T}{\partial r} \right) + \frac{1}{r^2}\frac{\partial^2 T}{\partial \theta^2} + \frac{\partial^2 T}{\partial z^2} \right] + S(r, \theta, z, t). \tag{3.90}$$

The coordinates of the system are shown in Fig. 3.16.

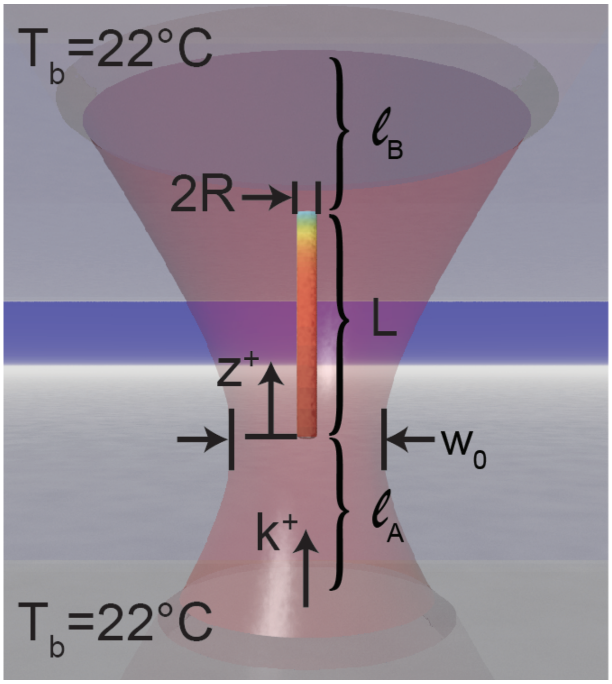

Figure 3.16: Schematic showing the heat transfer framework and example temperature distribution for a finite nanowire in a trapping chamber with a heating source from a continuous-wave laser incident on the end of the nanowire.

Figure 3.16 shows the laser incident with a focused beam and given k-vector as it is for optical trapping experiments. However, one can approximate the incident focused Gaussian beam (TEM$_{00}$ mode) of the optical trap as an unfocused planewave given that the nanowire's cross section ($\sim$ 200nm) is significantly smaller than the diameter of the diffraction-limited beam waist at the focus ($\sim$1μm). Furthermore, although the heat source is a function of time we shall consider it to be a function of only the spatial coordinates as we will focus on steady-state solutions where the source is constant in time. Also, if the internal electromagnetic field does not vary across the nanowire's diameter, the heat source reduces further to a function of axial position only, that is, S(z). We showed in Sec. 3.4 that homogeneous internal electromagnetic fields are a good approximation for silicon nanowires with diameters on the order of 10's of nanometers. For larger diameters, the internal fields may be radially varying, but using an approximation of radially and angularly homogeneous internal fields that are equal to the average of the realistic inhomogeneous case is appropriate considering that the large thermal conductivity and a small radial distance with respect to the silicon nanowire length dampens the radial dependence of the source term.

Under these assumptions, the dimensionless energy equation becomes:

$$\frac{\partial \Theta}{\partial \tau} = \frac{1}{\xi}\frac{\partial}{\partial \xi}\left(\xi \frac{\partial \Theta}{\partial \xi}\right) + \frac{1}{\xi^2}\frac{\partial^2 \Theta}{\partial \phi^2} + \left(\frac{R}{L}\right)^2 \frac{\partial^2 \Theta}{\partial \zeta^2} + S^*(\zeta), \tag{3.91}$$

where the dimensionless variables are defined by

$$\Theta = \frac{T - T_b}{T_b}, \quad \xi = \frac{r}{R}, \quad \zeta = \frac{z}{L}, \quad \tau = \frac{\kappa}{\rho C_p}\frac{t}{R} \tag{3.92}$$

Here, L is the nanowire length and R is the nanowire radius. The approximated dimensionless source function is given by

$$S^*(\zeta) = \frac{R^2}{\kappa T_b} S(\zeta). \tag{3.93}$$

Again, the source function S(ζ) for electromagnetic heating depends on the internal electromagnetic field, given by Eqs. 3.66, 3.67, and 3.74.

The boundary conditions for this framework (Fig. 3.16) show that the temperature of the upper and lower coverslips are assumed to be at the temperature of the fluid ($T_b = 22$ °C) as well as far from the nanowire in the radial direction. The length ℓ_A is the distance between the lower surface of the nanowire and the lower coverslip, while ℓ_B is the distance between the upper surface of the nanowire and the top coverslip of the chamber. As detailed in Sec. 3.4, theory and empirical correlations for the heat transfer coefficients are written in terms of the Nusselt and Biot numbers defined by Eqs. 3.55 and 3.65.

The dimensionless initial and boundary conditions for the nanowire are then given by

$$\Theta(\xi,\phi,\zeta,0) = 0 \tag{3.94}$$

$$\frac{\partial\Theta}{\partial\xi}(0,\phi,\zeta,\tau) = 0, \tag{3.95}$$

$$\frac{\partial\Theta}{\partial\zeta}(\xi,\phi,0,\tau) = Bi_1\Theta(\xi,\phi,0,\tau), \tag{3.96}$$

$$\frac{\partial\Theta}{\partial\xi}(1,\phi,\zeta,\tau) = -Bi_2\Theta(1,\phi,\zeta,\tau), \tag{3.97}$$

$$\frac{\partial\Theta}{\partial\zeta}(\xi,\phi,1,\tau) = -Bi_3\Theta(\xi,\phi,1,\tau), \tag{3.98}$$

$$\frac{\partial\Theta}{\partial\phi}(\xi,0,\zeta,\tau) = \frac{\partial\Theta}{\partial\phi}(\xi,\pi,\zeta,\tau) = 0, \tag{3.99}$$

where,

$$Bi_1 = \frac{\kappa_s}{\kappa}\frac{L}{\ell_A}, \tag{3.100}$$

$$Bi_2 = \frac{\kappa_s}{\kappa}\frac{Nu}{2} = 0.16\frac{\kappa_s}{\kappa}, \tag{3.101}$$

$$Bi_3 = \frac{\kappa_s}{\kappa}\frac{L}{\ell_B}. \tag{3.102}$$

To obtain the above boundary conditions, we assume that the heat loss from the lower and upper surfaces of the nanowire is due to conduction in the fluid between the nanowire and the bounding surfaces of the laser trapping chamber. This approximation neglects effects of motion of the fluid relative to the nanowire that might actually exist experimentally due to either Brownian motion or convective laminar flow in the event a substantial steady-state temperature gradient is established.

As in the previous sections, we use the classical method and assume a product solution to the homogeneous energy equation with the form

$$\Theta_H(\xi,\phi,\zeta,\tau) = u(\xi)v(\phi)w(\zeta)\chi(\tau), \tag{3.103}$$

where $u(\xi)$, $v(\phi)$, and $w(\zeta)$ are orthonormal eigenfunctions that satisfy the boundary conditions that are presented in Eqs. 3.94-3.99. Again, the function $\chi(\tau)$ does not need to be considered at this stage because the time-dependence of the inhomogeneous problem is substantially different than that of the homogenous problem.

The solution of the inhomogeneous energy equation can be written in terms of these orthonormal functions as

$$\Theta(\xi,\phi,\zeta,\tau)=\sum_{\ell=1}^{\infty}\sum_{m=1}^{\infty}\sum_{n=0}^{\infty}A_{\ell mn}(\tau)u_{\ell n}(\xi)v_n(\phi)w_m(\zeta), \tag{3.104}$$

where the eigenfunctions are given by

$$u_{\ell n}=\frac{X_{\ell n}(\xi)}{\|X_{\ell n}\|}=\frac{J_n(\gamma_{\ell n}\xi)}{\|X_{\ell n}\|}, \tag{3.105}$$

$$v_n=\frac{Y_n(\phi)}{\|Y_n\|}=\frac{\cos(n\phi)}{\|Y_n\|}, \tag{3.106}$$

$$w_m=\frac{Z_m(\zeta)}{\|Z_m\|}=\frac{cos(\delta_m\zeta)+(\mathrm{Bi}_1/\delta_m)\sin(\delta_m\zeta)}{\|Z_m\|}. \tag{3.107}$$

Here, $\mathrm{J_n}(\gamma_{\ell n}\xi)$ is the $\mathrm{n^{th}}$ order Bessel function, $\|X_{\ell n}\|$, $\|Y_n\|$, and $\|Z_m\|$ are the norms of the eigenfunctions, and $\gamma_{\ell n}$, n, and δ_m are their respective eigenvalues. Substituting Eq. 3.104 into Eq. 3.91 and applying the principle of orthogonality for each of the eigenfunctions, the time-dependent coefficients $\mathrm{A}_{\ell mn}(\tau)$ are found to be

$$\begin{aligned}A_{\ell mn}(\tau)=&\int_0^1\int_0^\pi\int_0^1\int_0^\tau S^*(\zeta')\\ &\exp\left[-\lambda_{\ell mn}^2(\tau-\tau')\right]\xi'u_{\ell n}(\xi')v_n(\phi')w_m(\zeta')d\xi'd\phi'd\zeta'd\tau',\end{aligned} \tag{3.108}$$

where the primes indicate dummy variables of integration, and

$$\lambda_{\ell mn}^2=\gamma_{\ell n}^2+\left(\frac{R}{L}\right)^2\delta_m^2. \tag{3.109}$$

Since we are worried about steady state heating solutions, the source function is not a function of time and Eq. 3.108 can be integrated over time to yield

$$A_{\ell mn}(\tau)=\frac{1-\exp\left[-\lambda_{\ell mn}^2\tau\right]}{\lambda_{\ell mn}^2}\int_0^1\int_0^\pi\int_0^1 S^*(\zeta')\xi'u_{\ell n}(\xi')v_n(\phi')w_m(\zeta')d\xi'd\phi'd\zeta'. \tag{3.110}$$

At steady state ($\tau\rightarrow\infty$) this result reduces to constants given by

$$A_{\ell mn}=\frac{1}{\lambda_{\ell mn}^2}\int_0^1\int_0^\pi\int_0^1 S^*(\zeta')\xi'u_{\ell n}(\xi')v_n(\phi')w_m(\zeta')d\xi'd\phi'd\zeta', \tag{3.111}$$

and the steady state dimensionless temperature distribution reduces to

$$\Theta(\xi,\phi,\zeta) = \sum_{\ell=1}^{\infty}\sum_{m=1}^{\infty}\sum_{n=0}^{\infty}\frac{u_{\ell n}(\xi)v_n(\phi)w_m(\zeta)}{\lambda_{\ell mn}^2} \int_0^1\int_0^{\pi}\int_0^1 S^*(\xi',\phi',\zeta')\xi' u_{\ell n}(\xi')v_n(\phi')w_m(\zeta')d\xi' d\phi' d\zeta'. \tag{3.112}$$

As stated above, for an unpolarized laser the electric field is very nearly uniform in the radial and angular directions. Consequently, the internal electric fields are only a function of the axial position. As the source function is independent of r and ϕ, Eq. 3.112 can be simplified by setting $\nu_n(\phi) = \nu_0(\phi) = 1$, and carrying out the integration over ξ to give

$$\Theta(\xi,\zeta) = \sum_{\ell=1}^{\infty}\sum_{m=1}^{\infty}\frac{X_{\ell 0}(\xi)Z_m(\zeta)J_1(\gamma_{\ell 0})}{\gamma_{\ell 0}\lambda_{\ell m0}^2\|X_{\ell 0}\|^2\|Z_m\|^2}\int_0^1 \langle S^*(\zeta')\rangle\, Z_m(\zeta')d\zeta' \tag{3.113}$$

where $\langle$S*(ζ')$\rangle$ is determined by the spatial average of the internal electric field at each axial position.

3.5.2 Theory results

Optical trapping experiments were performed on seven unique nanowires at various irradiances in order to experimentally determine the nanowires' temperatures using the methods outlined in Sec. 2.5.1. Details and results for this experiment will be given in Sec. 3.5.3. However, after the trapping experiments were performed, the nanowires' dimensions were measured using an atomic force microscope (AFM) in order to allow for accurate internal electric field simulations and temperature predictions with our model. For the more complex case of a finite cylindrical nanowire considered here, it is necessary to use numerical methods to determine the internal electromagnetic field profile within nanowires of various compositions. For the simulations shown here, freely-available discrete dipole approximation (DDA)[19, 87] electromagnetic simulation software was applied to compute the source-function for the case of an unpolarized planewave with a k-vector along the seven nanowires' axes. A DDA internal electric field solution for an example silicon nanowire (Fig. 3.17a) is

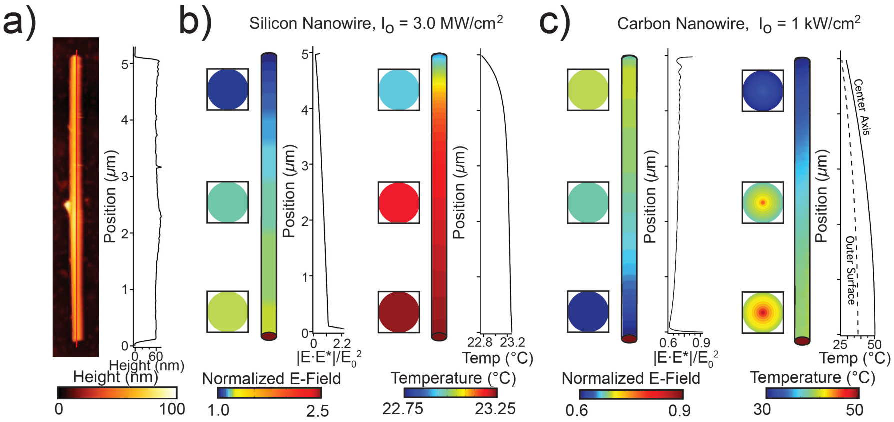

Figure 3.17: a) Atomic force microscope image of a silicon nanowire after optical trapping experiments. b) Calculated axial internal electric field magnitude and the corresponding axial temperature profile for the silicon nanowire shown in (a). c) Calculated axial internal electric field magnitude and the corresponding axial temperature profile for an amorphous carbon nanowire with the same nanowire geometry used in (a).

shown in the left-hand plot of Fig. 3.17b. The corresponding temperature profile given by Eq. 3.113 is shown in the right-hand plot of Fig. 3.17b.

Furthermore, it is also possible to use this model to make quantitative comparisons of the internal electromagnetic field and temperature profiles for strongly absorbing nanowires such as amorphous carbon[88, 89] with those for crystalline silicon nanowires. Example results are presented in Fig. 3.17c for an amorphous carbon nanowire that has an identical cylindrical morphology as the silicon nanowire in Fig. 3.17a,b. A visible wavelength of $\lambda = 488$ nm and irradiance of 1 kW/cm^2 are used for these calculations given the availability of experimental absorption coefficients for amorphous carbon in this spectral region[88]. The large imaginary index of refraction, k = 0.8, and low thermal conductivity $\kappa = 0.0159$ W/m·K of amorphous carbon lead to several marked differences between weakly absorbing silicon and strongly absorbing amorphous carbon nanowires.

First, the internal electric field profile is much more complex than that for crystalline silicon owing to the large imaginary index of refraction for amorphous carbon. There is also a sizeable field along the length of the nanowire leading to heating along the entire length of the nanowire. This would not be expected for planar amorphous carbon due to the large absorption coefficient at this wavelength. Second, there is an appreciable radial temperature gradient across the carbon nanowire that is not observed in the case of the silicon nanowire. Third, the total temperature gradient along the length of the nanowire (∼20°C degrees over 5 μm) is significantly larger than that for the silicon nanowire (∼1°C over 5 μm), even though the incident irradiance is over three orders of magnitude lower. This observation implies that photothermal heating and subsequent effects of photophoresis are much more relevant to consider for amorphous carbon or amorphous silicon materials than for crystalline silicon.

3.5.3 Silicon nanowire experiments

The analytical model derived above can now be used to predict temperatures of nanowires during laser trapping experiments. Here, we perform optical trapping experiments on silicon nanowires using a laser tweezer and apply the temperature extraction analysis described in Sec. 2.5.1 so that we can comment on the effectiveness of the model. A series of 7 native and 4 ion-implanted silicon nanowires were optically trapped and analyzed thermally with the laser tweezer at various irradiances (∼0.7 MW/cm^2, ∼1.8 MW/cm^2, and ∼3 MW/cm^2) at a distance of ∼75μm from the lower coverslip (half the chamber thickness). Each nanowire was then affixed to the top coverslip of the trapping chamber to facilitate AFM analysis as shown in Fig. 3.17a. The experimentally determined temperatures are then compared to the model's predicted temperatures and the results are discussed.

Experimental setup

Vertically aligned silicon nanowire arrays are fabricated using the metal-assisted chemical etching (MACE) method[90] (Fig. 3.18). Briefly, a polished <111> p-type (B) 10 Ω·cm silicon wafer is submerged in a 1:1 (v/v) solution of 10M hydrofluoric acid (HF) and 0.04M silver nitrate at room temperature and pressure for 3 hours. In this method, silver ions from the silver nitrate deposit on the surface of the silicon wafer. At the silver-silicon interface, a Schottky junction is created. Charge transfer across the junction permits chemistry that creates a silicon oxide layer at the interface that is continuously etched by HF to create an array of silicon nanowires, as shown in Fig. 3.18b.

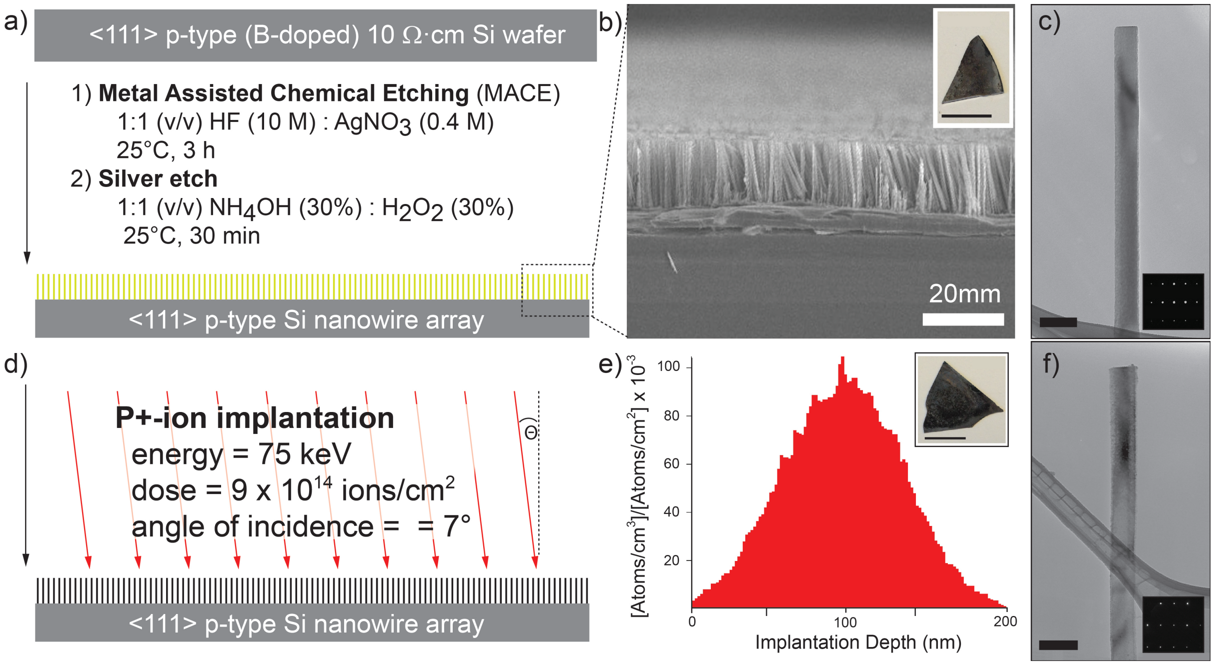

Figure 3.18: a) MACE diagram of a silicon nanowire array from a <111> p-type 10 Ω·cm wafer. b) SEM image of the silicon nanowire array following silver etching (inset: optical micrograph of wafer, scalebar = 1 cm). c) TEM image of a silicon nanowire following MACE (scalebar = 150 nm, inset: SAED). d) Schematic of phosphorus-ion implantation of a silicon nanowire array. e) Simulation of the stopping depth of phosphorus ions in silicon using an implantation energy of 75 keV. f) TEM image of a silicon nanowire following phosphorus implantation (scalebar = 225 nm, inset: SAED).

The etched silicon wafer is then transferred to a silver etch composed of a 1:1 (v/v) solution of 30% hydrogen peroxide and 30% ammonium hydroxide at room temperature and pressure for 30 minutes. The silver etch dissolves the silver film that results during the previous silicon etching step. The etched silicon wafer with vertically aligned nanowires is then rinsed liberally with deionized (DI) water and allowed to air dry. To detach the nanowires from the substrate for optical trapping experiments, the wafer is submerged in a solvent (typically DI water) and subsequently sonicated in an ultrasonic bath for 1 minute. A representative single-crystalline silicon nanowire is shown in Fig. 3.18c.

Following MACE synthesis of a silicon nanowire array, point defects were also introduced selectively within the nanowires via ion implantation (Fig. 3.18d,f) of positive phosphorous ions at an energy of 75 keV with a flux of $\sim 10^{15}$ ions/cm^2 at an incidence angle of 7° off normal to reduce the effect of ion tunneling. Calculations were made using Stopping Range of Ions in Matter (SRIM) software[91] in order to select for implantation depths of approximately 100 nm (Fig. 3.18e) in order to ensure that implanted ions remain within the nanowires and not travel into the substrate of the array. Transmission electron microscopy images (Fig. 3.18c,f) reveal that silicon nanowires are crystalline after implantation, although there is apparent crystallographic damage to the top and side surface of the nanowires following ion implantation in Fig. 3.18f.

Once synthesized, experimental trapping chambers were prepared by transferring several microliters of the silicon nanowire/water dispersion via pipette into a chamber consisting of a glass slide and glass coverslip. The edges of the glass slide and the glass coverslip were then sealed with a 150-μm-thick adhesive spacer. A series of 7 native and 4 ion-implanted silicon nanowires were optically trapped at the center of the chamber ($\sim$75 μm from the surface) at three irradiances ($\sim$0.7 MW/cm^2, $\sim$1.8 MW/cm^2, and $\sim$3 MW/cm^2) while voltage traces were recorded at the quadrant photodiode for 3 seconds at a sample rate of 100 kHz. The x and y quadrant photodiode voltage signals were normalized to the sum (z) voltage signal and temperatures were determined using methods discussed in Sec. 2.5.1. Trapping data was acquired using an unpolarized 975 nm pigtailed Fiber Bragg Grating (FBG) stabilized single mode laser diode source. Each nanowire was then affixed to the top coverslip of the trapping chamber to facilitate subsequent AFM analysis.

3.5.4 Results and discussion

Average extracted temperatures for the 7 native and 4 ion-implanted silicon nanowires are shown in Fig. 3.19a for increasing laser irradiances. Predicted temperature distribution calculations discussed in Sec. 3.5.2 were made for each of these nanowires, and the agreement between experiments and theory are plotted in Fig. 3.19b,c. The arrow in Fig. 3.19b represents measurements made for the nanowire shown in Fig. 3.17a at an irradiance of 3 MW/cm^2. The model developed here predicts steady state nanowire temperatures that increase nonlinearly with increasing nanowire radii (Fig. 3.19c). As shown in Fig. 3.19c, this model is observed to under-predict the observed experimental temperatures for nanowires with diameters below $\sim$100 nm, and over-predict temperatures for nanowires above this threshold.

For small silicon nanowire radii, it is likely that photothermal heating of the ambient water bath becomes increasingly important[24], even though it is neglected in the model presented here. For large silicon nanowire radii, it is likely that heating occurs according to the predicted nonlinear dependence that leads to an inhomogeneous, nonlinear temperature field around the nanowire. Motion of cooler fluid near the nanowire acts to reduce the observed temperature relative to what is predicted with the model developed above. The laser trapping experiment here can only detect the local fluid temperature through the Brownian motion of the optically trapped nanowire. In this way, the ambient fluid temperature can be expected to be lower than the internal temperature of an optically trapped nanowire. Analysis methods accounting for inhomogeneous temperature fields during experimental temperature extraction will be handled in the next chapter. Furthermore, the nanowires move within the laser trap relative to the fluid due to Brownian motion, and this will increase the effective heat transfer coefficient used here. These effects are not included in the heat transport model developed in this section. However, the observed temperature increases scatter closely about theoretical predictions, which reflects the utility of the model

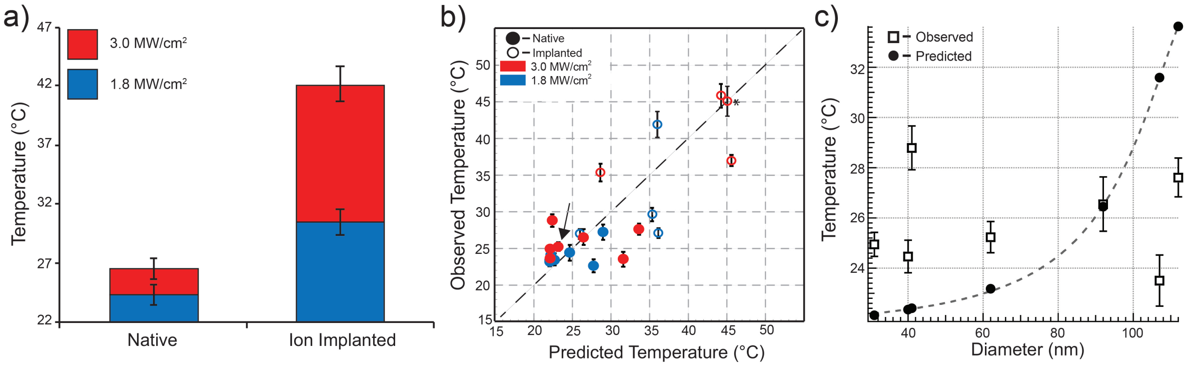

Figure 3.19: a) Average experimental temperatures measured from both native silicon nanowires (left) and ion-implanted silicon nanowires (right) at two separate laser irradiances. b) Comparison of experimentally-measured and numerically-calculated temperatures for several optically trapped native and ion-implanted silicon nanowires. The arrow represents calculations for a single nanowire presented in Fig. 3.17a. c) Diameter dependence of experimentally-measured and numerically-calculated temperatures for native silicon nanowires at 3 MW/cm^2 irradiance. The dashed line represents a 7th order polynomial fit. Error bars represent 95% confidence intervals.

developed here. For instance, the average internal electromagnetic fields from DDA simulations can be used to estimate the total power dissipated within an individual nanowire. The total heat dissipation was calculated to be 18 μW for the silicon nanowire of Fig. 3.17b under and irradiance of 3 MW/cm^2. The power associated with the incident beam over an equivalent cross-sectional diameter of the nanowire was found to be 81 μW, indicating that over 22% of the incident electromagnetic energy is dissipated as heat by the nanowire cavity.

Finally, it is possible to use the model to infer the unknown absorption coefficient for the ion-implanted silicon nanowires for comparison with bulk silicon. Temperature measurements showed significantly increased heating compared with native silicon nanowires. The imaginary component of the refractive index (k) for the implanted silicon nanowires was

Table 3.5: Experimental silicon nanowire trapping data.

Nanowire Type	**Observed (°C)**	**Predicted (°C)**	**ΔT (°C)**	**Diameter (nm)**	**Length (μm)**
Native	26.5	26.4	0.1	92	10.5
Native	24.9	22.1	2.8	31	4.5
Native	25.2	23.2	2.0	62	4.9
Native	28.8	22.4	6.4	41	8.2
Native	24.5	22.4	2.1	40	7.9
Native	27.6	33.6	-6.0	112	9.4
Native	23.5	31.6	-8.1	107	12.9
Implanted	45.8	44.2	1.6	97	16.2
Implanted	35.3	28.6	6.7	76	16.7
Implanted	37.0	45.6	-8.6	112	13.7
Implanted	45.9	45.9	0	37	13.9

varied using DDA computations and the resulting temperatures were calculated to match the observed temperature. For an ion-implanted silicon nanowire with 2R = 37 nm and L = 13.9 μm (denoted with an asterisk in Fig. 3.19b), we estimate k = 0.025, or equivalently, an absorption coefficient of $\alpha > 3{,}000$ cm^{-1}. This is roughly 2 orders of magnitude larger than for bulk intrinsic silicon (k = 5.6 x 10^{-4}, α = 72 cm^{-1})[58]. Using this extracted value for k, predicted temperatures for the other ion-implanted wires were calculated and are shown in Fig. 3.19b. Efforts towards introducing point defects in silicon nanowires leading to further increases of their absorption coefficient in the NIR tissue-transparency window will be further explored in chapter 5.

3.6 Discussion

In this chapter, we outlined the derivation of three related models for predicting temperatures distribution and evolution of laser-irradiated nanowires. From this treatment, we saw how the temperature dynamics hinge critically on the fundamental properties and parameters of the laser, the nanowire, and the surrounding medium. In Sec. 3.3, we showed how nanowire morphology (uniform versus tapered diameters) can affect the rate of heat generation and transfer due to the size dependence of thermal parameters such as the thermal conductivity and specific heat capacity. Furthermore, we also showed that polarization of the laser heating source can drastically impact the maximum temperature achieved due to the difference in the absorption efficiency of the nanowire at the relative orientations. In Sec. 3.4, we found how MDRs of the internal electric field heating source can drastically increase the temperature of weakly-absorbing nanowires. Moreover, the steady-state internal temperature distribution established within the nanowire is markedly dependent on the heat transfer both within the nanowire as well as between the nanowire and the surrounding matrix. Therefore, even though the internal electric field heating source can be highly asymmetric, the corresponding temperature distribution may still be highly uniform for systems with large thermal conductivities and heat transfer properties. Lastly, in Sec. 3.5, we showed how internal electric field heating sources can be solved using numerical techniques for complex systems such as that of the laser tweezer. The numerical heating source can then be used in the analytical model to predict temperature distributions and gradients of a trapped nanowire.

Preliminary optical trapping experiments of silicon nanowires show that the model for laser heating of a finite nanowire in Sec. 3.5 provides a powerful tool for approximating the temperature of a trapped nanowire. Additionally, modulation of the optical (e.g. absorption, complex index of refraction) and thermal (e.g. thermal conductivity) parameters of the nanowire through ion implantation shows an increase in photothermal temperatures of trapped silicon nanowires, which is also predicted by the model. With this understanding of the heating of the laser-nanoparticle system, we can attempt to intelligently engineer nanoparticles that will efficiently heat or cool by modifying the optical and thermal properties of the system.

3.7 Acknowledgments

We acknowledge our collaborator Prof. E. James Davis for his momentous contributions of the inception of the derivation, helpful discussion, and interpretation of each of the models presented in this chapter. We also acknowledge S. Manandhar, A. Devaraj, and D. E. Perea for experiments, helpful discussion, and interpretation of APT data and parameters; as well as B. E. Smith for help with laser trapping experiments, AFM analysis, and DDA simulations. We thank the University of Washington NanoTech User Facility (NTUF) as well as the Pacific Northwest National Laboratory Environmental Molecular Sciences Laboratory (PNNL EMSL) for use of instruments at their facility. This research is supported in part by the Air Force Office of Scientific Research Young Investigator Award (Contract #FA95501210400), the NSF Graduate Research Fellowship (DGE-1256082), and start-up funding from the University of Washington.

Chapter 4

EXTRACTING TEMPERATURES OF OPTICALLY TRAPPED NANOPARTICLES IN NON-ISOTHERMAL SYSTEMS

4.1 Introduction

In the last chapter, we covered the theory of photothermal heating of nanoparticles, particularly for nanowires in an optical trap. Laser tweezer experiments with silicon nanowires were discussed in Sec. 3.5.4 and the results showed some disagreement between predicted and observed temperatures. We reasoned that the disagreement is likely due to the fact that our temperature detection method described in Sec. 2.5.1 detects the local fluid temperature through the Brownian motion of the optically trapped nanowire under the assumption that the system is all at the same temperature. However, we can expect that the ambient fluid temperature far from the heated nanoparticle will different than the internal temperature of an optically trapped nanoparticle. The change in temperature between the heated nanoparticle and the surrounding medium would then lead to an inhomogeneous, nonlinear temperature field around the nanoparticle, rendering our experimental temperature techniques presented in Sec. 2.5 inaccurate.

In this chapter, we will attempt to rectify the temperature extraction methods presented in Sec. 2.5 by considering the inhomogeneous temperature fields around an optically trapped particle and determining how that affects its Brownian motion. We will start off by describing previously reported theory for how an inhomogeneous temperature fields affects a particle's Brownian motion, termed 'hot Brownian motion' or HBM. This approach will then be incorporated into the temperature extraction methods detailed in Sec. 2.5. Lastly, we will apply the updated techniques to optically trapped particles and discuss that difference between the HBM and classical Brownian motion treatment.

4.2 Accounting for non-isothermal systems by using hot Brownian motion analysis

For the temperature extraction methods described in Sec. 2.5, the temperature analysis of the trapped particle assumes that the particle-solvent system raises temperature in an isothermal manner, giving a thermal average of the hot particle and the cooler solvent surroundings. This assumption becomes unsuitable when measuring a trapped particle that heats drastically relative to its local solvent environment, giving rise to a large thermal gradient around the particle. Recently, HBM theory for the motion of a heated Brownian particle from the fluctuating hydrodynamics of its non-isothermal solvent has been developed[92–95]. The HBM theoretical model is beneficial in that it allows for an accurate determination of the particle temperature in the optical trap as well as the local thermal gradient that give rise to its Brownian dynamics.

Given that the temperature of the trapped particle is significantly different than the temperature sufficiently far from the laser focus, the dynamics of the particle-solvent system can be described by the HBM diffusion coefficient rather than the classical diffusion coefficient given by Eq. 1.11. For a spherical particle, the motion is then related to the effective HBM temperature by[93]

$$D_{HBM} = \frac{k_B T_{HBM}}{\gamma_{HBM}(T)}, \tag{4.1}$$

where $\mathrm{D_{HBM}}$ is the HBM diffusion coefficient, k_B is Boltzmann's constant, $\mathrm{T_{HBM}}$ is the HBM temperature, and $\gamma_{\mathrm{HBM}}(\mathrm{T})$ is the HBM Stokes drag. To the leading order of the temperature increment $\Delta\mathrm{T}=(\mathrm{T}_p\text{-}\mathrm{T}_b)$, where T_p is the temperature at the surface of the particle and T_b is the initial temperature of the solvent, the temperature-dependence of the viscosity on $\mathrm{T_{HBM}}$ can be neglected, giving an effective temperature[94]

$$T_{HBM} = T_b + \frac{5}{12}\Delta T. \tag{4.2}$$

It should be noted that the treatment of HBM to rod-like particles has been reported[95], where it was found that even for nanowires with extreme aspect ratios, the decay of the friction coefficients with the temperature increment of the nanowire was more or less the

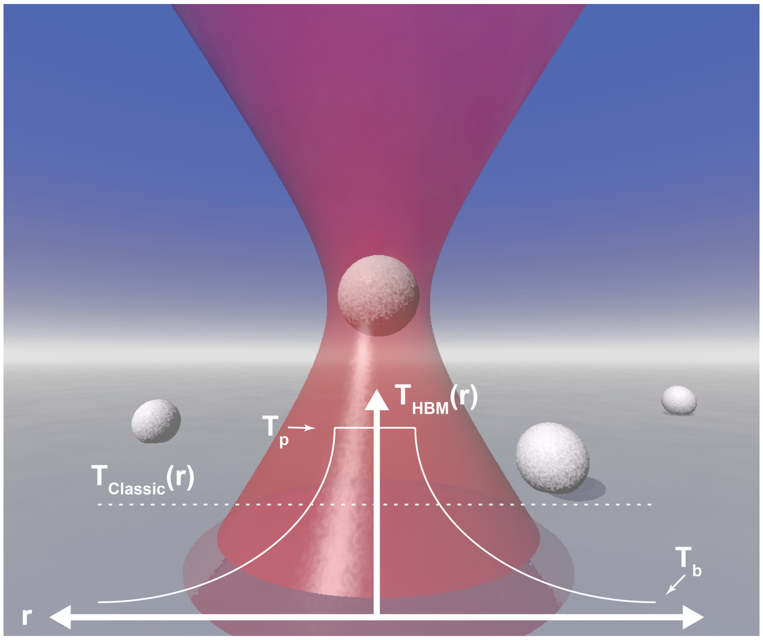

Figure 4.1: An illustration of an optically trapped particle in an aqueous fluid chamber. The local temperature profile between the particle temperature (T$_p$) and the bath temperature far away from the particle (T$_b$) is accounted for with hot Brownian motion analysis (solid line), which differs from the classical isothermal diffusion coefficient approach (dashed line).

same as for a sphere. Furthermore, as for the effective temperatures, the difference between that of rotational and translational motion transverse to the nanowire axis should be different (with the rotational motion being greater) but is most likely unmeasurably small for large aspect ratio nanowires. Therefore, we apply the same HBM analysis for spherical particles to nanowires with the appropriate change to the Stokes' drag term.

For a temperature dependence of the solvent viscosity given by Eq. 2.24, the HBM Stokes' drag is given by[93]

$$\gamma_{HBM}(T) = g\eta_{HBM}(T), \tag{4.3}$$

where g is the morphology-dependent coefficient, which for a nanowire moving transverse to the long axis is[96]

$$g = \frac{4\pi L}{\ln\left(\frac{L}{2R}\right) + 0.84}. \tag{4.4}$$

In Eq. 4.3, $\eta_{\mathrm{HBM}}(\mathrm{T})$ is the temperature-dependent HBM viscosity that is related to the viscosity of the solvent at room temperature, η_b, by[93]

$$\begin{aligned} \frac{\eta_b}{\eta_{HBM}(T)} \approx & 1 + \frac{193}{486}\left[\ln\frac{\eta_b}{\eta_\infty}\right]\left[\frac{\Delta T}{(T_b - T_{VF})}\right] \\ & - \left[\frac{56}{243}\ln\frac{\eta_b}{\eta_\infty} - \frac{12563}{118098}\ln^2\frac{\eta_b}{\eta_\infty}\right]\left[\frac{\Delta T}{(T_b - T_{VF})}\right]^2. \end{aligned} \tag{4.5}$$

By using Eqs. 4.2-4.5 for Eq. 4.1, $\mathrm{D}_{\mathrm{HBM}}$ represents a more accurate form of the experimental diffusion coefficient determined by power spectrum analysis outlined in Sec. 2.3. Therefore, we can equate the experimental diffusion coefficient to Eq. 4.1 to determine the temperature at the particle surface T_p (excluding the temperature discontinuity at the particle's surface from the Kapitza resistance[97]).

An alternative HBM temperature analysis using a semi-phenomenological expression for $\mathrm{D}_{\mathrm{HBM}}$ that approximately accounts for higher order terms in ΔT (Eq. 15 of the supporting online materials of Ref. [93]) yields consistent results, indicating that these higher order corrections are negligible, for our purposes.

4.2.1 Corrections to trapped particle surface temperatures

To comment on the application of HBM analysis to optical trapping experiments, silica microbeads were used for their monodisperse size distribution (1010 nm diameter) and their known capacity to heat minimally when trapped with a NIR laser trap[38]. For this experiment, a temperature controlled chamber was used with the chamber held at T_b = 25 °C while the bead was trapped and QPD photovoltages were acquired 10 consecutive times. QPD signals were calibrated using the method described in Sec. 2.4. The HBM analysis was then applied to the resulting calibrated PSD data and the temperature results are shown in red circles in Fig. 4.2. The average calculated particle temperature (red dashed line) is

$T_{p,HBM}$ = 35.9 °C with a standard deviation (red shaded area) of ±6.8 °C. For comparison, the same data was also analyzed using the temperature extraction methods detailed in Sec. 2.5 which assume isothermal conditions, and the temperature results are shown in blue squares in Fig. 4.2. The average calculated particle temperature (blue dashed line) is $T_{Classic}$ = 29.5 °C with a standard deviation (blue shaded area) of ±2.8 °C.

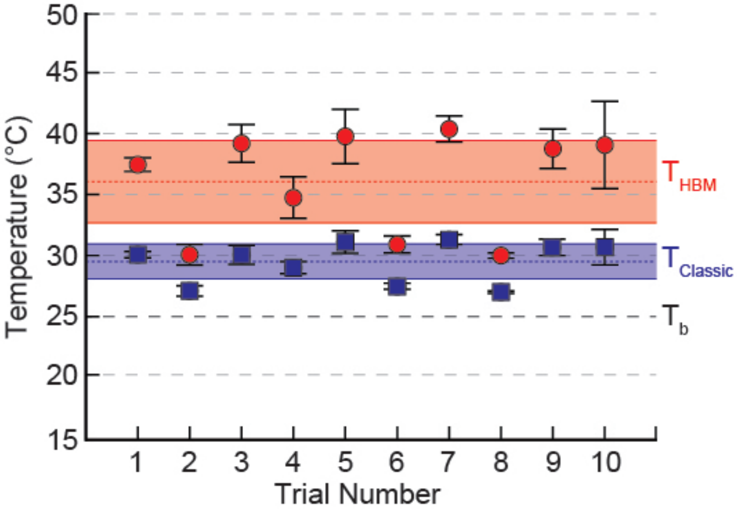

Figure 4.2: A 1.01 μm diameter silica microbead trapped in D_2O using a trapping wavelength of 975 nm in a temperature controlled chamber held at T_b = 25°C. QPD data was acquired 10 consecutive times at an irradiance of 5.9 MW/cm^2 and the temperature of the sphere was determined using both the HBM temperature analysis (red circles, T_{HBM}) and the temperature extraction method detailed in Sec. 2.5 (blue squares, $T_{Classic}$) which assumes isothermal conditions. The error bars represent the standard deviation.

4.3 Discussion

As evidenced by Fig. 4.2, the application of HBM analysis on determining the temperature of an optically trapped particle can have a significant impact for particles that heat above (or cool below) the ambient temperature. Furthermore, by applying HBM analysis to a trapped particle dispersed in a liquid phase, we can also approximate the local temperature gradient in the medium surrounding the trapped particle. The local temperature field at a distance r from the particles' surface is given by[93]

$$T(r) = T_b + \frac{R}{r}\left(T_p - T_b\right). \tag{4.6}$$

Knowing that the radius of the silica microbead is R = 505 nm, T_b = 25 °C, and $T_{p,avg}$ = 35.9 °C, the distance away from the particle where the temperature within 1 °C of T_b is 5.4 μm. The ability to measure and to control particle temperature and thermal gradients with HBM analysis could enable laser tweezers to investigate the triggering and probing of fundamental temperature-controlled biological processes[98].

To summarize, we have described an effective method to determine optically-trapped particle temperatures as well as the temperature gradient in the surrounding medium by combining laser tweezer calibration techniques, forward-scattered light power spectrum analysis, and HBM theory. Our experiments show the importance of accounting for inhomogeneous temperature fields when determining the temperature of an optically trapped particle. In the following chapters, we will utilize the HBM analysis in the temperature extraction techniques discussed in Sec. 2.5 to determine the temperatures of optically-trapped engineered nanoparticles that can superheat water and optically refrigerate.

4.4 Acknowledgments

We acknowledge Klaus Kroy of Leipzig University for insightful discussion of HBM analysis. This research is supported in part by the Air Force Office of Scientific Research Young Investigator Award (Contract #FA95501210400), the NSF Graduate Research Fellowship (DGE-1256082), and start-up funding from the University of Washington.

Chapter 5

PHOTOTHERMAL SUPERHEATING OF WATER WITH ION-IMPLANTED SILICON NANOWIRES

5.1 Introduction

Nanoparticle-mediated photothermal (PT) cancer therapy has received increased focus in the field of nanomedicine due to its potential as an effective, non-invasive, and targeted alternative to traditional cancer therapy based on small-molecule pharmaceuticals[34, 35, 99–102]. Gold nanoparticles have been a primary focus of PT research[103–107], which can be attributed to their size tunability[108–110], well understood conjugation chemistry[111–113], and efficient absorption of NIR radiation in the tissue transparency window (800 nm $-$ 1 μm) due to their size-dependent localized surface plasmon resonances[104, 114, 115].

Recently, semiconducting nanomaterials have gained traction as PT agents[116–121] owing to their synthetic simplicity and ability to tune their light-absorption properties independent of the nanoparticles' shape and size[102, 122]. Silicon nanowires (SiNWs) are one such semiconducting nanoparticle that has garnered interest as a PT agent[123]. Furthermore, silicon nanowires are well suited for PT applications since they are biodegradable[124, 125], generate singlet oxygen upon NIR photoexcitation[126], and can be made to be highly porous[127–129] for drug loading[130–133] and room-temperature photoluminescence[129, 134–136] applications.

A drawback of using silicon nanowires for PT therapy is that it is an inefficient absorber of light in the NIR due to its indirect bandgap. However, in Sec. 3.5.3 we showed how the PT heating efficiency of silicon nanowires can be increased by altering their thermal and optical properties via ion implantation. Yet, even with PT heating enhancement via ion implantation, the irradiance needed to heat silicon nanowires to temperatures suitable for PT cancer therapy (∼42 °C)[137, 138] is too large and would cause harmful damage to irradiated tissue. In this chapter, we apply our temperature extraction method from Sec. 2.5.2 with HBM analysis from Sec. 4.2 of trapped nanoparticles in a laser tweezer and show that we can drastically increase PT heating of ion-implanted silicon nanowires in a single-beam laser trap by using gold as the primary dopant ion to superheat water above 200 °C with ∼10 MW/cm^2 irradiances. Furthermore, we explore the role that the dopant ion plays in the PT heating process by comparing silicon nanowires implanted with gold ions to those implanted with silicon ions at several implantation doses for each ion. The HBM temperature extraction analysis is shown to be a versatile technique for quantifying heating of individual particles that arise during laser trapping experiments[38–41, 139–143]. The ion-implanted silicon nanowire heating results open up for the future possibility of using the gold-implanted silicon nanowires as a PT cancer agent at clinically relevant laser irradiances.

5.2 Ion-implantation and characterization of silicon nanowire arrays

Before ion implantation, silicon nanowire arrays were made using MACE method as described in Sec. 3.5.3. The resulting silicon nanowire arrays (Fig. 5.1b,c) were subsequently implanted with gold ions at an acceleration energy, incident beam angle, and ion doses that were determined using the simulation package SRIM[91] in order to result in ion penetration depths of ∼50 nm, which ensures gold ion distributions within the nanowires (Fig. 5.1e, inset) and not the underlying silicon substrate. For the gold ion implantation, ion doses of 6.25×10^{12}, 6.25×10^{13}, 6.25×10^{14}, and 6.25×10^{15} ions/cm^2 were used, resulting in dopant concentrations of 10^{18}, 10^{19}, 10^{20}, and 10^{21} ions/cm^3. As a control, separate silicon nanowire arrays were implanted with silicon ions at ion doses of 10^{14}, 10^{15}, and 10^{16} ions/cm^2, resulting in dopant concentrations of 2.5×10^{18}, 2.5×10^{19}, and 2.5×10^{20} ions/cm^3 with a penetration depth of 1.9 μm (Fig. 5.1d, inset). As shown in Fig. 5.1d and e, the effects of the implantation process can be seen visually as a darker surface, providing qualitative evidence for increased optical absorption. Following implantation, the silicon nanowires were detached from the substrate into DI water via ultrasonication.

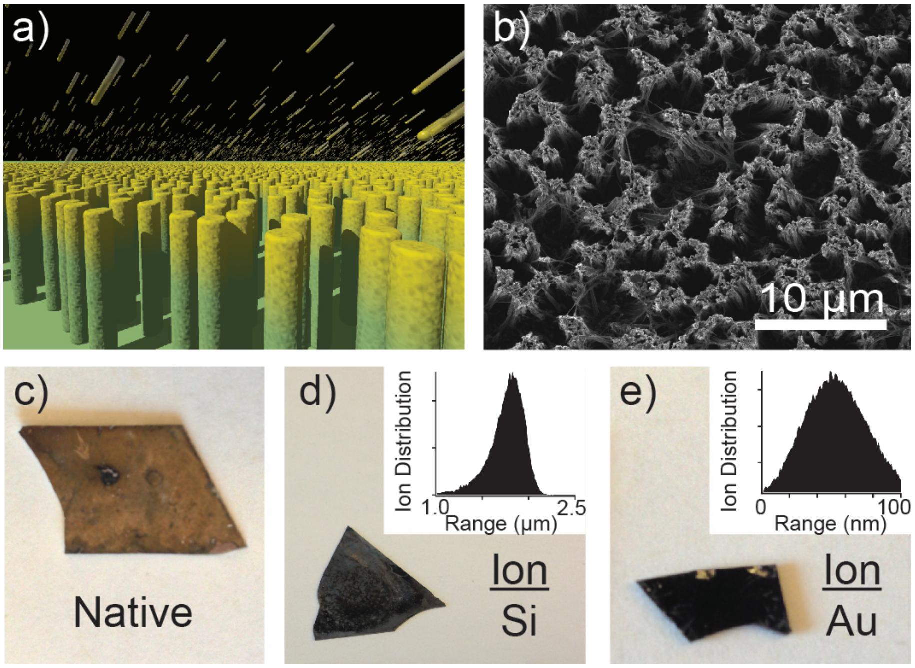

Figure 5.1: a) Illustration showing the gold ion-implantation into the tips of the array of SiNWs. The helium ion microscope (HIM) image (b) shows a magnified section of a post-implanted SiNW array (c). A color change of the SiNW array following silicon (d) and gold (e) ion-implantation is evidence of increased light absorption. SRIM[91] simulations of the ion implantation depth profiles are also presented for the silicon (d, inset) and gold (e, inset) ions.

The resulting structure of the ion implanted silicon nanowires were characterized using transmission electron microscopy, select area electron diffraction, energy dispersive x-ray spectroscopy, and Raman spectroscopy. Due to the large penetration depth of the silicon ions during implantation, silicon nanowires implanted with silicon ions show uniform damage along the entirety of the nanowire, as indicated by the constant SAED patterns showing partial crystalline and partial amorphous character[144] shown in the insets of Fig. 5.2a. The energy-dispersive x-ray (EDX) spectra in Fig. 5.2b reflect that the elemental composition of the nanowire is also constant throughout, showing a strong silicon and an oxygen peak with carbon and copper peaks originating from the lacey carbon TEM grid. Contrary to the

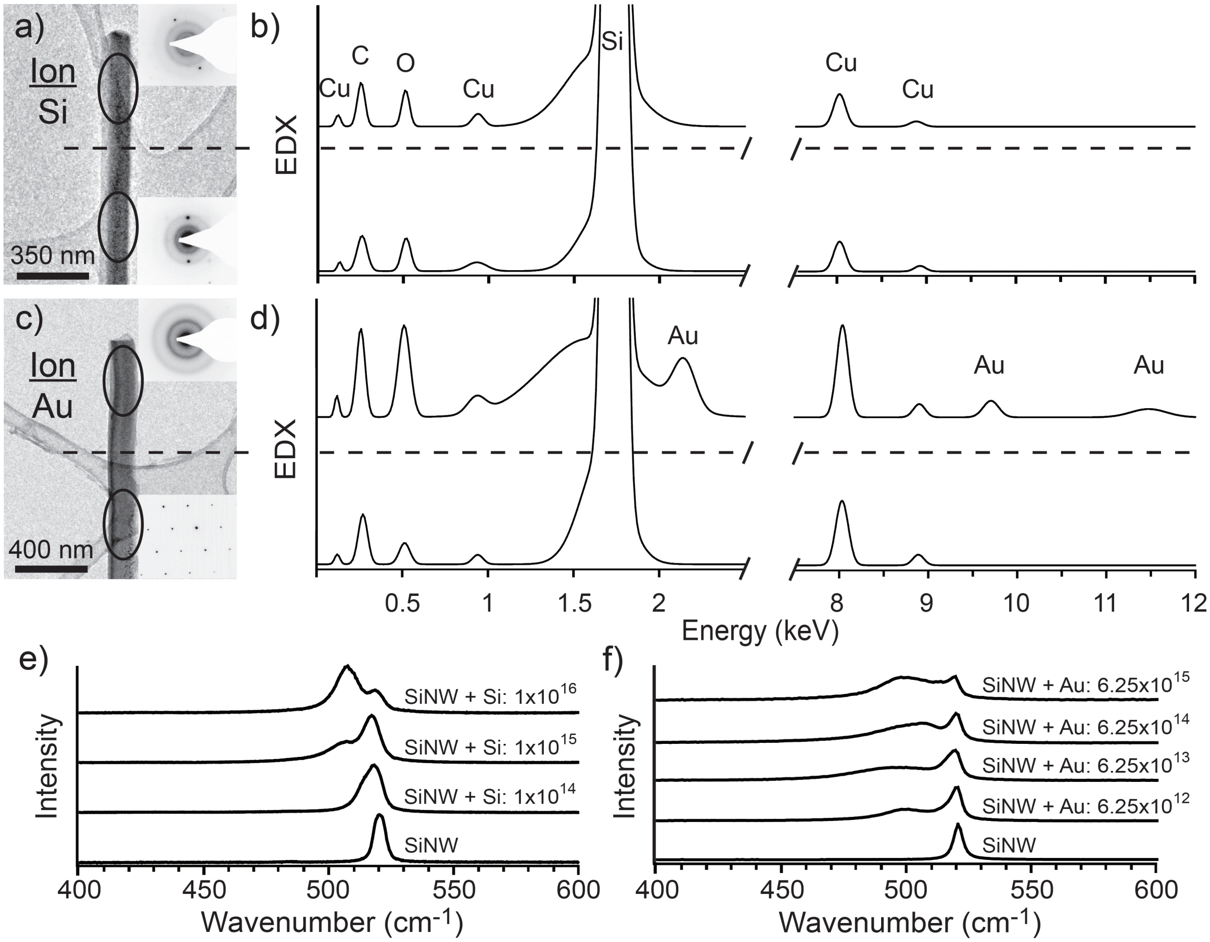

Figure 5.2: Corresponding TEM bright field image, SAED, and EDX spectra of of a silicon-implanted (a,b) and gold-implanted (c,d) SiNWs. Raman spectra showing increased amorphization and lattice damage from increasing (e) silicon and (f) gold implantation dosage.

silicon-implanted silicon nanowires, the gold-implanted silicon nanowires show a localization of gold to a single end of the nanowire. The SAED pattern (Fig. 5.2c, top-right inset) at the tip of the nanowire shown in Fig. 5.2c shows diffuse Debye rings, suggesting complete amorphization[144]. The EDX spectrum at the same site (Fig. 5.2d, top) shows gold peaks, but those peaks and amorphous SAED pattern diminish as the nanowire is probed further from the tip, as shown in Fig. 5.2c. Lastly, damage to the single-crystalline silicon lattice from ion-implantation can be seen with increasing ion dosage by observing the emergence of an amorphous silicon peak red-shifted with respect to the native single-crystalline Raman peak at 520 cm^{-1} in the Raman spectra[145–147] for both silicon and gold ion-implanted silicon nanowire arrays in Fig. 5.2e,f.

5.2.1 Characterization details

Ion Implantation: Silicon nanowire arrays were implanted with gold and silicon ions using a 3 MeV tandem accelerator from National Electrostatic Corporation (9SDH-2). The acceleration energy, incident beam angle, and ion doses were chosen based on calculations using the simulation package SRIM[91]. For the gold ion implantation, an acceleration voltage of 500 keV at a 68 degree incidence angle was used. For the silicon implantation, an acceleration energy of 2 MeV at an incident angle normal to the sample was used.

Transmission Electron Microscopy: Bright field images were taken on a FEI Tecnai G2 F20 at an acceleration voltage of 200 keV. SAED images were taken with camera lengths of 490 mm and 600 mm. EDX spectra were obtained with a 60 second acquisition time at a rate of approximately 2000 counts/second. The spectra were then processed by subtracting the background and using a multi-peak fitting software to identify and smooth the peaks.

Helium Ion Microscopy: Helium ion microscopy was performed using a Zeiss Orion Plus Helium Ion Microscope. The He$^+$ ion beam was accelerated using a voltage of 30 keV with a dwell time of 30 μs and blanker current of 1.3 pA.

Raman Spectroscopy: Raman spectra were acquired on a lab-built setup using a Coherent Compass 532 nm laser with 19 mW of output focused onto the sample with a Mitutoyo 50x objective (NA = 0.55). Back-scattered photons were collected through the same objective and focused onto an Acton SpectraPro 500i spectrometer with a Princeton Instruments liquid nitrogen-cooled silicon charge coupled device. Wavenumber values were corrected using modes from a cyclohexane sample measured in the same setup.

5.3 Results and discussion

The ion-implanted silicon nanowires were subsequently trapped in a single-beam 975nm laser tweezer shown in Fig. 2.1 and nanowire temperatures where determined using the method from Sec. 2.5.2 with HBM analysis from Sec. 4.2. Figure 5.3 shows the HBM temperature extraction results of trapping at least five silicon nanowires of each implantation type and dose at seven different laser irradiances between 5.3 − 15.6 MW/cm^2 at a trapping wavelength of 975 nm.

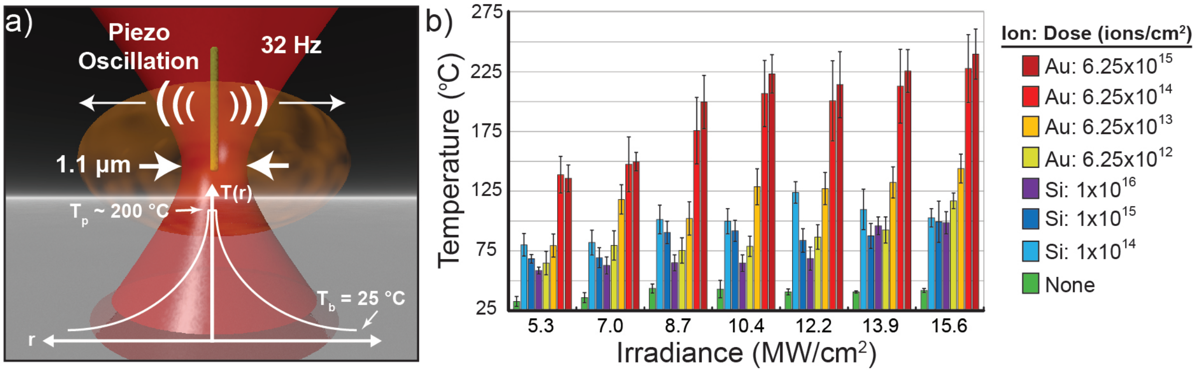

Figure 5.3: a) Illustration of a trapped SiNW undergoing HBM. b) Results from the HBM temperature extraction method of optically trapped ion-implanted SiNWs using a 975 nm focused laser source. Error bars represent the standard deviation in the extracted temperatures between implanted SiNWs.

The HBM temperature analysis necessitates knowledge of the particle size for the morphology-dependent component g of the Stokes' drag coefficient, which for a direction transverse to the nanowire axis is given by Eq. 4.4. However, often the silicon nanowire diameter lies below the diffraction limit of the illumination source. Therefore, care needs to be taken when using image analysis techniques to determine the diameter of the silicon nanowires. In order to account for this, a method for determining the size of a silicon nanowire in the laser trap chamber was developed and compared with SEM analysis as shown in Fig. 5.4.

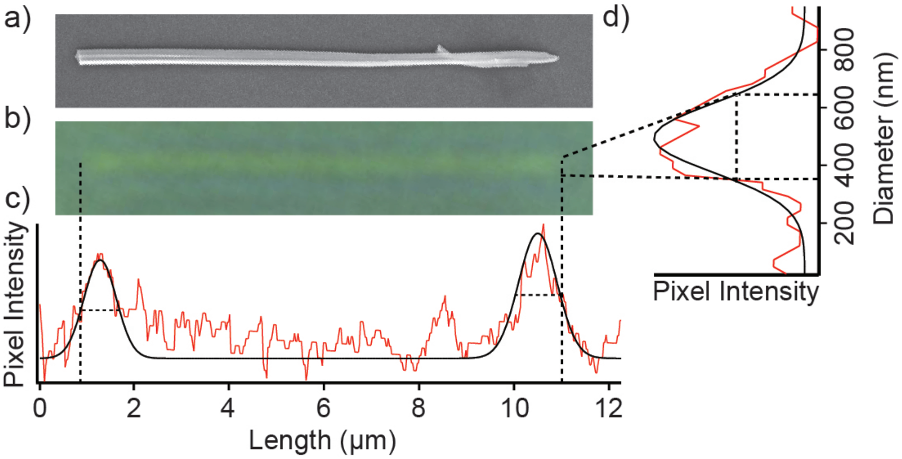

Figure 5.4: a) SEM image of a SiNW on a coverslip of a trapping chamber. b) A CCD camera image of the same SiNW in the water-filled trapping chamber. Image pixel intensity line profiles with gaussian fits from the (c) length and (d) diameter of the same SiNW from (b). Dashed lines across the gaussian peaks indicate the full width at half maximum that is used to calculate the size of the nanowires.

To extract the dimensions of the silicon nanowires, a calibrated CCD camera image is taken of the silicon nanowire in focus lying flat against the chamber surface. The image is then converted to grayscale and pixel value intensity line profiles are drawn across the length and diameter of the silicon nanowire as shown in Fig. 5.4c,d. The edges of the silicon nanowire show up as a peak in pixel intensity in the line profiles. These peaks are fit to a gaussian curve and the FWHM is used as the initial and final points for the length and diameter measurement. Lastly, the procedure was then repeated ten times in order to decrease uncertainty.

To test the effectiveness of this method, five silicon nanowires where imaged in a trapping chamber and their sizes were calculated using the method outlined above. Then, the sample chamber was dehydrated and taken to an SEM for high resolution imaging. Lastly, the silicon nanowire sizes were determined from SEM data and compared to the size extraction method. Results of the study showed that the analysis worked to within 25% uncertainty for nanowires greater than 250 nm in diameter, with the uncertainty decreasing as the diameter increases. Therefore, no data in Fig. 5.3b was presented for silicon nanowires with diameters less than 280 nm. As an example, the silicon nanowire shown in Fig. 5.4 has a length of 10.07 μm and a diameter of 290 nm ± 36 nm as determined by SEM. Using the image analysis method, the results show 10.12 μm long and 312 nm ± 58 nm in diameter which is within the SEM error.

Using this size analysis method, the size distribution of the trapped silicon nanowires presented in Fig. 5.3b was 455 nm ± 117 nm diameter and 6.65 μm ± 3.78 μm. By comparing the silicon-implanted silicon nanowires with the non-implanted silicon nanowires, it is evident that the damage to the crystalline lattice from the implantation process causes an increase in the PT heating efficiency, likely due to the increased density of charge and phonon scattering at the implantation-induced defect sites within the nanowires. Moreover, it is important to note that an increase in the silicon ion dosage does not seem to result in a significant change in the nanowire heating, suggesting that the contribution of the lattice damage as a mechanism to the nanowire heating has reached a saturation limit.

For the gold ion-implanted nanowires, the lowest dosage shows temperatures comparable to those of the silicon ion-implanted nanowires. However, as the gold ion concentration increases, the temperature of the trapped nanowires also increases dramatically to a point of superheating water above 200 °C. Superheating water without bubble formation by trapping gold nanoparticles with 10 nm radii of curvature has recently been reported[40] and was attributed to the large thermal energy needed to overcome the large Maxwell-Young interfacial surface pressure at the surface of the trapped nanoparticle. The increased PT heating efficiency as a function of the increased gold-ion dosage is likely due to the increased light absorption at 975 nm as well as an increased free carrier density to respond to the generated internal electric fields within the nanowire. The mechanism for increased absorption from the gold ion-implanted silicon nanowires is unclear, but could be due to the formation of gold-related deep level traps in silicon[148]. The increase in the error bars for the highly dosed gold-implanted nanowires suggests that the amount of gold accumulation between silicon nanowires varies greatly and causes a large spread in PT heating enhancement from nanowire-to-nanowire. This is likely caused by the irregularity of the fabricated silicon nanowire array as shown in Fig. 5.1b and consequently results in an inhomogeneous ion implantation into the silicon nanowires. Furthermore, during trapping of the highest dosage

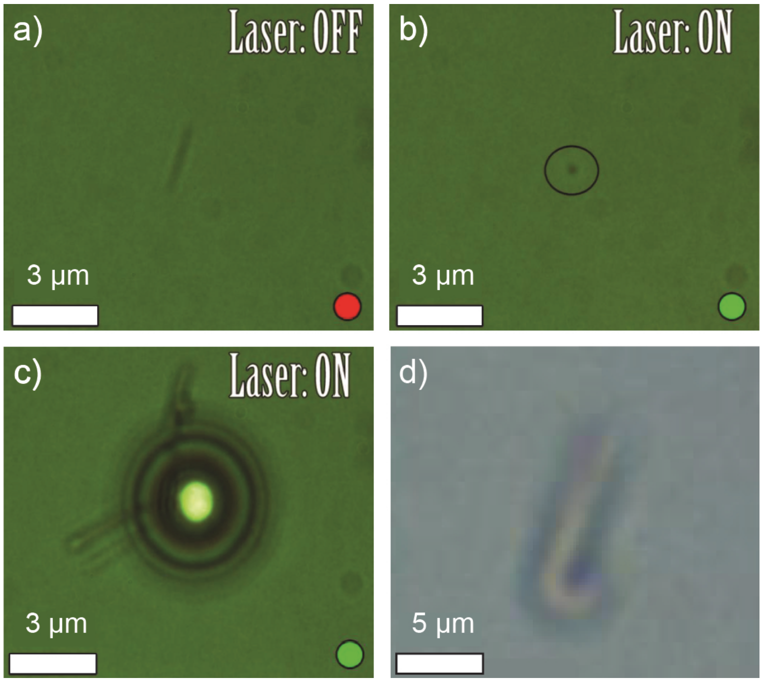

Figure 5.5: a) Video frames of a gold ion-implanted SiNW in Brownian motion before the 975 nm trapping laser is turned on and the SiNW is trapped (b). c) The SiNW is then brought into proximity of other gold ion-implanted SiNWs that are attached to the glass coverslip and a bubble is generated. d) Image of a gold ion-implanted SiNW after an unsuccessful trapping attempt showing a morphology change on one side of the SiNW. Before the trapping attempt, the end of the SiNW was not curved.

gold-implanted nanowires, we also noticed both changes in the nanowire morphology after trapping as well as bubble formation when the trapped SiNW was brought in proximity with other gold-implanted nanowires attached to the surface, as shown in Fig. 5.5.

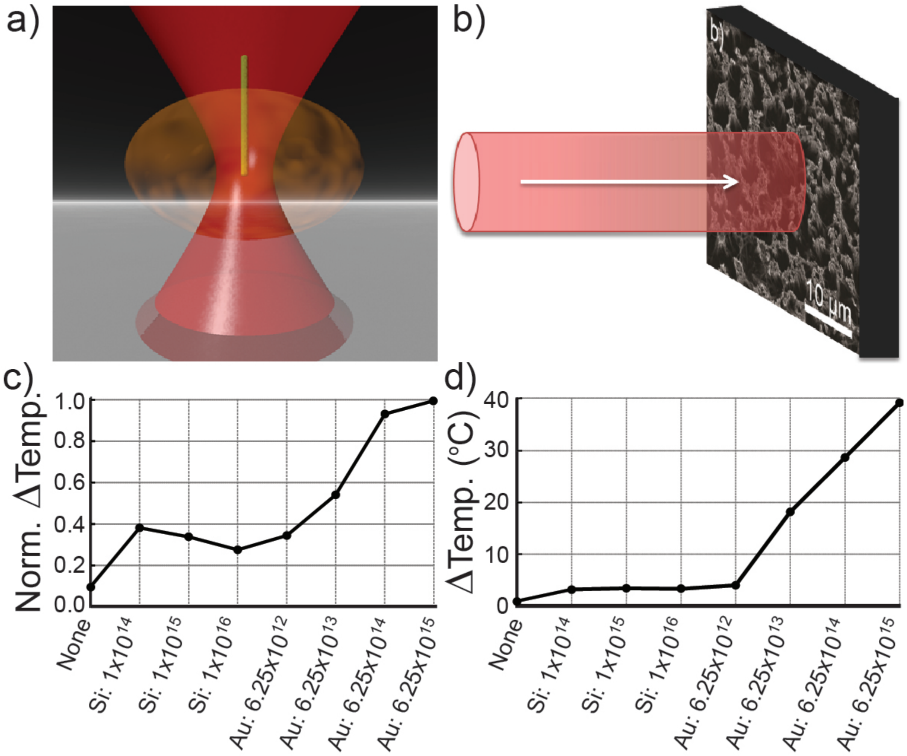

Figure 5.6: a) Illustration of a optically trapped nanowire for data presented in (c). b) Illustration of a SiNW array temperature measurement for data presented in (d). c) Plot of the average temperature increase for each doping level shown in Fig. 5.3b normalized to the maximum temperature increase at each irradiance. d) Plot of an array of SiNWs heated in air by an unfocused 975 nm laser.

To corroborate the results from our HBM temperature extraction method, we also compared the heating trend results from Fig. 5.3b, Fig 5.6a,c) with the trend for the silicon nanowire arrays (Fig. 5.6b,d) heated in air by an unfocused 975 nm laser with a beam diameter of 3 mm and laser power of 50 mW measured with a thermocouple out of the beam path. The similarity in the heating trends suggests that the HBM temperature extraction method detailed in the main manuscript is a powerful method for extracting particle temperature information from individually-trapped nanoparticles in a single-beam optical trap.

Future research into further enhancement of PT heating efficiencies of ion-implanted silicon nanowires could be realized by altering the gold implantation profile to be uniform throughout the nanowire length. Another approach to increasing PT heating efficiencies would be to follow gold implantation with a thermal annealing step, which may allow for formation of gold nanoclusters[149] within the nanowires of a size that could allow them to be more efficient absorbers of the incident NIR radiation and inhibit ion migration to the nanowire surface. Likewise, alternative methods to obtain metallic nanoclusters, such as silver nanoclusters with tunable and uniform sizes[150], could also drastically increase PT heating efficiencies while removing the need for an implantation processing step.

5.4 Conclusion

In this chapter, we have shown that we can measure quantitatively the temperature of optically trapped engineered particles and demonstrated the laser tweezer as a versatile instrument for studying the superheating of water from optically trapped nanoparticles and their efficacy as PT agents. We have also shown that the PT heating efficiency of silicon nanowires can be increased by causing lattice damage through ion implantation which produces scattering sites that impede heat and charge transport. Additionally, the efficiency of silicon nanowire PT heating was shown to increase significantly by implanting with gold ions that drastically increase absorption at the 975 nm trapping wavelength and cause superheating of water of over 200 °C at the trap site. We expect that this HBM temperature extraction analysis method for laser tweezers will be used to further explore nanoparticles for PT therapy applications as well as to inform how to quantify laser-induced heating effects during laser trapping experiments in various fields of study including cavity optomechanics and single-molecule biophysics.

5.5 Acknowledgments

We acknowledge S. Manandhar and S. Shutthanandan for nanowire array ion implantation and HIM characterization, B. E. Smith for Raman spectroscopy characterization, X. Zhou for SEM characterization, Klaus Kroy of Leipzig University for discussion of HBM analysis, and E. J. Davis for heating analysis comments and providing an optical spectrometer with LN_2-cooled detector. We thank the University of Washington NanoTech User Facility (NTUF) as well as the Pacific Northwest National Laboratory Environmental Molecular Sciences Laboratory (PNNL EMSL) for use of instruments at their facility. This research is supported in part by the Air Force Office of Scientific Research Young Investigator Award (Contract #FA95501210400), the NSF Graduate Research Fellowship (DGE-1256082), and start-up funding from the University of Washington.

Chapter 6

COLD BROWNIAN MOTION IN AQUEOUS MEDIA VIA ANTI-STOKES PHOTOLUMINESCENCE

6.1 Introduction

Up until this chapter, we have focused solely on photothermal heating of particles in an optical trap. The thought of an object cooling down when exposed to light, a form of energy, is perplexing and counterintuitive as it suggests a violation of conservation of energy. Yet, laser refrigeration of materials via phonon-mediated anti-Stokes photoluminescence has previously been reported to cool to near-cryogenic temperatures in vacuum. In 1929, Pringsheim[151] proposed that solid-state materials could experience refrigeration if they exhibited biased emission of anti-Stokes (blue-shifted) radiation relative to a fixed optical excitation wavelength. Epstein[152] and colleagues experimentally demonstrated this concept first in 1995 using rare-earth-doped fluoride glass materials (ZBLAN). More recently, the laser refrigeration of doped yttrium aluminum garnet (Yb^{3+}:YAG) materials has recently been reported in air at atmospheric pressure[153]. Anti-Stokes photoluminescence has also been shown[154] to cool cadmium sulfide (CdS) nanoribbons *in vacuo* by as much as 40 °C below room temperature. Of these anti-Stokes cooling materials, the solid-state rare-earth-doped yttrium lithium fluoride (Yb^{3+}:YLF) crystals have reported the most impressive results and have been cooled to cryogenic temperatures[155] *in vacuo* using a continuous-wave NIR laser excitation.

In contrast to anti-Stokes processes, optomechanical laser refrigeration of nanomaterials has also been demonstrated based on a novel mechanism of angular momentum transfer between a circularly polarized laser and a birefringent crystal[156]. Still, laser refrigeration of nanoparticles in aqueous media has not been reported stemming in part from the large NIR optical absorption coefficient of water[58]. It has remained an open question whether these known cooling materials could act to refrigerate aqueous media and undergo hypothesized cold Brownian motion (CBM): the cold analog of HBM. In this work, we demonstrate the local refrigeration of aqueous media by > 21 °C below ambient conditions following anti-Stokes photoluminescence from optically trapped, rare-earth-doped YLF nanoparticles undergoing CBM.

6.2 Yb^{3+}-doped yttrium lithium fluoride

$YLiF_4$ (YLF for short) is a insulating crystalline material well known for its use as a laser gain medium. As we will discuss, the laser refrigeration mechanism of Yb^{3+}-doped YLF requires long excited state lifetimes of the substitutional Yb^{3+} ion. YLF makes an ideal laser refrigeration (and laser gain) host because it has a large bandgap ($\sim$300 nm) and is therefore transparent to the pump laser wavelength (1020 nm), which minimizes absorption and subsequent heating[157]. Furthermore, YLF also has a relatively low two-photon cross-section as well as low phonon energies[158] which minimize the non-radiative decay rates in the crystal. This in turn leads to less heat dissipated in the crystal[158]. Together, these properties of YLF allow for substitutional Yb^{3+} ions to experience long excited state lifetimes and enable laser refrigeration. To achieve laser refrigeration with YLF, we substitute up to 10% of the yttrium (Y^{3+}) ions with optically-active ytterbium ions (Yb^{3+}), subsequently rendering the crystal slightly absorbing in the NIR.

6.2.1 Laser refrigeration with anti-Stokes photoluminescence

The electronic configuration of ytterbium is $[Xe]4f^{14}6s^2$. To form the trivalent ytterbium ion, the outermost $6s$ electrons are removed followed by a single $4f$ electron, giving the ion an electron configuration of $[Xe]4f^{13}$. There are a couple considerations that arise from this electronic configuration. First, the Yb^{3+} ions have a relatively small radius and are partly shielded from external fields by the filled $5s$ and $5p$ shells [159]. This screening of the optically active levels of the ion works to reduce the crystal-field effects from the host crystal[159]. Secondly, the absence of the single $4f$ electron gives the ion a total spin of S

= 1/2 and total orbital angular momentum L = 3. The non-zero values of S and L give rise to a spin-orbit interaction that lifts the degeneracy of the ^{2}F manifold into $^2F_{5/2}$ and $^2F_{7/2}$ multiplets[160]. The energy level splitting by the spin-orbit interaction is much larger than that of the crystal-field interaction for Yb^{3+}:YLF because 1) the spin-orbit interaction varies roughly as Z^2[159] ($Z_{\mathrm{Yb}} = 70$), and 2) the screening of the 4f electrons by the 5s and 5p shells diminishes the crystal-field interaction. Thus, the spin-orbit interaction serves to create the $^2F_{5/2}$ and $^2F_{7/2}$ multiplets with an energy separation of ∼1 μm and the crystal-field interaction further lifts the respective 3-fold and 4-fold degeneracy of said multiplets, allowing for efficient phonon-mediated upconversion between the sub-bands. Moreover, theoretical calculations suggest that nanocrystalline materials may exhibit higher cooling efficiencies than bulk single crystals[157] based in part on a broadening of the phonon density of states at nanometer grain sizes.

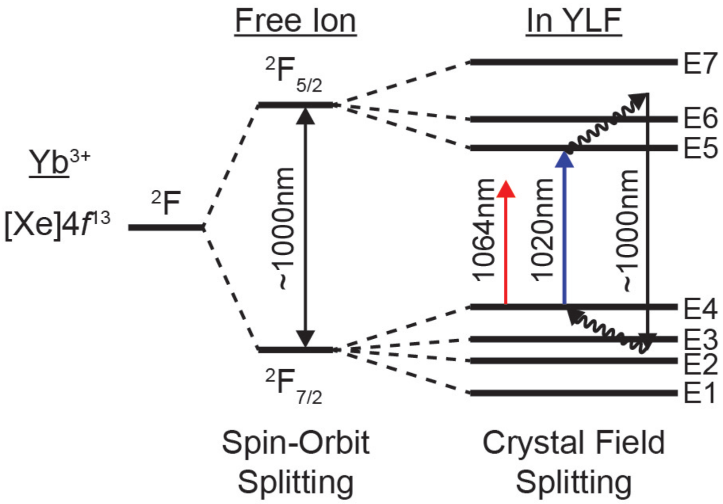

Figure 6.1: Diagram of the electronic configuration of the Yb^{3+} free ion and the substitutional Yb^{3+} ion in the YLF crystal host. The anti-Stokes photoluminescence refrigeration process occurs for the material when pumped at the E4-E5 resonance (λ=1020nm) and does not occur when λ <1020nm (e.g. λ=1064nm).

When the Yb^{3+}:YLF is irradiated by a wavelength that is at the $^2F_{7/2}\rightarrow{}^2F_{5/2}$ energy gap, an electron at the highest level of $^2F_{7/2}$ (E4) can be excited to the lowest level of $^2F_{5/2}$ (E5) directly. Since the E5 level has a long lifetime in the YLF host, the excited electron has a large probability of absorbing an optical phonon from the YLF host crystal thereby upconverting the electron to an even higher energy state (E6 or E7). The upconverted electron then eventually decays radiatevly across the energy gap by emitting a photon that has an energy larger than the pump photon by an amount equal to the absorbed optical phonon energy, thereby cooling the YLF host crystal. Using this phonon upconversion mechanism to optically refrigerate a material thereby requires that the pump wavelength be very close to the resonance of the E4-E5 transition, which is λ=1020nm for Yb^{3+} in YLF. When the laser wavelength is insufficient to pump the E4-E5 transition (e.g. λ=1064nm), the cooling mechanism can not occur. These processes are diagramed in Fig. 6.1.

As mentioned previously, the concept of laser cooling via anti-Stokes emission has been around since the 1920s[151]. Initially, many scientists were skeptical of the refrigeration process because it seemed to violate the second law of thermodynamics[157]. The paradox was solved by Lev Landau when he attributed the increase in entropy to the radiation field[161]. Landau showed that the entropy of radiation is related to the frequency bandwidth as well as the directional spread of the radiation. Thus, the issue of the paradoxical decreasing entropy was rectified by the fact that the pump laser has a very narrow spectral linewidth and has a very narrow directionality (almost zero entropy) whereas the anti-Stokes emission from the host material has a relatively broad bandwidth and propagates in all directions (relatively large entropy).

6.2.2 Ratiometric thermography with codoped Yb^{3+}, Er^{3+} ions

Furthermore, it is possible to obtain strong visible upconversion in host crystals that are codoped with different rare-earth ions[162]. Figure 6.2a illustrates how the Yb^{3+} ion can act as a sensitizer to an Er^{3+} ion, where an excited electron in the Yb^{3+} ion's $^2F_{5/2}$ level can resonantly transfer its energy to excite the Er^{3+} ion's $^4I_{11/2}$ level. Moreover, this process can then happen again and promote the electron in the Er^{3+} ion's $^4I_{11/2}$ level to its $^4F_{7/2}$ level. The excited electron in the Er^{3+} ion's $^4F_{7/2}$ level then non-radiatevly relaxes to either the $^2H_{11/2}$ or $^4S_{3/2}$ levels, both of which have long (ms) lifetimes[162]. These long-lived excited states then radiatevly emit upconverted green light in two distinct bands: $\lambda \approx$525nm from the $^2H_{11/2}$ level and $\lambda \approx$550nm from the $^4S_{3/2}$ level .

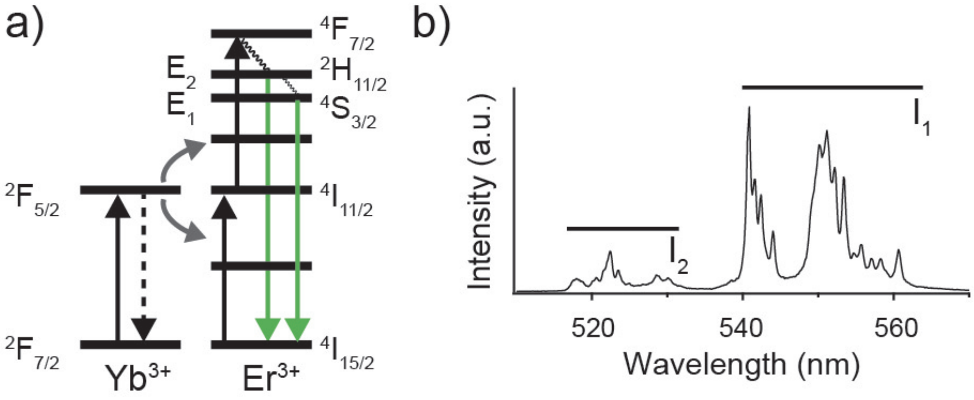

Figure 6.2: a) Illustration of green upconversion with Yb^{3+}/Er^{3+} codoped YLF. b) Corresponding photoluminescence showing emission bands I_2 and I_1 corresponding to radiative relaxation from Er^{3+} E_2 ($^2H_{11/2}$) and E_1 ($^4S_{3/2}$) levels, respectively.

The long lifetimes of photoluminescence from the rare-earth point defects in YLF may also be used to infer temperature changes through ratiometric thermometry by analysis of Boltzmann thermal populations[163], which is given by the equation:

$$\frac{I_2}{I_1} \propto \exp\left[\frac{-(E_2 - E_1)}{k_B T}\right] \tag{6.1}$$

Changes in the ratio of the integrated emission bands I_2 and I_1 (Fig. 6.2b) that stem from transitions between energy states E_2 ($^2H_{11/2}$) and E_1 ($^4S_{3/2}$), respectively, and a common ground state ($^4I_{15/2}$) are directly correlated to a change in the particle's temperature. Therefore, we can monitor the temperature of the crystal by measuring its upconversion photoluminescence spectrum, integrating under the distinct emission bands I_2 and I_1, and taking the natural logarithm of the ratio of I_2 and I_1. Since the difference in energy levels E_2 and E_1 are constant, a change in the ratio of the emission bands therefore corresponds to the change of the lattice temperature in the crystal.

6.2.3 Nanoparticle synthesis and characterization

Traditionally, efforts to cool Yb^{3+}:YLF materials *in vacuo* have relied on the growth of high-purity YLF single-crystals using an air- and moisture- free Czochralski process[164]. In the experiments reported here, a low-cost modified hydrothermal synthesis[165] of Yb^{3+}:YLF was used to prepare YLF crystals shown in Fig. 6.3. SEM analysis reveals that YLF crystals exhibit a truncated tetragonal bipyramidal (TTB) morphology (Fig. 6.3b). X-ray diffraction confirms that the YLF crystal has a Scheelite structure (Fig. 6.3c). Bright field and high-angle annular dark field (HAADF) TEM imaging (Fig. 6.3d,e) and SAED (Fig. 6.3e, inset) suggest that the TTB YLF particles are polycrystalline and likely form through an oriented attachment[166] process of nanocrystalline grains. Figure 6.3f shows an EDX compositional-analysis-spectrum of a YLF crystal taken within the TEM, confirming the elemental crystalline composition including Y, Yb, and F species.

Characterization details

Yb^{3+}:YLF and Yb^{3+}/Er^{3+}:YLF Synthesis The following synthesis was performed following modifications to Lu, C. et. al[165]. Yttrium oxide (Y_2O_3), ytterbium oxide (Yb_2O_3) and erbium oxide (Er_2O_3) of 99.99% purity were used as purchased from Sigma-Aldrich. Yttrium nitrate ($Y(NO_3)_3$), ytterbium nitrate ($Yb(NO_3)_3$) and erbium nitrate ($Er(NO_3)_3$) were obtained by dissolving the oxide in concentrated nitric acid at 60 °C while stirring for several hours until the excess nitric acid was removed. The residual solid was then dissolved in Millipore DI water to achieve a stock concentration of the respective nitrate. Lithium fluoride (LiF), nitric acid (HNO_3), ammonium bifluoride (NH_4HF_2) and ethylenediaminetetraacetic acid (EDTA) of analytical grade were used directly in the synthesis without any purification. The following preparation uses the synthesis of 2%Er^{3+},10%Yb^{3+}:$YLiF_4$ as an

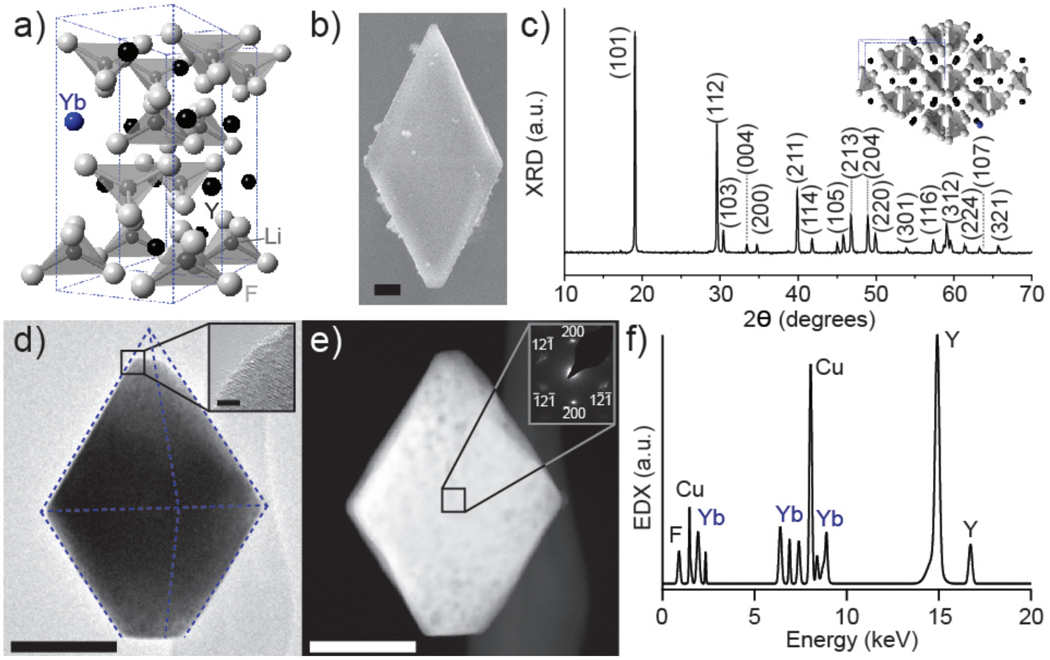

Figure 6.3: a) Schematic of the scheelite crystal structure of YLF with $I_{41/a}$ space group symmetry. b) SEM image of a faceted Yb^{3+} YLF particle (scale bar = 1 μm). c) XRD of hydrothermal YLF crystals . d) BF TEM image of an individual Yb^{3+}:YLF grain (scale bar = 200 nm). Inset: HR-TEM image taken from the indicated region (scale bar = 2 nm). e) HAADF TEM image of the YLF grain in panel b. Inset: SAED from the indicated region. f) EDX of YLF crystal taken in d,e.

example. 7.04ml of 0.5M $Y(NO_3)_3$, 0.8ml of 0.5M $Yb(NO_3)_3$ and 0.16ml of 0.5M $Er(NO_3)_3$ were mixed with 1.17g EDTA in 5ml Millipore DI water at 80 °C while stirring for 1h. We call this solution A. Subsequently, 0.21g of LiF and 0.68g of NH_4HF_2 were dissolved in 7ml Millipore DI water at 70 °C while stirring for 1h to form solution B. Solutions A and B were mixed together while stirring for 20min to form a homogeneous white suspension which is then transferred to a 23ml Teflon-lined autoclave and heated to 220 °C for 72h. After the autoclave cools to room temperature, the 2%Er^{3+},10%Yb^{3+}:$YLiF_4$ particles can be recovered by centrifuging and washing with ethanol and Millipore DI water three times. The final white powder was obtained by calcining at 300 °C for 2h. 10%Yb^{3+}:$YLiF_4$ particles were achieved using the same method.

Transmission Electron Microscopy: Bright field and STEM HAADF images were taken on a FEI Tecnai G2 F20 at an accelerating voltage of 200 keV. Select area electron diffraction (SAED) images were taken with a camera length of 490 mm. EDX spectra were obtained with a 60 second acquisition time. The spectra were then processed by subtracting the background and smoothing the peaks.

Scanning Electron Microscopy: Secondary electron images were taken on an FEI Sirion at an accelerating voltage of 5 keV.

X-ray Diffraction: Powder XRD patterns are obtained on a Bruker F8 Focus Powder XRD with Cu K (40kV, 40mA) irradiation (λ=0.154nm). The 2θ angle of the XRD spectra was from 10° to 70° and the scanning rate was $0.01^\circ s^{-1}$. The one minor unlabeled peak in the XRD spectra at $2\theta = 44.9^\circ$ is attributed to a small amount of unreacted LiF precursor ((200) peak).

Yb^{3+} Ion Spacing

According to the XRD data presented in Fig. 6.3c, the lattice parameters of 10%Yb^{3+}:YLF are a = 5.1641 Å and c = 10.7177 Å and the volume of the corresponding unit cell is $V_0 = a^2 * c = 2.85*10^{-28}$ m^3. For 1 m^3 YLF, the number of unit cells is $n = 1$ m$^3/V_0 = 3.5*10^{27}$ m^{-3}. For each unit cell, there are 4 rare earth atoms. The total number of rare earth atoms in 1 m^3 is $n_t = 4n = 1.4*10^{28}$ m^{-3}. For 10%Yb^{3+}:YLF, the number of Yb atoms in 1 m^3 is $n_{Yb} = 0.1*n_t = 1.4*10^{27}$ m^{-3}. The linear density of Yb atoms is $p = (n_{Yb})*(1/3) = 1.11*10^8$ m^{-1} and the average ion spacing is approximately $l = 1/p = 8.9$ Å.

6.3 Cold Brownian motion of locally refrigerated Yb^{3+}:YLF

The Yb^{3+}:YLF particles were trapped in a single-beam laser tweezer shown in Fig. 2.1 and temperatures where determined using the method from Sec. 2.5.2 with HBM analysis from

Sec. 4.2. Typically, HBM analysis is applied to situations where the particle of interest is at an elevated temperature compared to its surrounding medium. However, the analysis is also appropriate for particles at a temperature less than its surrounding environment, which is termed cold Brownian motion (CBM). Here, the TBB Yb^{3+} crystals are approximated as being spherical with radius R, where the morphology-dependent component g of the Stokes' drag coefficient (Eq. 1.12) is given by $g = 6\pi R$. Trapping data was acquired using a diode-pumped solid state Yb:YAG thin-disk tunable laser (VersaDisk 1030-10, Sahajanand Laser Technologies) at a wavelength of 1020 nm, a 975 nm pigtailed Fiber Bragg Grating (FBG) stabilized single-mode laser diode (PL980P330J, Thorlabs), as well as a solid-state Nd:YAG 1064 nm (BL-106C, Spectra-Physics) at an irradiance of 5.9, 10.7, 14.6, 21.2, and 25.5 MW/cm^2. Nanocrystals were trapped at the center ($\sim$75 μm from the surface) of the temperature controlled perfusion chamber (RC-31, Warner Instruments) and held at T_b = 25 °C while voltage traces were recorded at the QPD for 3 seconds at a sample rate of 100 kHz. The QPD voltage signal was calibrated by oscillating the piezostage at 32Hz and an amplitude of 150nm peak-to-peak during signal acquisition, as outlined in Sec. 2.5.2. Each YLF CBM temperature extraction result in Fig. 6.4b represents an average of 6 individual particles with an average radius of 764 nm with a standard deviation of 293 nm. In order to minimize fluid absorption and heating at the trapping wavelengths[45], laser trapping experiments were performed in D_2O unless explicitly stated otherwise.

A bright-field micrograph for a characteristic optically-trapped Yb^{3+}:YLF crystal is shown in the inset of Fig. 6.4a. The dependence of laser refrigeration on the trapping laser's pump wavelength is shown in Fig. 6.4b, where YLF crystals doped with 10% Yb^{3+} are observed to cool from 19 °C at a 5.9 MW/cm^2 trapping irradiance to 4 °C at a 25.5 MW/cm^2 trapping irradiance when trapped with $\lambda = 1020$ nm, which is resonant with ytterbium's E4-E5 transition shown in Fig. 6.1. The same Yb^{3+}:YLF crystals are shown to heat from 40 °C to 47 °C when trapped at the same respective irradiances with $\lambda = 1064$ nm, which is energetically insufficient to pump the E4-E5 resonance and subsequently cannot initiate upconversion-mediated cooling (Fig. 6.1).

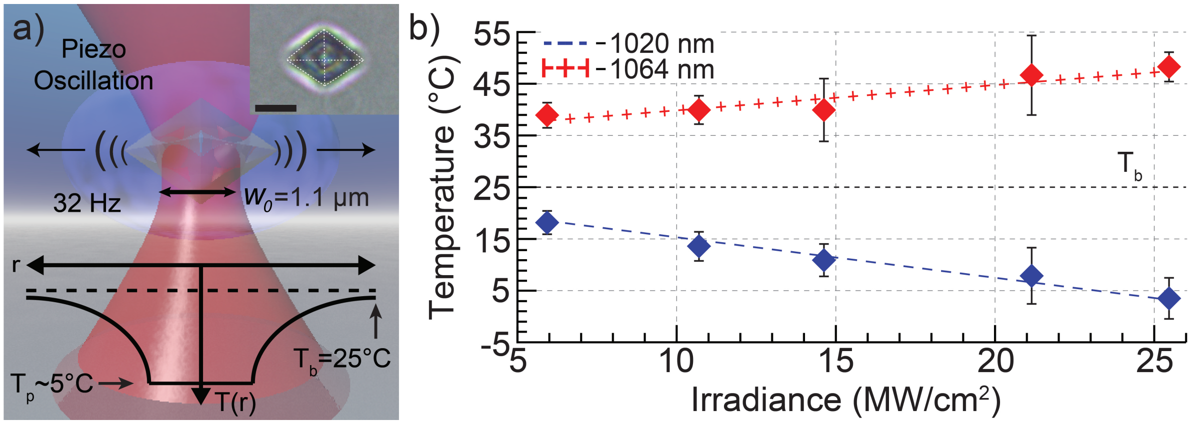

Figure 6.4: a) Illustration of a trapped Yb^{3+}:YLF particle undergoing CBM. Inset: optical micrograph of an optically trapped Yb^{3+}:YLF crystal (scale bar = 3μm). b) Results from the CBM temperature extraction method of optically trapped Yb^{3+}:YLF particles showing cooling when the trapping wavelength is resonant with the E4-E5 transition (λ = 1020 nm, blue) and heating when the trapping wavelength is below the transition (λ = 1064 nm, red). Error bars represent the standard deviation in the extracted temperatures between Yb^{3+}:YLF particles.

For the codoped 2%Er^{3+},10%Yb^{3+}:YLF ratiometric particles, substantial fluctuations in upconversion photoluminescence was observed, making bulk calibration measurements inadequate for individual ratiometric temperature measurements. Calibration for ratiometric thermometry of an individual particle is non-trivial in that there exist fluctuations in particle morphology and dopant concentration/distribution that affect the kinetics of the upconversion efficiency and overall spectral profile of the E_1 ($^4S_{3/2}$) and E_2 ($^2H_{11/2}$) to E_{ground} ($^4I_{15/2}$) transitions (Fig. 6.5a). This means that for a given laser power, relative intensities will vary from particle to particle (Fig. 6.5b). It is, therefore, improbable that a comparison of the individual particles' emission ratio of the two transitions to a calibrated ensemble would yield an accurate temperature. For this reason, we use the Boltzmann distribution of

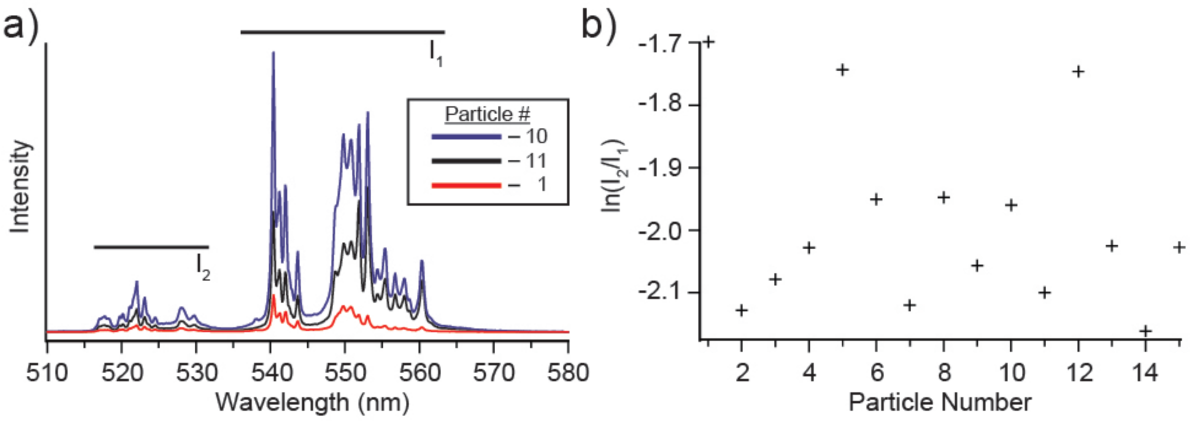

Figure 6.5: a) Select photoluminescence spectra from the measurements in (b) of multiple optically-trapped, codoped 2%Er^{3+},10%Yb^{3+}:YLF particles showing the variability in the integration regions I_2 and I_1, representing emission from Er^{3+} energy states E_2 ($^2H_{11/2}$) and E_1 ($^4S_{3/2}$) to the ground state E_{ground} ($^4I_{15/2}$), respectively. b) Natural logarithm of the ratio I_2/I_1 of different trapped particles showing the particle-to-particle variation.

these electronic states solely in a qualitative manner to confirm the trend of a decreasing or increasing temperature.

With this in mind, we still see a marked difference in the logarithmic ratio of I_2 to I_1 when the upconverting particles are trapped with $\lambda = 1020$nm versus $\lambda = 975$ nm, as shown in Fig. 6.6b. The decrease (increase) in the logarithmic ratio of I_2 to I_1 (Fig. 6.6b) with increasing irradiance reflects a decrease (increase) in the internal lattice temperature[167], which agrees well with the observed temperature changes measured via temperature extraction methods detailed in Sec. 2.5.2 with CBM analysis from Sec. 4.2 (Fig. 6.6c). Specifically, laser trapping analysis of the particles' CBM indicates that codoped 2%Er^{3+},10%Yb^{3+}:YLF undergoes laser refrigeration (ΔT = -4.9 ± 2.8 °C) when trapped at $\lambda = 1020$ nm and heating (ΔT = 21.8 ± 10.11 °C) when trapped at $\lambda = 975$ nm. Furthermore, it has been proposed recently that codoping YLF crystals with other upconverting rare-earth ions can enhance cooling through

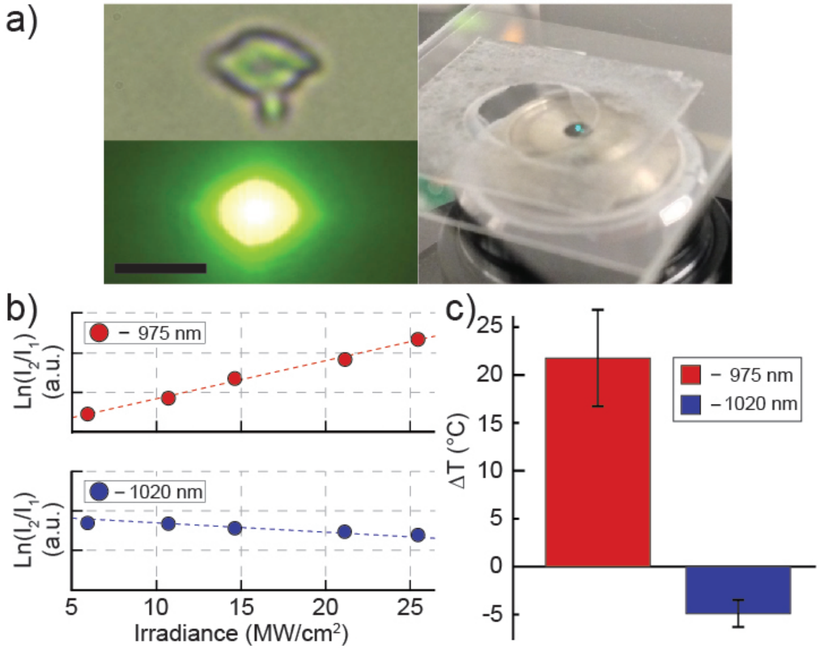

Figure 6.6: a) BF (top) and DF (bottom) image showing a codoped 2%Er^{3+},10%Yb^{3+}:YLF particle in Brownian motion (scale bar = 4μm). Upconverted PL can be seen with the unaided eye (right). b) Logarithmic ratio of I_2/I_1 showing a linear increase (top) with laser irradiance at $\lambda = 975$ nm and a linear decrease (bottom) with laser irradiance at $\lambda = 1020$ nm. c) Laser refrigeration of the codoped YLF crystal analyzed in b measured with CBM analysis.

energy transfer enhanced cooling[168]. The laser trapping and refrigeration of 10%Yb^{3+}:YLF nanocrystals at $\lambda = 1020$ nm in biological buffers such as phosphate-buffered saline (PBS) and Dulbecco's Modified Eagle Medium (DMEM) is also possible, as demonstrated in Table 6.1, where temperature changes are determined between the laser irradiances 5.9 and 25.5 MW/cm^2 and T_b = 25°C. VFT viscosity parameters for DI water, PBS (0.01M, pH 7.4; Sigma P5368), and DMEM (1X, high glucose, pyruvate; Life Technologies Cat. #11995-065) were assumed to be equivalent since it has been reported that water viscosity can be used for purposes of modeling particle transport in non-serum containing media[169].

Table 6.1: Local cooling of Yb^{3+}-doped YLF crystals in various media.

Solvent Type	**ΔT = (T$_p$ - T$_b$) (°C)**	**ΔT Std. Dev. (°C)**
D_2O	-15.0	4.1
DI Water	-14.7	3.8
PBS	-14.9	4.3
DMEM	-11.2	6.3

6.4 Discussion

These results suggest the potential for using singly- and co-doped YLF nanocrystals as a potential platform for various applications, such as precision device and circuit cooling, physiological refrigeration, biological imaging, and *in situ* ratiometric thermometry. Specific applications for these materials include precision temperature control in integrated electronic[170–172], photonic[173, 174], and microfluidic[175] circuits; as well as triggering and probing fundamental temperature-controlled biological processes[98, 175, 176]. The ability to measure and to modulate temperature could enable this technology to investigate kinetics and temperature sensitivity of basic cellular processes, including motor protein dynamics[41], ion channels[177], or to act as simultaneous theranostic-hypothermia agents to identify and treat cancerous tissues[178].

Analyzing the CBM of a nanocrystal dispersed in a liquid phase to measure the nanocrystal's temperature also provides the unique capability to predict the local temperature gradient in the medium surrounding the trapped nanocrystal. Since we approximate the aspect ratio of the TTB as a sphere, the local temperature field is given by[92]:

$$T(r) = T_0 + \frac{R}{r}(T_p - T_b). \tag{6.2}$$

Given that the average radius of the Yb^{3+}:YLF particles trapped at $\lambda = 1020$ nm in Fig. 6.4b is $R_{avg} = 764 \pm 293$ nm, $T_b = 25$ °C, and $T_{p,avg} = 4.3$ °C at 25.5 MW/cm^2 irradiance, the distance away from the particle where the temperature increases to within 1% of T_b is 6.9 μm (Fig. 6.4a).

An important question that has arisen is whether or not Yb^{3+}:YLF nanoparticles can refrigerate the entire particle-medium system rather than just its local environment. That is, we saw in Sec. 6.3 that it is possible to *locally* cool the optically-trapped Yb^{3+}:YLF particle and the solvent nearby. However, the anti-Stokes photoluminescence from the trapped particle has a nonzero probability that it will get reabsorbed in the surrounding solvent or glass coverslips. Therefore, the heat in the system may not be getting reduced, but rather getting displaced. This is why almost all anti-Stokes laser refrigeration experiments are done in vacuum: to minimize the heat load.

Yet, previous work on optically refrigerating a condensed phase has been shown (claimed) by a couple of research labs using rhodamine dye in ethanol[179–181]. These results, however, have come under scrutiny[182, 183]. It is yet to be shown conclusively if any material, dye or rare-earth-doped crystals, can laser refrigerate a condensed phase. The Pauzauskie lab is currently tackling this problem by using techniques presented in this thesis to come up with clever methods to maximize the cooling efficiency of Yb^{3+}:YLF while simultaneously minimizing the reabsorption of the anti-Stokes photoluminescence in the system. For example, future synthetic developments with YLF host crystals could enhance the resonant optical absorption of Yb^{3+} through MDRs as discussed in Sec. 3.4, or reduce unwanted background impurity absorption to a level capable of locally freezing water at atmospheric or elevated pressures.

6.5 Acknowledgments

We acknowledge X. Zhou for hydrothermal and organic synthesis, characterization (XRD, SEM, PL), and performing laser trapping experiments; A. R. Lombardo for organic synthesis, B. E. Smith for operation of the tunable solid-state trapping laser, visible spectroscopy, laser trapping experiments, and computational electromagnetics calculations with DDA; M. J. Crane for conducting laser trapping control experiments, trap alignment, and data analysis, Klaus Kroy of Leipzig University for discussion of CBM analysis, John W. Cahn for discussion of YLF crystallography, and E. J. Davis for manuscript comments and providing an optical spectrometer with LN_2-cooled detector. We thank the University of Washington NanoTech User Facility (NTUF) for use of instruments at their facility, as well as the Lawrence Livermore National Laboratory for a capital equipment donation. This research is supported in part by the Air Force Office of Scientific Research Young Investigator Award (Contract #FA95501210400), the NSF Graduate Research Fellowship (DGE-1256082), the DoD through the National Defense Science & Engineering Graduate Fellowship (NDSEG) Program, and start-up funding from the University of Washington.

Chapter 7

CLOSING REMARKS AND CONCLUSIONS

7.1 Summary of results

Theoretical models, experimental methods, and analysis techniques were developed in order to explore the fundamental parameters of optical heating of nanoparticles and inform the engineering of materials for novel, efficient, and controlled photothermal applications. The effects of size, morphology, crystal structure, and surround medium were determined to be key variables in the light absorption, heat generation, and thermal transport process and drastically effect the final temperature distribution of laser-irradiated one-dimensional structures. Predictions using the theoretical models were compared to temperatures of optically-trapped nanowires determined through techniques developed for a laser tweezer and found to show verisimilar agreement. Lastly, the knowledge gained through these results were used to engineer novel nanoparticles to superheat water and locally refrigerate upon optical trapping. The results presented are not constrained to the materials put forth in this thesis, but rather provide a springboard for future studies requiring precise single-particle photothermal analysis capabilities.

An analytical model of pulsed laser heating of uniform and tapered supported nanowires was developed which takes into account size-dependent thermal parameters. We observed that the taper angle, the size-dependence of the thermal conductivity, and the choice of temperature that constant thermal parameters are evaluated at become increasingly important when determining the rate of heat generation and dissipation. Furthermore, we found that internal temperature distributions and peak specimen temperatures were highly sensitive to the incident laser polarization and subsequent MDRs. By comparing simulation results with experimental data, we saw that these effects on peak temperatures and cooling rates correspond to broadening in the produced time-of-flight ion mass spectra. The results could be used to predict the critical time it takes a pulsed specimen to cool to its base temperature prior to the next pulse, thereby informing ideal APT experimental parameters so that minimal fields for ion evaporation and maximum pulse rates can be attained.

Closed-form analytical calculations were shown for the temperature rise within infinite circular cylinders with nanometer-scale diameters irradiated at right angles by TM-polarized continuous-wave laser sources, allowing for analysis of laser-heated nanowires in a solvated environment. Solutions for the heat source were calculated and results for the corresponding temperature distribution showed that the maximum temperature increase is affected not only by the cylinder's composition, but also by MDRs that lead to significant spikes in the local temperature at particular diameters. Furthermore, nanowires with high thermal transport properties were observed to exhibit extremely uniform internal temperatures during electromagnetic heating to one part in 10^6, including cases where there are substantial fluctuations of the internal electric field source that generates the Joule-heating. Low-absorbing porous nanowires also show extremely narrow MDRs for nanowires with 25% porosity, indicating promising opportunities in the area of photothermal theranostic applications, such as drug loading. Yet, nanowires with 75% porosity were shown to not exhibit fine MDRs, likely due to the reduced reflectivity of an interface between water and a water/nanowire composite that is 75% water. For highly absorbing materials, much higher temperatures are predicted, the internal temperature distribution is non-uniform, and MDRs are not encountered. Extremely low temperatures changes are predicted for nanowires with small diameters, irrespective of porosity or absorbing nature.

The optical heating of laser-irradiated finite nanowires in the framework of a laser tweezer was derived for direct comparison with experiments. Numerical simulations were performed based on nanowires studied in a laser trap to determine the internal fields used for the heating source. Temperature distributions in optically-trapped silicon nanowires were calculated by the model and compared to temperatures obtained by forward-scattered light power spectrum analysis in the back focal plane of the laser tweezer. It was found that for small silicon nanowire radii, it is likely that photothermal heating of the ambient water bath becomes increasingly important, even though it is neglected in the model. For large silicon nanowire radii, it is likely that heating occurs according to the predicted nonlinear dependence that leads to an inhomogeneous, nonlinear temperature field around the nanowire. Motion of cooler fluid near the nanowire acts to reduce the observed temperature relative to what is predicted with the model. Furthermore, we showed that ion-implantation drastically increases the photothermal temperature of trapped silicon nanowires through modulation of the optical (e.g. absorption, complex index of refraction) and thermal (e.g. thermal conductivity) parameters, which is predicted by the model.

An effective method to determine optically-trapped particle temperatures as well as the temperature gradient in the surrounding medium by combining laser tweezer calibration techniques, forward-scattered light power spectrum analysis, and HBM theory was developed. We showed how the technique properly accounts for inhomogeneous temperature fields when determining the temperature of an optically trapped particle. The technique was then applied to measure the temperature of gold- and silicon-implanted silicon nanowires and study the implantation effect on their photothermal efficiencies. The silicon nanowire photothermal efficiency was shown to increase significantly by implanting with gold ions that drastically increase absorption at the 975 nm trapping wavelength and cause superheating of water of over 200 °C at the trap site.

Lastly, novel YLF nanoparticles doped with Yb^{3+} ions were synthesized by the hydrothermal method and optically trapped in a laser tweezer. Through application of developed temperature extraction techniques and HBM analysis, Yb^{3+}:YLF nanoparticles were observed for the first time to undergo cold Brownian motion and locally cool in a condensed phase via anti-Stokes photoluminescence when trapped with a laser wavelength corresponding to the Yb^{3+} E4-E5 resonance (λ=1020nm). Furthermore, YLF codoped with Er^{3+} and Yb^{3+} were synthesized and exhibited intense visible upconversion of the NIR trapping laser that was used to monitor its lattice temperature by ratiometric thermography, which also indicated modest cooling when trapped at λ=1020nm. The results suggest the potential of these materials to investigate kinetics and temperature sensitivity of basic cellular processes, or to act as simultaneous theranostic-hypothermia agents to identify and treat cancerous tissues.

7.2 Closing remarks

One topic that I have not covered in this thesis is the experience of starting a new research lab. As Professor Peter Pauzauskie's first student, I had the privilege of helping build the lab from bare rooms and footprints to the functioning machine that it is today. I could write at length of all of the important components (e.g. simulation and workstation computers, software, microscopes, optical tables, lasers, etc.) and not-so-important components (e.g. lab coat hangers, printers, label maker, etc.) that I helped set up at the lab's initial stages, but there would not be much to learn from the discussion other than one simple fact: it is easier to understand a complex system when you know all of its fundamental parts and how they work together. I took great pride and thoroughly enjoyed (most of the time) building the laser tweezer; including the optics and instrument components, the hardware-computer interface, the computer-software interface, and the software. Having a keen understanding of the instrument that I used for the experiments presented in this thesis provided me with a much greater insight into the data analysis and results than I would have had without having the experience of building the instrument. Yet, today the laser tweezer and optical tables look nothing like what I had initially set up four years ago, and that is because my colleagues in the Pauzauskie group have put an equal amount of effort into understanding the instrument and continue to build upon and modify it in ways that I could not. Even though these efforts often go unnoticed and don't generally result in journal publications, the working knowledge gained often does come across in the quality of research presented.

The results of the theoretical models and the experiments presented in the last few chapters have proven to be of great utility for understanding photothermal interactions in an optical trap and providing insight for engineering nanoparticles for numerous potential optical and thermal applications. However, like all good research, our results have lead to many new, more interesting questions. Many of these questions are currently being investigated and are sure to spring a cornucopia of new, interesting science and applications. I am confident that the Pauzauskie group will continue to make progress in the field optical interactions with nanomaterials and discover new breakthroughs along the way.

LIST OF PUBLICATIONS

[1] **P. B. Roder**, P. J. Pauzauskie, and E. J. Davis. Nanowire Heating by Optical Electromagnetic Irradiation. *Langmuir*, 28(46):16177–16185, 2012.

[2] **P. B. Roder**, B. E. Smith, E. J. Davis, and P. J. Pauzauskie. Photothermal Heating of Nanowires. *The Journal of Physical Chemistry C*, 118(3):1407–1416, 2014.

[3] S. Manandhar*, **P. B. Roder***[1], J. L. Hanson, M. Lim, B. E. Smith, A. Mann, and P. J. Pauzauskie. Rapid Sol-Gel Synthesis of Nanodiamond Aerogel. *Journal of Materials Research*, 29(24):2905–2911, 2014.

[4] **P. B. Roder**, S. Manandhar, Smith B. E., X. Zhou, V. S. Shutthanandan, and P. J. Pauzauskie. Photothermal Superheating of Water with Ion-Implanted Silicon nanowires. *Advanced Optical Materials*, Accepted, 2015.

[5] B. E. Smith, **P. B. Roder**, X. Zhou, and P. J. Pauzauskie. Nanoscale Materials for Hyperthermal Theranostics. *Nanoscale*, 7(16):7115–7126, 2015.

[6] B. E. Smith, **P. B. Roder**, J. L. Hanson, S. Manandhar, A. Devaraj, D. E. Perea, W. Kim, A. L. D. Kilcoyne, and P. J. Pauzauskie. Singlet-Oxygen Generation from Individual Semiconducting and Metallic Nanostructures During Near-Infrared Laser Trapping. *ACS Photonics*, 2(4):559–564, 2015.

[7] **P. B. Roder***, B. E. Smith*, X. Zhou*, M. J. Crane, and P. J. Pauzauskie. Cold Brownian Motion in Aqueous Media via Anti-Stokes photoluminescence. *arXiv Preprint*, arXiv:1503.07265, 2015.

[8] **P. B. Roder***, B. E. Smith*, X. Zhou*, M. J. Crane, and P. J. Pauzauskie. Laser Refrigeration of Hydrothermal Nanocrystals in Physiological Media. *The Proceedings of the National Academy of Sciences of the United States of America*, Submitted.

[9] **P. B. Roder**, S. Manandhar, A. Devaraj, D. E. Perea, E. J. Davis, and P. J. Pauzauskie. Nanowire Heating Associated with Atom-Probe Tomography. *Physical Review B*, In Preparation.

---

[1] * Signifies equal contribution

[10] B. E. Smith*, **P. B. Roder***, and P. J. Pauzauskie. Cavity-Enhanced Harmonic Generation and Hot Brownian Thermometry with Nonlinear Optical Nanowires. *Chemical Physics Letters*, In Preparation.

BIBLIOGRAPHY

[1] J. C. Maxwell. *A Treatise on Electricity and Magnetism*, volume 2. Oxford, 1873.

[2] P. Lebedew. An Experimental Investigation of the Pressure of Light. *Astrophysical Journal*, 15(1):60–62, 1902.

[3] S. Arrhenius. The Cause of the Northern Lights. *Physikalische Zeitschrift*, 2(1):81–87, 1900.

[4] E. F. Nichols and G. F. Hull. A Preliminary Communication on the Pressure of Heat and Light Radiation. *Physical Review (Series I)*, 13:307–320, 1901.

[5] A. Ashkin. History of Optical Trapping and Manipulation of Small-Neutral Particle, Atoms, and Molecules. *IEEE Journal of Selected Topics in Quantum Electronics*, 6(6):841–856, 2000.

[6] A. Ashkin. *Optical Trapping and Manipulation of Neutral Particles Using Lasers: A Reprint Volume with Commentaries.* World Scientific, 2006.

[7] A. Ashkin. Acceleration and Trapping of Particles by Radiation Pressure. *Physical Review Letters*, 24(4):156, 1970.

[8] A. Ashkin and J. M. Dziedzic. Optical Trapping and Manipulation of Viruses and Bacteria. *Science*, 235(4795):1517–1520, 1987.

[9] A. Ashkin. Optical Trapping and Manipulation of Neutral Particles Using Lasers. *Proceedings of the National Academy of Sciences of the United States of America*, 94(10):4853–4860, 1997.

[10] A. Ashkin, J. M. Dziedzic, and T. Yamane. Optical Trapping and Manipulation of Single Cells Using Infrared Laser Beams. *Nature*, 330(6150):769–771, 1987.

[11] A. Ashkin and J. M. Dziedzic. Internal Cell Manipulation Using Infrared Laser Traps. *Proceedings of the National Academy of Sciences of the United States of America*, 86(20):7914–7918, 1989.

[12] H. Liang, W. H. Wright, S. Cheng, W. He, and M. W. Berns. Micromanipulation Of Chromosomes in PTK2 Cells Using Laser Microsurgery (Optical Scalpel) in Combination with Laser-Induced Opitcal Force (Optical Tweezers). *Exp Cell Res*, 204(1):110–120, 1993.

[13] N. W. Charon, S. F. Goldstein, S. M. Block, K. Curci, J. D. Ruby, J. A. Kreiling, and R. J. Limberger. Morphology and Dynamics of Protruding Spirochete Periplasmic Flagella. *Journal of Bacteriology*, 174(3):832–840, 1992.

[14] P. J. Pauzauskie, A. Radenovic, E. Trepagnier, H. Shroff, P. D. Yang, and J. Liphardt. Optical Trapping and Integration of Semiconductor Nanowire Assemblies in Water. *Nature Materials*, 5(2):97–101, 2006.

[15] L. P. Neukirch, J. Gieseler, R. Quidant, Novotny L., and A. N. Vamivakas. Observation of Nitrogen Vacancy Photoluminescence from an Optically Levitated Nanodiamond. *Optical Letters*, 38(16):2976–2979, 2013.

[16] C. Xie, M. A. Dinno, and Y. Li. Near-Infrared Raman Spectroscopy of Single Optically Trapped Biological Cells. *Optical Letters*, 27(4):249–251, 2002.

[17] Lucien P Ghislain and Watt W Webb. Scanning-Force Microscope Based on an Optical Trap. *Opt. Lett.*, 18(19):1678–1680, 1993.

[18] R. N. C. Pfeifer, T. A. Nieminen, N. R. Heckenberg, and H. Rubinsztein-Dunlop. Colloquium: Momentum of an Electromagnetic Wave in Dielectric Media. *Reviews of Modern Physics*, 79(4):1197, 2007.

[19] B. T. Draine and P. J. Flatau. Discrete-Dipole Approximation for Scattering Calculations. *Journal of the Optical Society of America A*, 11(4):1491–1499, 1994.

[20] T. A. Nieminen, H. Rubinsztein-Dunlop, and N. R. Heckenberg. Calculation and Optical Measurement of Laser Trapping Forces on Non-Spherical Particles. *Journal of Quantitative Spectroscopy and Radiative Transfer*, 70(4):627–637, 2001.

[21] J. P. Gordon. Radiation Forces and Momenta in Dielectric Media. *Physical Review A*, 8(1):14, 1973.

[22] B. T. Draine. The Discrete-Dipole Approximation and its Application to Interstellar Graphite Grains. *The Astrophysical Journal*, 333:848–872, 1988.

[23] O. M. Maragò, P. H. Jones, P. G. Gucciardi, G. Volpe, and A. C. Ferrari. Optical Trapping and Manipulation of Nanostructures. *Nature Nanotechnology*, 8(11):807–819, 2013.

[24] K. Berg-Sorensen and H. Flyvbjerg. Power Spectrum Analysis for Optical Tweezers. *Review of Scientific Instruments*, 75(3):594–612, 2004.

[25] A. Einstein. On the Motion–Required by the Molecular Kinetic Theory of Heat–of Small Particles Suspended in a Stationary Liquid. *Annalen der Physik*, 17(8):549–560, 1905.

[26] K. C. Neuman and S. M. Block. Optical Trapping. *Review of Scientific Instruments*, 75(9):2787–2809, 2004.

[27] E. Fällman and O. Axner. Influence of a Glass-Water Interface on the On-Axis Trapping of Micrometer-Sized Spherical Objects by Optical Tweezers. *Applied Optics*, 42(19):3915–3926, 2003.

[28] B. Roy, S. K. Bera, and A. Banerjee. Simultaneous Detection of Rotational and Translational Motion in Optical Tweezers by Measurement of Backscattered Intensity. *Optics Letters*, 39(11):3316–3319, 2014.

[29] O. M. Marago, P. H. Jones, F. Bonaccorso, V. Scardaci, P. G. Gucciardi, A. G. Rozhin, and A. C. Ferrari. Femtonewton Force Sensing with Optically Trapped Nanotubes. *Nano Letters*, 8(10):3211–3216, 2008.

[30] A. Irrera, P. Artoni, R. Saija, P. G. Gucciardi, M. A. Iatì, F. Borghese, P. Denti, F. Iacona, F. Priolo, and O. M. Marago. Size-Scaling in Optical Trapping of Silicon Nanowires. *Nano Lett.*, 11(11):4879–4884, 2011.

[31] P. B. Roder, B. E. Smith, E. J. Davis, and P. J. Pauzauskie. Photothermal Heating of Nanowires. *The Journal of Physical Chemistry C*, 118(3):1407–1416, 2014.

[32] M. Sarshar, W. T. Wong, and B. Anvari. Comparative Study of Methods to Calibrate the Stiffness of a Single-Beam Gradient-Force Optical Tweezers Over Various Laser Trapping Powers. *Journal of Biomedical Optics*, 19(11):115001–115001, 2014.

[33] S. F. Tolić-Nørrelykke, E. Schäffer, J. Howard, F. S. Pavone, F. Jülicher, and H. Flyvbjerg. Calibration of Optical Tweezers with Positional Detection in the Back Focal Plane. *Review of Scientific Instruments*, 77(10):103101, 2006.

[34] M. J. Sailor and J. Park. Hybrid Nanoparticles for Detection and Treatment of Cancer. *Advanced Materials*, 24(28):3779–3802, 2012.

[35] Z. Zhang, J. Wang, and C. Chen. Near-Infrared Light-Mediated Nanoplatforms for Cancer Thermo-Chemotherapy and Optical Imaging. *Advanced Materials*, 25(28):3869–3880, 2013.

[36] S. Berciaud, L. Cognet, G. A. Blab, and B. Lounis. Photothermal Heterodyne Imaging of Individual Nonfluorescent Nanoclusters and Nanocrystals. *Physical Review Letters*, 93(25):257402, 2004.

[37] E. C. Dreaden, A. M. Alkilany, X. Huang, C. J. Murphy, and M. A. El-Sayed. The Golden Age: Gold Nanoparticles for Biomedicine. *Chemical Society Reviews*, 41(7):2740–2779, 2012.

[38] E. J. G. Peterman, F. Gittes, and C. F. Schmidt. Laser-Induced Heating in Optical Traps. *Biophysical Journal*, 84(2):1308–1316, 2003.

[39] J. Millen, T. Deesuwan, P. Barker, and J. Anders. Nanoscale Temperature Measurements Using Non-Equilibrium Brownian Dynamics of a Levitated Nanosphere. *Nature Nanotechnology*, 9(6):425–429, 2014.

[40] A. Kyrsting, P. M. Bendix, D. G. Stamou, and L. B. Oddershede. Heat Profiling of Three-Dimensionally Optically Trapped Gold Nanoparticles Using Vesicle Cargo Release. *Nano Letters*, 11(2):888–892, 2010.

[41] M. Iwaki, A. H. Iwane, K. Ikezaki, and T. Yanagida. Local Heat Activation of Single Myosins Based on Optical Trapping of Gold Nanoparticles. *Nano Letters*, 15(4):2456–2461, 2015.

[42] J. Kestin, M. Sokolov, and W. A. Wakeham. Viscosity of Liquid Water in the Range 8C to 150C. *Journal of Physical and Chemical Reference Data*, 7(3):941–948, 1978.

[43] R. C. Hardy and R. L. Cottington. Viscosity of Deuterium Oxide and Water in the Range of 5 to 125C. *Journal of Research of the National Bureau of Standards*, 42:573–578, 1949.

[44] M. Capitanio, G. Romano, R. Ballerini, M. Giuntini, F. S. Pavone, D. Dunlap, and L. Finzi. Calibration of Optical Tweezers with Differential Interference Contrast Signals. *Review of Scientific Instruments*, 73(4):1687–1696, 2002.

[45] P. Haro-González, B. Del Rosal, L. M. Maestro, E. M. Rodríguez, R. Naccache, J. A. Capobianco, K. Dholakia, J. G. Solé, and D. Jaque. Optical Trapping of $NaYF_4$: Er^{3+}, Yb^{3+} Upconverting Fluorescent Nanoparticles. *Nanoscale*, 5(24):12192–12199, 2013.

[46] J. H. Bunton, J. D. Olson, D. R. Lenz, and T. F. Kelly. Advances in Pulsed-Laser Atom Probe: Instrument and Specimen Design for Optimum Performance. *Microscopy and Microanalysis*, 13(06):418–427, 2007.

[47] D. E. Perea, J. L. Lensch, S. J. May, B. W. Wessels, and L. J. Lauhon. Composition Analysis of Single Semiconductor Nanowires Using Pulsed-Laser Atom Probe Tomography. *Applied Physics A*, 85(3):271–275, 2006.

[48] D. E. Perea, E. Wijaya, J. L. Lensch-Falk, E. R. Hemesath, and L. J. Lauhon. Tomographic Analysis of Dilute Impurities in Semiconductor Nanostructures. *Journal of Solid State Chemistry*, 181(7):1642–1649, 2008.

[49] B. P. Gorman, A. G. Norman, and Y. Yan. Atom Probe Analysis of III-V and Si-Based Semiconductor Photovoltaic Structures. *Microscopy and Microanalysis*, 13(06):493–502, 2007.

[50] D. N. Seidman and R. M. Scanlan. On the Heating of a Field Ion Microscope Specimen. *Philosophical Magazine*, 23(186):1429–1437, 1971.

[51] H. F. Liu and T. T. Tsong. Numerical Calculation of the Temperature Evolution and Profile of the Field Ion Emitter in the Pulsed-Laser Time-of-Flight Atom Probe. *Review of Scientific Instruments*, 55(11):1779–1784, 1984.

[52] H. F. Liu, H. M. Liu, and T. T. Tsong. Numerical Calculation of the Temperature Distribution and Evolution of the Field-Ion Emitter Under Pulsed and Continuous-Wave Laser Irradiation. *Journal of Applied Physics*, 59(4):1334–1340, 1986.

[53] F. Vurpillot, B. Gault, A. Vella, M. Bouet, and B. Deconihout. Estimation of the Cooling Times for a Metallic Tip Under Laser Illumination. *Applied Physics Letters*, 88(9):094105, 2006.

[54] S. G. Volz and G. Chen. Molecular Dynamics Simulation of Thermal Conductivity of Silicon Nanowires. *Applied Physics Letters*, 75(14):2056–2058, 1999.

[55] D. Li, Y. Wu, P. Kim, L. Shi, P. Yang, and A. Majumdar. Thermal Conductivity of Individual Silicon Nanowires. *Applied Physics Letters*, 83(14):2934–2936, 2003.

[56] J. Bogdanowicz, M. Gilbert, N. Innocenti, S. Koelling, B. Vanderheyden, and W. Vandervorst. Light Absorption in Conical Silicon Particles. *Optics Express*, 21(3):3891–3896, 2013.

[57] J. Bogdanowicz, M. Gilbert, S. Koelling, and W. Vandervorst. Impact of the Apex of an Elongated Dielectric Tip Upon its Light Absorption Properties. *Applied Surface Science*, 302:223–225, 2014.

[58] E. D. Palik. *Handbook of Optical Constants of Solids*. Elsevier, New York, 1998.

[59] P. Flubacher, A. J. Leadbetter, and J. A. Morrison. The Heat Capacity of Pure Silicon and Germanium and Properties of Their Vibrational Frequency Spectra. *Philosophical Magazine*, 4(39):273–294, 1959.

[60] S. Koelling, N. Innocenti, J. Bogdanowicz, and W. Vandervorst. Optimal Laser Positioning for Laser-Assisted Atom Probe Tomography. *Ultramicroscopy*, 132:70–74, 2013.

[61] T. F. Kelly, A. Vella, J. H. Bunton, J. Houard, E. P. Silaeva, J. Bogdanowicz, and W. Vandervorst. Laser Pulsing of Field Evaporation in Atom Probe Tomography. *Current Opinion in Solid State and Materials Science*, 18(2):81–89, 2014.

[62] D. G. Cahill, M. Katiyar, and J. R. Abelson. Thermal Conductivity of a-Si:H Thin Films. *Physical Review B*, 50(9):6077, 1994.

[63] B. L. Zink, R. Pietri, and F. Hellman. Thermal Conductivity and Specific Heat of Thin-Film Amorphous Silicon. *Physical Review Letters*, 96(5):055902, 2006.

[64] D. G. Cahill, H. E. Fischer, T. Klitsner, E. T. Swartz, and R. O. Pohl. Thermal

Conductivity of Thin Films: Measurements and Understanding. *Journal of Vacuum Science and Technology A*, 7(3):1259–1266, 1989.

[65] G. Pompe and E. Hegenbarth. Thermal Conductivity of Amorphous Si at Low Temperatures. *Physica Status Solidi B*, 147(1):103–108, 1988.

[66] J. B. In, B. Xiang, D. J. Hwang, S. Ryu, E. Kim, J. Yoo, O. Dubon, A. M. Minor, and C. P. Grigoropoulos. Generation of Single-Crystalline Domain in Nano-Scale Silicon Pillars by Near-Field Short Pulsed Laser. *Applied Physics A*, 114(1):277–285, 2014.

[67] A. S. McLeod, P. Kelly, M. D. Goldflam, Z. Gainsforth, A. J. Westphal, G. Dominguez, M. H. Thiemens, M. M. Fogler, and D. N. Basov. Model for Quantitative Tip-Enhanced Spectroscopy and the Extraction of Nanoscale-Resolved Optical Constants. *Physical Review B*, 90(8):085136, 2014.

[68] S. Berweger and M. B. Raschke. Signal Limitations in Tip-Enhanced Raman Scattering: The Challenge to Become a Routine Analytical Technique. *Analytical and Bioanalytical Chemistry*, 396(1):115–123, 2010.

[69] S. W. Churchill and H. S. Chu. Correlating Equations for Laminar and Turbulent Free Convection from a Horizontal Cylinder. *International Journal of Heat and Mass Transfer*, 18(9):1049–1053, 1975.

[70] William Henry McAdams and William H McAdams. *Heat transmission*, volume 3. McGraw-Hill New York, 1954.

[71] P. Davies and M. J. Fisher. Heat Transfer from Electrically Heated Cylinders. *Proceedings of the Royal Society of London Series A*, 280(1383):486–527, 1964.

[72] J. P. Holman. *Heat Transfer*. McGraw-Hill:New York, 1981.

[73] H. C. Van De Hulst. *Light Scattering by Small Particles*. Wiley and Sons:New York, 1957.

[74] M. Kerker. *The Scattering of Light, and Other Electromagnetic Radiation*. Academic Press:New York, 1969.

[75] C. F. Bohren and D. R. Huffman. *Absorption and Scattering of Light by Small Particles*. Wiley and Sons:New York, 1983.

[76] K. S. Yee. Numerical Solution of Initial Boundary Value Problems Involving Maxwell's Equations in Isotropic Media. *IEEE Transactions on Antennas and Propagation*, 14(3):302–307, 1966.

[77] A. F. Oskooi, D. Roundy, M. Ibanescu, P. Bermel, J. D. Joannopoulos, and S. G. Johnson. MEEP: A Flexible Free-Software Package for Electromagnetic Simulations by the FDTD Method. *Computer Physics Communications*, 181(3):687–702, 2010.

[78] R. Ruppin. Electromagnetic Energy Inside an Irradiated Cylinder. *Journal of the Optical Society of America A*, 15(7):1891–1895, 1998.

[79] C. H. Liu, C. Y. Soong, W. K. Li, and P. Y. Tzeng. Internal Electric Field Distribution Within a Micro-Cylinder-Shaped Particle Suspended in an Absorbing Gaseous Medium. *Journal of Quantitative Spectroscopy and Radiative Transfer*, 111(3):483–491, 2010.

[80] T. M. Allen, M. F. Buehler, and E. J. Davis. Radiometric Effects on Absorbing Microspheres. *Journal of Colloid and Interface Science*, 142(2):343–356, 1991.

[81] A. B. Pluchino, S. S. Goldberg, J. M. Dowling, and C. M. Randall. Refractive-Index Measurements of Single Micron-Sized Carbon Particles. *Applied Optics*, 19:3370–3372, 1980.

[82] D. Ramos, E. Gil-Santos, V. Pini, J. M. Llorens, M. Fernández-Regúlez, Á. San Paulo, M. Calleja, and J. Tamayo. Optomechanics with Silicon Nanowires by Harnessing Confined Electromagnetic Modes. *Nano Letters*, 12(2):932–937, 2012.

[83] Y. Qu, H. Zhou, and X. Duan. Porous Silicon Nanowires. *Nanoscale*, 3(10):4060–4068, 2011.

[84] C. Ferrero, M. Servidori, D. Thiaudière, S. Milita, S. Lequien, S. Sama, S. Setzu, and T. H. Metzger. Depth Profiling of the Lateral Pore Size and Correlation Distance in Thin Porous Silicon Layers by Grazing Incidence Small Angle X-Ray Scattering. *Journal of The Electrochemical Society*, 150(7):366–370, 2003.

[85] A. Garahan, L. Pilon, J. Yin, and I. Saxena. Effective Optical Properties of Absorbing Nanoporous and Nanocomposite Thin Films. *Journal of Applied Physics*, 101(1):014320, 2007.

[86] J. K. Carson, S. J. Lovatt, D. J. Tanner, and A. C. Cleland. Thermal Conductivity Bounds for Isotropic, Porous Materials. *International Journal of Heat and Mass Transfer*, 48(11):2150–2158, 2005.

[87] M. A. Yurkin and A. G. Hoekstra. The Discrete Dipole Approximation: An Overview and Recent Developments. *Journal of Quantitative Spectroscopy and Radiative Transfer*, 106(1-3):558–589, 2007.

[88] T. C. Bond and R. W. Bergstrom. Light Absorption by Carbonaceous Particles: An Investigative Review. *Aerosol Science and Technology*, 40(1):27–67, 2006.

[89] P. J. Pauzauskie, J. C. Crowhurst, M. A. Worsley, T. A. Laurence, A. L. D. Kilcoyne, Y. Wang, T. M. Willey, K. S. Visbeck, S. C. Fakra, W. J. Evans, J. M. Zaug, and J. H. Satcher. Synthesis and Characterization of a Nanocrystalline Diamond Aerogel. *The Proceedings of the National Academy of Sciences of the United States of America*, 108(21):8550–8553, 2011.

[90] Z. Huang, N. Geyer, P. Werner, J. de Boor, and U. Gösele. Metal-Assisted Chemical Etching of Silicon: A Review. *Advanced Materials*, 23(2):285–308, 2010.

[91] J. P. Biersack and L. G. Haggmark. A Monte-Carlo Computer-Program for the Transport of Energetic Ions in Amorphous Targets. *Nuclear Instruments and Methods in Physics Research*, 174(1):257–269, 1980.

[92] D. Rings, R. Schachoff, M. Selmke, F. Cichos, and K. Kroy. Hot Brownian Motion. *Physical Review Letters*, 105(9):090604, 2010.

[93] D. Chakraborty, M. V. Gnann, D. Rings, J. Glaser, F. Otto, F. Cichos, and K. Kroy. Generalised Einstein Relation for Hot Brownian Motion. *Europhysics Letters*, 96(6):60009, 2011.

[94] G. Falasco, M. V. Gnann, D. Rings, and K. Kroy. Effective Temperatures of Hot Brownian Motion. *Physical Review E*, 90(3):032131, 2014.

[95] D. Rings, D. Chakraborty, and K. Kroy. Rotational Hot Brownian Motion. *New Journal of Physics*, 14(5):053012, 2012.

[96] P. J. Reece, W. J. Toe, F. Wang, S. Paiman, Q. Gao, H. H. Tan, and C. Jagadish. Characterization of Semiconductor Nanowires Using Optical Tweezers. *Nano Letters*, 11(6):2375–2381, 2011.

[97] D. G. Cahill, W. K. Ford, K. E. Goodson, G. D. Mahan, A. Majumdar, H. J. Maris, R. Merlin, and S. R. Phillpot. Nanoscale Thermal Transport. *Journal of Applied Physics*, 93(2):793–818, 2003.

[98] G. Kucsko, P. C. Maurer, N. Y. Yao, M. Kubo, H. J. Noh, P. K. Lo, H. Park, and M. D. Lukin. Nanometre-Scale Thermometry in a Living Cell. *Nature*, 500(7460):54–58, 2013.

[99] B. E. Smith, P. B. Roder, X. Zhou, and P. J. Pauzauskie. Nanoscale Materials for Hyperthermal Theranostics. *Nanoscale*, 7(16):7115–7126, 2015.

[100] J. T. Robinson, K. Welsher, S. M. Tabakman, S. P. Sherlock, H. Wang, R. Luong,

and H. Dai. High Performance in vivo Near-IR (¿ 1 μm) Imaging and Photothermal Cancer Therapy with Carbon Nanotubes. *Nano Research*, 3(11):779–793, 2010.

[101] C. Liang, S. Diao, C. Wang, H. Gong, T. Liu, G. Hong, X. Shi, H. Dai, and Z. Liu. Tumor Metastasis Inhibition by Imaging-Guided Photothermal Therapy with Single-Walled Carbon Nanotubes. *Advanced Materials*, 26(32):5646–5652, 2014.

[102] J. K. Young, E. R. Figueroa, and R. A. Drezek. Tunable Nanostructures as Photothermal Theranostic Agents. *Annals of Biomedical Engineering*, 40(2):438–459, 2012.

[103] E. Boisselier and D. Astruc. Gold Nanoparticles in Nanomedicine: Preparations, Imaging, Diagnostics, Therapies and Toxicity. *Chemical Society Reviews*, 38(6):1759–1782, 2009.

[104] E. B. Dickerson, E. C. Dreaden, X. Huang, I. H. El-Sayed, H. Chu, S. Pushpanketh, J. F. McDonald, and M. A. El-Sayed. Gold Nanorod Assisted Near-Infrared Plasmonic Photothermal Therapy (PPTT) of Squamous Cell Carcinoma in Mice. *Cancer Letters*, 269(1):57–66, 2008.

[105] P. K. Jain, I. H. El-Sayed, and M. A. El-Sayed. Au Nanoparticles Target Cancer. *Nano Today*, 2(1):18–29, 2007.

[106] L. C. Kennedy, L. R. Bickford, N. A. Lewinski, A. J. Coughlin, Y. Hu, E. S. Day, J. L. West, and R. A. Drezek. A New Era for Cancer Treatment: Gold-Nanoparticle-Mediated Thermal Therapies. *Small*, 7(2):169–183, 2011.

[107] C. Loo, A. Lowery, N. Halas, J. West, and R. Drezek. Immunotargeted Nanoshells for Integrated Cancer Imaging and Therapy. *Nano Letters*, 5(4):709–711, 2005.

[108] P. K. Jain, K. S. Lee, I. H. El-Sayed, and M. A. El-Sayed. Calculated Absorption and Scattering Properties of Gold Nanoparticles of Different Size, Shape, and Composition: Applications in Biological Imaging and Biomedicine. *The Journal of Physical Chemistry B*, 110(14):7238–7248, 2006.

[109] N. R. Jana, L. Gearheart, and C. J. Murphy. Seed-Mediated Growth Approach for Shape-Controlled Synthesis of Spheroidal and Rod-Like Gold Nanoparticles Using a Surfactant Template. *Advanced Materials*, 13(18):1389, 2001.

[110] S. Link and M. A. El-Sayed. Shape and Size Dependence of Radiative, Non-Radiative and Photothermal Properties of Gold Nanocrystals. *International Reviews in Physical Chemistry*, 19(3):409–453, 2000.

[111] I. H. El-Sayed, X. Huang, and M. A. El-Sayed. Selective Laser Photo-Thermal Therapy of Epithelial Carcinoma Using anti-EGFR Antibody Conjugated Gold Nanoparticles. *Cancer Letters*, 239(1):129–135, 2006.

[112] R. S. Norman, J. W. Stone, A. Gole, C. J. Murphy, and T. L. Sabo-Attwood. Targeted Photothermal Lysis of the Pathogenic Bacteria, Pseudomonas Aeruginosa, with Gold Nanorods. *Nano Letters*, 8(1):302–306, 2008.

[113] L. Tong, Q. Wei, A. Wei, and J. Cheng. Gold Nanorods as Contrast Agents for Biological Imaging: Optical Properties, Surface Conjugation and Photothermal Effects. *Photochemistry and Photobiology*, 85(1):21–32, 2009.

[114] S. E. Skrabalak, J. Chen, L. Au, X. Lu, X. Li, and Y. Xia. Gold Nanocages for Biomedical Applications. *Advanced Materials*, 19(20):3177–3184, 2007.

[115] T. S. Troutman, J. K. Barton, and M. Romanowski. Biodegradable Plasmon Resonant Nanoshells. *Advanced Materials*, 20(13):2604–2608, 2008.

[116] C. Chen and D. Chen. Preparation of LaB_6 Nanoparticles as a Novel and Effective Near-Infrared Photothermal Conversion Material. *Chemical Engineering Journal*, 180:337–342, 2012.

[117] Z. Chen, Q. Wang, H. Wang, L. Zhang, G. Song, L. Song, J. Hu, H. Wang, J. Liu, and M. Zhu. Ultrathin PEGylated $W_{18}O_{49}$ Nanowires as a New 980 nm-Laser-Driven

Photothermal Agent for Efficient Ablation of Cancer Cells In Vivo. *Advanced Materials*, 25(14):2095–2100, 2013.

[118] C. M. Hessel, V. Pattani, M. Rasch, M. G. Panthani, B. Koo, J. W. Tunnell, and B. A. Korgel. Copper Selenide Nanocrystals for Photothermal Therapy. *Nano Letters*, 11(6):2560–2566, 2011.

[119] T. N. Lambert, N. L. Andrews, H. Gerung, T. J. Boyle, J. M. Oliver, B. S. Wilson, and S. M. Han. Water-Soluble Germanium(0) Nanocrystals: Cell Recognition and Near-Infrared Photothermal Conversion Properties. *Small*, 3(4):691–699, 2007.

[120] W. Li, R. Zamani, P. Rivera Gil, B. Pelaz, M. Ibáñez, D. Cadavid, A. Shavel, R. A. Alvarez-Puebla, W. J. Parak, and J. Arbiol. CuTe Nanocrystals: Shape and Size Control, Plasmonic Properties, and use as SERS Probes and Photothermal Agents. *Journal of the American Chemical Society*, 135(19):7098–7101, 2013.

[121] G. Song, Q. Wang, Y. Wang, G. Lv, C. Li, R. Zou, Z. Chen, Z. Qin, K. Huo, and R. Hu. A Low-Toxic Multifunctional Nanoplatform Based on Cu_9S_5 $mSiO_2$ Core-Shell Nanocomposites: Combining Photothermal-and Chemotherapies with Infrared Thermal Imaging for Cancer Treatment. *Advanced Functional Materials*, 23(35):4281–4292, 2013.

[122] J. A. Faucheaux, A. L. D. Stanton, and P. K. Jain. Plasmon Resonances of Semiconductor Nanocrystals: Physical Principles and New Opportunities. *The Journal of Physical Chemistry Letters*, 5(6):976–985, 2014.

[123] N. Wang, B. D. Yao, Y. F. Chan, and X. Y. Zhang. Enhanced Photothermal Effect in Si Nanowires. *Nano Letters*, 3(4):475–477, 2003.

[124] A. P. Mann, T. Tanaka, A. Somasunderam, X. Liu, D. G. Gorenstein, and M. Ferrari. E-Selectin-Targeted Porous Silicon Particle for Nanoparticle Delivery to the Bone Marrow. *Advanced Materials*, 23(36):278–282, 2011.

[125] J. Park, L. Gu, G. Von Maltzahn, E. Ruoslahti, S. N. Bhatia, and M. J. Sailor. Biodegradable Luminescent Porous Silicon Nanoparticles for in Vivo Applications. *Nature Materials*, 8(4):331–336, 2009.

[126] B. E. Smith, P. B. Roder, J. L. Hanson, S. Manandhar, A. Devaraj, D. E. Perea, W. Kim, A. L. D. Kilcoyne, and P. J. Pauzauskie. Singlet-Oxygen Generation from Individual Semiconducting and Metallic Nanostructures During Near-Infrared Laser Trapping. *ACS Photonics*, 2(4):559–564, 2015.

[127] X. Li and P. W. Bohn. Metal-Assisted Chemical Etching in HF/H_2O_2 Produces Porous Silicon. *Applied Physics Letters*, 77(16):2572–2574, 2000.

[128] N. Noguchi and I. Suemune. Luminescent Porous Silicon Synthesized by Visible Light Irradiation. *Applied Physics Letters*, 62(12):1429–1431, 1993.

[129] L. Lin, S. Guo, X. Sun, J. Feng, and Y. Wang. Synthesis and Photoluminescence Properties of Porous Silicon Nanowire Arrays. *Nanoscale Research Letters*, 5(11):1822–1828, 2010.

[130] E. J. Anglin, L. Cheng, W. R. Freeman, and M. J. Sailor. Porous Silicon in Drug Delivery Devices and Materials. *Advanced Drug Delivery Reviews*, 60(11):1266–1277, 2008.

[131] J. Salonen, L. Laitinen, A. M. Kaukonen, J. Tuura, M. Björkqvist, T. Heikkilä, K. Vähä-Heikkilä, J. Hirvonen, and V. P. Lehto. Mesoporous Silicon Microparticles for Oral Drug Delivery: Loading and Release of Five Model Drugs. *Journal of Controlled Release*, 108(2):362–374, 2005.

[132] W. Sun, J. E. Puzas, T. J. Sheu, X. Liu, and P. M. Fauchet. Nano-to Microscale Porous Silicon as a Cell Interface for Bone-Tissue Engineering. *Advanced Materials*, 19(7):921–924, 2007.

[133] L. Vaccari, D. Canton, N. Zaffaroni, R. Villa, M. Tormen, and E. di Fabrizio. Porous Silicon as Drug Carrier for Controlled Delivery of Doxorubicin Anticancer Agent. *Microelectronic Engineering*, 83(4):1598–1601, 2006.

[134] S. Chan and P. M. Fauchet. Tunable, Narrow, and Directional Luminescence from Porous Silicon Light Emitting Devices. *Applied Physics Letters*, 75(2):274–276, 1999.

[135] A. G. Cullis, L. T. Canham, and P. D. J. Calcott. The Structural and Luminescence Properties of Porous Silicon. *Journal of Applied Physics*, 82(3):909–965, 1997.

[136] S. M. Prokes and W. E. Carlos. Oxygen Defect Center Red Room Temperature Photoluminescence from Freshly Etched and Oxidized Porous Silicon. *Journal of Applied Physics*, 78(4):2671–2674, 1995.

[137] J. A. Dickson and B. E. Oswald. The Sensitivity of a Malignant Cell Line to Hyperthermia (42C) at Low Intracellular pH. *British Journal of Cancer*, 34(3):262, 1976.

[138] J. C. Y. Kah, R. C. Y. Wan, K. Y. Wong, S. Mhaisalkar, C. J. R. Sheppard, and M. Olivo. Combinatorial Treatment of Photothermal Therapy Using Gold Nanoshells with Conventional Photodynamic Therapy to Improve Treatment Efficacy: an in Vitro Study. *Lasers in Surgery and Medicine*, 40(8):584–589, 2008.

[139] Y. Liu, D. K. Cheng, G. J. Sonek, M. W. Berns, C. F. Chapman, and B. J. Tromberg. Evidence for Localized Cell Heating Induced by Infrared Optical Tweezers. *Biophysical Journal*, 68(5):2137, 1995.

[140] H. Mao, J. R. Arias-Gonzalez, S. B. Smith, I. Tinoco, and C. Bustamante. Temperature Control Methods in a Laser Tweezers System. *Biophysical Bournal*, 89(2):1308–1316, 2005.

[141] P. A. Quinto-Su. A Microscopic Steam Engine Implemented in an Optical Tweezer. *Nature Communications*, 5, 2014.

[142] H. Rubinsztein-Dunlop, T. A. Nieminen, M. E. J. Friese, and N. R. Heckenberg. Optical Trapping of Absorbing Particles. *Advances in Quantum Chemistry*, 30:469–492, 1998.

[143] Y. Seol, A. E. Carpenter, and T. T. Perkins. Gold Nanoparticles: Enhanced Optical Trapping and Sensitivity Coupled with Significant Heating. *Optics Letters*, 31(16):2429–2431, 2006.

[144] D. B. Williams and C. B. Carter. The Transmission Electron Microscope. In *Transmission Electron Microscopy*. Springer, 2009.

[145] X. Huang, F. Ninio, L. J. Brown, and S. Prawer. Raman Scattering Studies of Surface Modification in 1.5 MeV Si-Implanted Silicon. *Journal of Applied Physics*, 77(11):5910–5915, 1995.

[146] K. P. Jain, A. K. Shukla, R. Ashokan, S. C. Abbi, and M. Balkanski. Raman Scattering from Ion-Implanted Silicon. *Physical Review B*, 32(10):6688, 1985.

[147] J. Lavrentiev, V.and Vacik, V. Vorlicek, and V. Vosecek. Raman Scattering in Silicon Disordered by Gold Ion Implantation. *Physica Status Solidi B*, 247(8):2022–2026, 2010.

[148] D. V. Lang, H. G. Grimmeiss, E. Meijer, and M. Jaros. Complex Nature of Gold-Related Deep Levels in Silicon. *Physical Review B*, 22(8):3917, 1980.

[149] D. K. Venkatachalam, D. K. Sood, and S. K. Bhargava. Spiral Patterns of Gold Nanoclusters in Silicon (100) Produced by Metal Vapour Vacuum Arc Implantation of Gold Ions. *Nanotechnology*, 19(1):015605, 2008.

[150] X. T. Wang, W. S. Shi, G. W. She, L. X. Mu, and S. T. Lee. High-Performance Surface-Enhanced Raman Scattering Sensors Based on Ag Nanoparticles-Coated Si Nanowire Arrays for Quantitative Detection of Pesticides. *Applied Physics Letters*, 96(5):053104, 2010.

[151] P. Pringsheim. Two Observations About the Difference Between Luminescence and Thermal Radiation. *Zeitschrift für Physik*, 57:739–746, 1929.

[152] R. I. Epstein, M. I. Buchwald, B. C. Edwards, T. R. Gosnell, and C. E. Mungan. Observation of Laser-Induced Fluorescent Cooling of a Solid. *Nature*, 377(6549):500–503, 1995.

[153] E. S. d. L. Filho, G. Nemova, S. Loranger, and R. Kashyap. Laser-Induced Cooling of a Yb:YAG Crystal in Air at Atmospheric Pressure. *Optics Express*, 21(21):24711–24720, 2013.

[154] J. Zhang, D. Li, R. Chen, and Q. Xiong. Laser Cooling of a Semiconductor by 40 kelvin. *Nature*, 493(7433):504–508, 2013.

[155] S. D. Melgaard, D. V. Seletskiy, A. Di Lieto, M. Tonelli, and M. Sheik-Bahae. Optical Refrigeration to 119K, below National Institute of Standards and Technology Cryogenic Temperature. *Optics Letters*, 38(9):1588–1590, 2013.

[156] Y. Arita, M. Mazilu, and K. Dholakia. Laser-Induced Rotation and Cooling of a Trapped Microgyroscope in Vacuum. *Nature Communications*, 4, 2013.

[157] X. L. Ruan and M. Kaviany. Enhanced Laser Cooling of Rare-Earth-Ion-Doped Nanocrystalline Powders. *Physical Review B*, 73(15):155422, 2006.

[158] Y. Y. Kalisky. *The Physics and Engineering of Solid State Lasers*, volume 71. SPIE Press, 2006.

[159] F. Mark. *Optical Properties of Solids*. Oxford University Press:New York, 2001.

[160] Markus P. Hehlen. Crystal-Field Effects in Fluoride Crystals for Optical Refrigeration. volume 7614, pages 761404–761404–12, 2010.

[161] L. Landau. On The Thermodynamics of Photoluminescence. *Journal of Physics (Moscow)*, 10:503–506, 1946.

[162] F. Wang, D. Banerjee, X. Liu, Y.and Chen, and X. Liu. Upconversion Nanoparticles in Biological Labeling, Imaging, and Therapy. *Analyst*, 135(8):1839–1854, 2010.

[163] E. J. McLaurin, L. R. Bradshaw, and D. R. Gamelin. Dual-Emitting Nanoscale Temperature Sensors. *Chemistry of Materials*, 25(8):1283–1292, 2013.

[164] D. V. Seletskiy, S. D. Melgaard, S. Bigotta, A. Di Lieto, M. Tonelli, and M. Sheik-Bahae. Laser Cooling of Solids to Cryogenic Temperatures. *Nature Photonics*, 4(3):161–164, 2010.

[165] C. Lu, W. Huang, Y. Ni, and Z. Xu. Hydrothermal Synthesis and Luminescence Properties of Octahedral $LiYbF_4$:Er^{3+} Microcrystals. *Materials Research Bulletin*, 46(2):216–221, 2011.

[166] D. Li, M. H. Nielsen, J. R. I. Lee, C. Frandsen, J. F. Banfield, and J. J. De Yoreo. Direction-Specific Interactions Control Crystal Growth by Oriented Attachment. *Science*, 336(6084):1014–1018, 2012.

[167] F. Vetrone, R. Naccache, A. Zamarron, A. Juarranz de la Fuente, F. Sanz-Rodríguez, L. Martinez Maestro, E. Martín Rodriguez, D. Jaque, J. García Solé, and J. A. Capobianco. Temperature Sensing using Fluorescent Nanothermometers. *ACS Nano*, 4(6):3254–3258, 2010.

[168] G. Dong, X. Zhang, and L. Li. Energy Transfer Enhanced Laser Cooling in Ho^{3+} and Tm^{3+}-Codoped Lithium Yttrium Fluoride. *Journal of the Optical Society of America B*, 30(4):939–944, 2013.

[169] P. M. Hinderliter, K. R. Minard, G. Orr, W. B. Chrisler, B. D. Thrall, J. G. Pounds, and J. G. Teeguarden. ISDD: A Computational Model of Particle Sedimentation, Diffusion and Target Cell Dosimetry for in Vitro Toxicity Studies. *Particle and Fibre Toxicology*, 7(1):36, 2010.

[170] A. V. Feshchenko, J. V. Koski, and J. P. Pekola. Experimental Realization of a Coulomb Blockade Refrigerator. *Physical Review B*, 90(20):201407, 2014.

[171] I. Chowdhury, R. Prasher, K. Lofgreen, G. Chrysler, S. Narasimhan, R. Mahajan, D. Koester, R. Alley, and R. Venkatasubramanian. On-Chip Cooling by Superlattice-Based Thin-Film Thermoelectrics. *Nature Nanotechnology*, 4(4):235–238, 2009.

[172] J. Flipse, F. L. Bakker, A. Slachter, F. K. Dejene, and B. J. Van Wees. Direct Observation of the Spin-Dependent Peltier Effect. *Nature Nanotechnology*, 7(3):166–168, 2012.

[173] W. Bogaerts, M. Fiers, and P. Dumon. Design Challenges in Silicon Photonics. *IEEE Journal of Selected Topics in Quantum Electronics*, 20(4):1–8, 2014.

[174] C. Vicario, B. Monoszlai, C. Lombosi, A. Mareczko, A. Courjaud, J. A. Fülöp, and C. P. Hauri. Pump Pulse Width and Temperature Effects in Lithium Niobate for Efficient THz Generation. *Optics Letters*, 38(24):5373–5376, 2013.

[175] E. M. Lucchetta, J. H. Lee, L. A. Fu, N. H. Patel, and R. F. Ismagilov. Dynamics of Drosophila Embryonic Patterning Network Perturbed in Space and Time using Microfluidics. *Nature*, 434(7037):1134–1138, 2005.

[176] J. H. Lee, H. Ryu, K. S. Chung, D. Posé, S. Kim, M. Schmid, and J. H. Ahn. Regulation of Temperature-Responsive Flowering by MADS-Box Transcription Factor Repressors. *Science*, 342(6158):628–632, 2013.

[177] H. Huang, S. Delikanli, H. Zeng, D. M. Ferkey, and A. Pralle. Remote Control of Ion Channels and Neurons Through Magnetic-Field Heating of Nanoparticles. *Nature Nanotechnology*, 5(8):602–606, 2010.

[178] C. Li. A Targeted Approach to Cancer Imaging and Therapy. *Nature Materials*, 13(2):110–115, 2014.

[179] C. Zander and K. H. Drexhage. Cooling of a Dye Solution by Anti-Stokes Fluorescence. *Advances in Photochemistry*, 20:59–78, 1995.

[180] J. L. Clark and G. Rumbles. Laser Cooling in the Condensed Phase by Frequency Upconversion. *Physical Review Letters*, 76(12):2037, 1996.

[181] J. L. Clark, P. F. Miller, and G. Rumbles. Red Edge Photophysics of Ethanolic Rhodamine 101 and the Observation of Laser Cooling in the Condensed Phase. *The Journal of Physical Chemistry A*, 102(24):4428–4437, 1998.

[182] C. E. Mungan and T. R. Gosnell. Comment on "Laser Cooling in the Condensed Phase by Frequency Upconversion". *Physical Review Letters*, 77(13):2840–2840, 1996.

[183] G. Rumbles and J. L. Clark. Rumbles and Clark Reply. *Physical Review Letters*, 77(13):2841, 1996.

Appendix A

MATLAB FILES

A.1 Introduction

Over the last five years in the Pauzauskie group, I have managed to write many Matlab scripts for a variety of experiments and applications. It would be unreasonable and unnecessary to include all of the scripts here, but there are two scripts in particular that serve as great references for the work presented in this thesis.

The first script is for simulating the temperature fields in laser-pulsed, tapered nanowires presented in Sec. 3.3. This script serves as a great example because it employs integration of size-dependent parameters, a pulsed-laser, and temperature iteration to find the time-dependent temperature solution. This example can easily be adapted to account for continuous-wave lasers and steady-state solutions for the infinite and finite nanowire cases. The second script is for post-processing voltage data acquired during laser tweezer experiments with the quadrant photodiode in the back focal plane to obtain particle temperatures using hot Brownian motion analysis.

A.2 Pulsed laser heating theory

```
% This code is used to predict temperatures of laser pulsed uniform and
% tapered nanowire that are in vaccuum and supported at its base to a heat
% sink. For this m-file , the size dependence of the thermal conductivity is
% solved for by fitting experimental thermal conductivity data to the
% function k(r) = k0(r/r0)^m.

% Written by Paden Roder
% Pauzauskie NanoOptoMechanical Group
```

```
% University of Washington, Department of Materials Science and Engineering
% Created: 02/18/2015
% Last Updated: 02/09/2015

%% Administrative
clear all
close all
LW = 'linewidth';
MS = 'markersize';

%% Functions
isposint = @(y)(y>=0)&(mod(y,1)==0); % Deterime if num is a positive int.

%% Input simulation parameters
r0 = 15; % Wire tip radius, nm
r0m = r0*10^(-9); % Convert to m
w0 = 849; % Laser focus beam waist, nm
w0m = w0*10^(-9); % Convert to m
thetaD = 4; % Wire taper angle, degrees
theta = thetaD*(pi/180); % Convert to radians
len = 10000; % Wire length, nm
r1 = r0 + len*tan(theta); % Wire base radius, nm
lambda = 532; % Laser wavelength, nm
dens = 2.3290; % Wire density, g/cm3
dens = dens*(10^6); % Convert to g/m3
Tb = 70; % Base temp, K
Tg = 109; % Guess temp for thermal properties, K
AvgT = Tb; % Initialize AvgT to be = Tb, K
Tmin = 50; % Set min temperature for thermal properties, K
Tmax = 300; % Set max temperature for thermal properties, K
fp = 10^4; % Pulse frequency, Hz
wp = 10^(-11); % Pulse width, sec
t0 = 0; % Start pulse time, sec
```

```
t1 = 1/fp; % Start next pulse, sec
td = t1-wp; % Time after pulse (wp) until start of next pulse (t1), sec
EpMin = 2*10^(-11); % Minimum pulse energy, J
EpMax = 10^(-10); % Maximum pulse energy, J
Pmin = EpMin/wp; % Minimum laser power, W
Pmax = EpMax/wp; % Maximum laser power, W
Imin = Pmin*2/(pi*(w0m^2)); % Minimum laser irradiance, W/m^2
Imax = Pmax*2/(pi*(w0m^2)); % Maximum laser irradiance, W/m^2
I0 = Imin; % Starting irradiance
numEigs = 30; % Number of eigenvalues wanted. Typically ~> 25

%% Import Specific Heat (Cp) Experimental Data
% Data has 2 columns: Col1 = Temperature (K), Col2 = Cp (J/g.K)
CP = load('CpSiTempDepend.txt'); % Silicon data
tCp = CP(:,1); % temperature of Cp data
CpData = CP(:,2); % Cp data

%% Interpolate function
ppCp = interp1(tCp,CpData,'spline','pp'); % Make function from data

%% Make chebfun of Cp
Cpf = @(t)ppval(ppCp,t);
Cp = chebfun(Cpf,[Tmin Tmax],'splitting','on');
cp = Cp(Tg); % Set initial guess at specific heat

%% Import Thermal Conductivity (k) Data
% Data has 10 columns: Col1,3,5,7, 9 = Temperature (K),
% Col2,4,6,8, 10 = k (W/mK) for 22, 37, 56, 115 nm SiNWs
% (Li Appl. Phys. Lett., Vol. 83, No. 14, 6 October 2003).
K = load('kSiTempSizeDepend.txt');
tK22 = K(:,1); % temperature of k data for 22nm SiNW
KData22 = K(:,2); % k data for 22nm SiNW
tK37 = K(:,3); % temperature of k data for 37nm SiNW
```

```
KData37 = K(:,4); % k data for 37nm SiNW
tK56 = K(:,5); % temperature of k data for 56nm SiNW
KData56 = K(:,6); % k data for 56nm SiNW
tK115 = K(:,7); % temperature of k data for 115nm SiNW
KData115 = K(:,8); % k data for 115nm SiNW
tKb = K(:,9); % temperature of k data for bulk Si
KDatab = K(:,10); % k data for bulk Si
kr = [22/2 37/2 56/2 115/2]; % radius in nm
kL = kr/r0;

%% Interpolate functions
ppK22 = interp1(tK22,KData22,'spline','pp');
ppK37 = interp1(tK37,KData37,'spline','pp');
ppK56 = interp1(tK56,KData56,'spline','pp');
ppK115 = interp1(tK115,KData115,'spline','pp');
ppKb = interp1(tKb,KDatab,'spline','pp');

%% Make Chebychev polynomial functions of k using chebfun package
Kf22 = @(t)ppval(ppK22,t);
K22 = chebfun(Kf22,[Tmin Tmax],'splitting','on');
k22 = K22(Tg); % Set initial guess at thermal conductivity for 22nm SiNW
Kf37 = @(t)ppval(ppK37,t);
K37 = chebfun(Kf37,[Tmin Tmax],'splitting','on');
k37 = K37(Tg); % Set initial guess at thermal conductivity for 37nm SiNW
Kf56 = @(t)ppval(ppK56,t);
K56 = chebfun(Kf56,[Tmin Tmax],'splitting','on');
k56 = K56(Tg); % Set initial guess at thermal conductivity for 56nm SiNW
Kf115 = @(t)ppval(ppK115,t);
K115 = chebfun(Kf115,[Tmin Tmax],'splitting','on');
k115 = K115(Tg); % Set initial guess at thermal conductivity for 115nm SiNW
Kfb = @(t)ppval(ppKb,t);
Kb = chebfun(Kfb,[Tmin Tmax],'splitting','on');
kb = Kb(Tg); % Set initial guess at thermal conductivity for bulk Si
```

```
%% Make variables dimensionless
L0 = 1; % Tip of wire
L1 = (r0 + len*tan(theta))/r0; % Base of wire
Lres = (L1-L0)/1000;

%% Import Absorption Coefficient Qabs Data.
% Data has 2 columns: Col1 = NW radius, Col2 = Qabs
Q = load('QabsSiVac532D10D2000A7.txt');
rQ = Q(:,1); % radius of Qabs data
QabsData = Q(:,2); % Qabs data

%% Check if the range of Qabs data is sufficient to include r0 and r1
rminData = min(rQ);
rmaxData = max(rQ);
if r0 < rminData % Check minimum value
    errordlg('Qabs data does not include minimum radius')
    error('Qabs data does not include minimum radius')
end
if r1 > rmaxData % Check maximum value
    errordlg('Qabs data does not include maximum radius')
    error('Qabs data does not include maximum radius')
end
rQd = rQ/r0; % Cast radii to dimensionless

%% Interpolate function
ppQ = interp1(rQd,QabsData,'spline','pp');

%% Make chebfun of Qabs
Qabsf = @(x)ppval(ppQ,x);
Qabs = chebfun(Qabsf,[L0 L1],'splitting','on');

%% Set data storage location
```

```
dataDir = uigetdir(['','Select Data Folder']); % Get the data folder

%% Start While Loop for Temp Dependent Parameters
disp('Starting temperature feedback optimization loop...')
disp(' ')
cntr = 1; % Initiate loop counter
Conv = []; % Initiate convergence tracker
Cntr = []; % Initiate convergence tracker counter
% Make sure average temperature of rod is within 5C of the temperature used
% for thermal constants.
while abs(Tg - AvgT) > 5
    if cntr > 1
        Tg = AvgT; % Set Tg = AvgT
    end

    cp = Cp(Tg); % Set initial guess at specific heat

    k22 = K22(Tg); % Set initial guess at thermal conductivity for 22nm SiNW
    k37 = K37(Tg); % Set initial guess at thermal conductivity for 37nm SiNW
    k56 = K56(Tg); % Set initial guess at thermal conductivity for 56nm SiNW
    k115 = K115(Tg); % Set initial guess at thermal conductivity for 115nm
   SiNW
    kb = Kb(Tg); % Set initial guess at thermal conductivity for bulk Si
    ks = [k22 k37 k56 k115];

    %% Interpolate k vs length function
    kLi = min(kL):(max(kL)-min(kL))/10:max(kL);
    KS = interp1(kL,ks,kLi);

    %% Find best fit to k vs L data
    % Set the fitting options.
    foP = fitoptions('Method','NonlinearLeastSquares',...
        'StartPoint',[15 .75],...
```

```
         'Lower',[0 0],...
         'MaxFunEvals',1e4,...
         'MaxIter',1e4,...
         'TolFun',1e-14,...
         'TolX',1e-14,...
         'Robust','Bisquare');

% Set the fit function for k = k0*(r/r0)^m
Fit = fittype('k.*(L.^m)',...
         'coefficients',{'k','m'},... % What we are optimizing
         'independent','L',... % Dimensionless radial data
         'options',foP); % Include options above.

% Optimize k0 and m
kmfit = fit(kLi',KS',Fit,'problem',m);
% Thermal conductivity and m fit value, J/m*K*sec and unitless
fitparams = coeffvalues(kmfit);
k0 = fitparams(1);
m = fitparams(2);

%% Set Thermal Diffusivity
a0 = k0/(dens*cp); % Thermal diffusivity, m2/sec
a0 = a0*10^(18); % nm2/sec

%% Dimensionless variables
tau0 = ((a0*(tan(theta)^2))/(r0^2))*t0; % Start pulse
tau1 = ((a0*(tan(theta)^2))/(r0^2))*t1; % Start next pulse
taud = ((a0*(tan(theta)^2))/(r0^2))*td; % After pulse
tauw = ((a0*(tan(theta)^2))/(r0^2))*wp; % Pulse width

%% Make chebfun for source function (Eq. 24)
sourcef = @(x) Qabsf(x).*((2*r0m*I0)/(pi*k0*Tb*(tan(theta)^2)))*...
        exp(-(2*(r0^2)*((x-1).^2))./((w0^2)*(tan(theta)^2)));
```

```
sourceP = chebfun(@(x) ((2*r0m*I0)/(pi*k0*Tb*(tan(theta)^2)))*...
    exp(-(2*(r0^2)*((x-1).^2)./((w0^2)*(tan(theta)^2))),[L0 L1]);
source = sourceP.*Qabs;

%% Define S-L Eq (25) in form Au(x) = Lam*Bu(x) in region L0 (tip) to L1 (
base).
x = chebfun('x',[L0 L1]); % Define key variable and region of interest
A = chebop(L0,L1); % Initiate LHS operator A over ROI
A.op = @(x,u) diff(x.^(2+m).*diff(u)); % Define LHS operator A
A.lbc = @(u) diff(u); % Set tip boundary condition
A.rbc = @(u) u; % Set base boundary condition
B = chebop(L0,L1); % Initiate RHS operator B over ROI
B.op = @(x,u) (x.^2).*u; % Define RHS operator B

%% Find eigenvalues and eigenfunctions of S-L operators defined above
[eigFuns,Lams] = eigs(A,B,numEigs); % Retrieve numEigs eigenvalues from
system
[lam,ii] = sort(sqrt(-diag(Lams))); % Lam = -lam^2

%% Find eigenfunctions gn
if isposint(m) % If m is 0 or an integer
    gfun = @(n,x)x.^(-(1+m)/2).*(besselj(-sqrt((m+1)^2)/(m-2),...
        (2/(2-m))*lam(n)*x.^((2-m)/2)) + ...
    (-besselj(-sqrt((m+1)^2)/(m-2),(2/(2-m))*lam(n)*L1^((2-m)/2))/...
    bessely(-sqrt((m+1)^2)/(m-2),(2/(2-m))*lam(n)*L1^((2-m)/2)))*...
    bessely(-sqrt((m+1)^2)/(m-2),(2/(2-m))*lam(n)*x.^((2-m)/2)));
else % If m is not an integer
    gfun = @(n,x)x.^(-(1+m)/2).*(besselj(-sqrt((m+1)^2)/(m-2),...
        (2/(2-m))*lam(n)*x.^((2-m)/2)) + ...
    (-besselj(-sqrt((m+1)^2)/(m-2),(2/(2-m))*lam(n)*L1^((2-m)/2))/...
    besselj(sqrt((m+1)^2)/(m-2),(2/(2-m))*lam(n)*L1^((2-m)/2)))*...
    besselj(sqrt((m+1)^2)/(m-2),(2/(2-m))*lam(n)*x.^((2-m)/2)));
end
```

```
% Initialize eigenfunction matrix 'G'
G = [];
for ind = 1:1:numEigs % For each eigenvalue,
    % Populate eigenfunction matrix 'G'. Each column of G corresponds
    % to the eigenfunction of eigenvalue lam(column).
    G =  horzcat(G,chebfun(@(x) gfun(ind,x),[L0 L1]));
end
g = chebfun(G,[L0 L1]); % Eigenfunctions functions instead of arrays

%% Construct matrix to check gn orthogonality and retreive norms
h = waitbar(0,['Norm Calculation. Loop # ' num2str(cntr) ...
        ': Progress = 0%...']);
NormsNM = ones(numEigs); % Initiate
for r = 1:1:numEigs % For each eigenvalue (n index)
    gn = @(x)gfun(r,x); % gn
    for c = 1:1:numEigs % For each eigenvalue (m index)
        gm = @(x)gfun(c,x); % gm
        % Norm = Square root(integral(x^2*gn*gm))
        gnmNorm = sqrt(sum(chebfun(@(x)x^2*gn(x)*gm(x)...
            ,[L0 L1],'vectorize')));
        NormsNM(r,c) = real(gnmNorm); % Populate matrix with norms
    end
    waitbar((r/numEigs),h,['Norm Calculation. Loop # ' num2str(cntr) ...
        ': Progress = ' num2str((r/numEigs)*100,2) '%...'])
end
close(h)

%% Extract norms of the g eigenfunctions (NormsNM diagonal).
Norms = diag(NormsNM);
% Make normalized NormsNM matrix
uNormsNM = zeros(size(NormsNM)); % Initialize
for c = 1:1:numEigs
    uNormsNM(:,c) = NormsNM(:,c).*(1/Norms(c));
```

```
end

%% Calculate the orthornomal eigenfunctions by dividing g by its norm
u = g./Norms';

%% Find the psi integral (Eq. 34) for each eigenvalue
Psi = size(u); % Initiate
h = waitbar(0,['Psi Calculation. Loop # ' num2str(cntr) ...
        ': Progress = 0%...']);
for ind = 1:1:numEigs % For each eigenvalue,
    % Take the integral of x*orthonoromal eigenfunction*source
    Psi(:,ind) = sum(x.*u(:,ind).*source); % Find psi integral
    waitbar((ind/numEigs),h,['Psi Calculation. Loop # ' num2str(cntr) ...
        ': Progress = ' num2str((ind/numEigs)*100,2) '%...'])
end
close(h)
psi = chebfun(Psi,[L0 L1]); % Make function from array

%% Find ideal time resolutions for simulations
% Find the peak temperature (T @ end of pulse (tauw))
Ttauw = 0; % Initiate dimensionless temperature summation bin
for ind = 1:1:numEigs % For each eigenvalue
    % Sum the dimensionless temperature summation bin with the value
    % of the dimensionless temperature for the eigenvalue.
    Ttauw = Ttauw + ...
        ((1-exp(-tauw*(lam(ind)^2)))*psi(0,ind)*u(1,ind)/(lam(ind)^2));
end
% Set target temperature ratio for the step after the initial step of
% the pulse.
TresD = tauw/200;

% Run loop to find ideal resolution: after
TresA = tauw/200; % Initial guess at time resolution after pulse
```

```
Tratio = 0;
cond = 1;
cnt = 0;
while cond
    Ttau = 0; % Initiate dimensionless temperature summation bin
    for ind = 1:1:numEigs % For each eigenvalue
        % Sum dimensionless temperature summation bin with the value
        % of the dimensionless temperature for the eigenvalue.
        Ttau = Ttau + ...
            (exp(-(tau0+TresA)*(lam(ind)^2))*...
            (1-exp(-tauw*(lam(ind)^2)))*psi(0,ind)*u(1,ind)/(lam(ind)^2));
    end
    % Find the ratio of Ttau to Ttauw
    Tratio = (Ttauw - Ttau)/Ttauw;
    % Check to see if ratio is within the target threshold
    if Tratio < .999
        TresA = TresA*1.5;
        cnt = cnt + 1;
    elseif cnt >= 10000 % If the loop > 100 times, use last TresD
        cond = 0;
        disp('Optimization couldnt find proper resolution.')
    else
        cond = 0;
    end
end

%% Initialize dimensionless temperature matrix and populate
W = L0:Lres:L1; % Dimensionless wire radii array
TempD = []; % Initiate dimensionless temperature matrix for the pulse
TempA = []; % Initiate dimensionless temperature matrix for after

%% Start the pulsed laser heating calculation
tol = .01; % Set temperature difference tolerance to 1%
```

```
Tdiff = 1;
cnt = 0;
Td = []; % Initialize dimensionless time array during pulse
h = waitbar(0,['Pulse Section; Loop # ' num2str(cntr)...
        ': Progress = 0%...']);
for t = tau0:TresD:tauw
    if t > tauw
        t = tauw;
    end
    Td = horzcat(Td,t);
    Ptemp = 0; % Initiate dimensionless temperature summation bin
    for ind = 1:1:numEigs % For each eigenvalue
        % Sum the dimensionless temperature sum bin with the value
        % of the dimensionless temperature for the eigenvalue.
        Ptemp = Ptemp + ...
            ((1-exp(-t*(lam(ind)^2)))*psi(0,ind)*u(W,ind)/(lam(ind)^2));
    end
    TempD(:,cnt+1) = Ptemp'; % Add dimensionless temperature to matrix
    Tlast = Ptemp(1); % Get tip temperature for tolerance comparison
    Tdiff = Ttauw - Tlast; % Temperature difference
    cnt = cnt + 1; % Increment matrix indexer
    waitbar((t/tauw),h,['Pulse Section; Loop # ' num2str(cntr)...
        ': Progress = ' num2str((t/tauw)*100,2) '%...'])
end
close(h)

%% Start the temperature calculation after the laser pulse

tol = .01; % Set temperature difference tolerance to 1%
Tlast = 1;
cnt = 0;
Ta = []; % Initialize dimensionless time array during pulse
Ta2 = []; % Initialize dimensionless time array during pulse
```

```
    coolTime = logspace(log10(wp),log10(t1),500);
    coolTime = coolTime-wp;
    tauC = ((a0*(tan(theta)^2))/(r0^2)).*coolTime;
    szTauC = size(tauC);
    szTauC = szTauC(2);
    h = waitbar(0,['Cooling Section; Loop # ' num2str(cntr)...
            ': Progress = 0%...']);
    for t = tauC
%       for t = tau0:TresA/200:TresA
        Ta = horzcat(Ta,t+tauw);
        Ta2 = horzcat(Ta2,t);
        Ptemp = 0; % Initiate dimensionless temperature summation bin
        for ind = 1:1:numEigs % For each eigenvalue
            % Sum the dimensionless temperature sum bin with the value
            % of the dimensionless temperature for the eigenvalue.
            Ptemp = Ptemp + ...
                (exp(-t*(lam(ind)^2))*(1-exp(-tauw*(lam(ind)^2)))*...
                psi(0,ind)*u(W,ind)/(lam(ind)^2));
        end
        TempA(:,cnt+1) = Ptemp'; % Add dimensionless temperature to matrix
        Tlast = Ptemp(1); % Get tip temperature for tolerance comparison
        cnt = cnt + 1; % Increment matrix indexer
        waitbar((cnt/szTauC),h,['Cooling Section; Loop # ' num2str(cntr)...
            ': Progress = ' num2str((cnt/szTauC)*100,2) '%...'])
    end
    close(h)

    %% Put plots in proper dimensions
    timeD = (Td./((a0*(tan(theta)^2))/(r0^2))).*10^12; % Time in ps
    timeA = (Ta./((a0*(tan(theta)^2))/(r0^2))).*10^9; % Time in ns
    timeA2 = (Ta2./((a0*(tan(theta)^2))/(r0^2))).*10^9; % Time in ns
    tempD = TempD*Tb+Tb; % Pulse temp in K
    tempA = TempA*Tb+Tb; % After pulse temp in K
```

```
    % Join during and after pulse sections together
    if (tauw - Td(end)) < 10*(tauw/TresD)
        cond = 1;
        time = horzcat(timeD/10^3, timeA);
        Time = horzcat(Td,Ta);
        temp = horzcat(tempD, tempA);
        Temp = horzcat(TempD,TempA);
    else
        cond = 0;
    end

    %% Find Average Axial Temperature
    sizeTd = size(Td);
    sizeTd = sizeTd(2);
    indP = sizeTd+1;
    AvgT = mean(temp(1:151,indP));

    %% Populate Convergence Tracker
    Conv = horzcat(Conv,abs(Tg - AvgT));
    Cntr = horzcat(Cntr,cntr);

    %% Update Temperature guess
    disp(['Loop # ' num2str(cntr) ': abs(Tg - AvgT) = '...
        num2str(abs(Tg - AvgT),4) 'C (Tol = 5C)'])

    cntr = cntr + 1;
end

%% Plots
% Cp fit
CPP = figure;
plot(Cp,'k',LW,2)
hold on
```

```
grid on
plot(Tg,cp,'r*',MS,10)
str = ['\leftarrow Cp = ' num2str(cp,2)];
text(Tg+10,cp,str)
title('Cp Data','fontsize',16)
xlabel('Temperature','fontsize',14)
ylabel('Cp (J/gK)','fontsize',14)
legend('Cp Data','Used Cp Value','Location','SouthEast')
hold off

% k fit
K = figure;
plot(K22,'c',LW,2)
hold on
grid on
plot(K37,'b',LW,2)
plot(K56,'g',LW,2)
plot(K115,'r',LW,2)
plot(Kb,'k',LW,2)
plot(Tg,k22,'b*',MS,10)
plot(Tg,k37,'g*',MS,10)
plot(Tg,k56,'r*',MS,10)
plot(Tg,k115,'k*',MS,10)
plot(Tg,kb,'c*',MS,10)
str22 = ['\leftarrow k = ' num2str(k22,3)];
text(Tg+10,k22,str22)
text(Tmax-5,K22(end)+2,'r = 11.0 nm','HorizontalAlignment','right')
str37 = ['\leftarrow k = ' num2str(k37,3)];
text(Tg+10,k37,str37)
text(Tmax-5,K37(end)+2,'r = 18.5 nm','HorizontalAlignment','right')
str56 = ['\leftarrow k = ' num2str(k56,3)];
text(Tg+10,k56,str56)
text(Tmax-5,K56(end)+2,'r = 28.0 nm','HorizontalAlignment','right')
```

```
str115 = ['\leftarrow k = ' num2str(k115,3)];
text(Tg+10,k115,str115)
text(Tmax-5,K115(end)+2,'r = 57.5 nm','HorizontalAlignment','right')
strb = ['\leftarrow k = ' num2str(kb,3)];
text(Tg+10,kb,strb)
text(Tmax-5,Kb(end)+2,'r = bulk','HorizontalAlignment','right')
title({'k Data';['Markers @ T = ' num2str(Tg,3) ' K']},'fontsize',16)
xlabel('Temperature','fontsize',14)
ylabel('k (W/mK)','fontsize',14)
set(gca,'yscale','log')
hold off

% k0 fit
K0 = figure;
plot(kLi,KS,'ko',LW,2)
hold on
grid on
plot(kL,k0*(kL).^m,'r',LW,2)
title({['k0 Fit @ T = ' num2str(Tg,3) ' K']; ...
    ['k0 = ' num2str(k0,4) ' W/mK'];
    ['m = ' num2str(m,4)]},'fontsize',16)
xlabel('Dimensionless R','fontsize',14)
ylabel('k0 (W/mK)','fontsize',14)
hold off

% temp convergence
CONV = figure;
plot(Cntr,Conv,'ko',LW,2)
hold on
grid on
thrsh = 5*ones(size(Conv));
plot(thrsh,'b--')
text(Cntr(1),6,'Threshold = 5 K')
```

```
title('Convergence Tracking','fontsize',16)
xlabel('Loop #','fontsize',14)
ylabel('abs(Tg - AvgT) (K)','fontsize',14)
hold off

% Qabs fit
QABS = figure;
plot(rQd,QabsData,'ko',LW,2)
hold on
grid on
plot(Qabs,'b')
title('Qabs Data','fontsize',16)
xlabel('Dimensionless R','fontsize',14)
ylabel('Qabs','fontsize',14)
hold off

% Source
SOURCE = figure;
plot(source,LW,2);
hold on
grid on
title('Source Profile','fontsize',16)
xlabel('Dimensionless R','fontsize',14)
ylabel('Dimensionless Source','fontsize',14)
hold off

% Eigenvalues
EIGS = figure;
hold on
title('Eigenvalues vs n','fontsize',16)
plot(lam,'.k','markersize',10)
grid on
xlabel('n','fontsize',14)
```

```
ylabel('Lambda(n)','fontsize',14)
hold off

% g
G = figure;
hold on
title('g eigenfunction (Eq. 24)','fontsize',16)
plot(g,LW,2)
grid on
xlabel('Dimensionless R','fontsize',14)
ylabel('g','fontsize',14)
hold off

% g Norms
GNORM = figure;
hold on
title('g Norms','fontsize',16)
plot(Norms,'-ok',LW,1.3,MS,3)
grid on
xlabel('n','fontsize',14)
ylabel('g(n) Norm','fontsize',14)
hold off

% u
U = figure;
hold on
title('u orthonormal eigenfunction (Eq. 29)','fontsize',16)
plot(u,LW,2)
grid on
xlabel('Dimensionless R','fontsize',14)
ylabel('u','fontsize',14)
hold off
```

```
% Orthonormality check of normalized eigenfunctions
ONCHK = figure;
hold on
title('Orthonormality Check','fontsize',16)
surf(uNormsNM)
xlabel('m','fontsize',14)
ylabel('n','fontsize',14)
colormap gray
colorbar
view(90,90)
grid off
hold off

% psi
PSI = figure;
hold on
title('Psi Integral (Eq. 34)','fontsize',16)
plot(psi(0,:),'-ok',LW,1.3,MS,3)
grid on
xlabel('n','fontsize',14)
ylabel('psi','fontsize',14)
hold off

% dimensionless temp rise
THETArise = figure;
hold on
title('Theta During Pulse @ Tip','fontsize',16)
plot(Td,TempD(1,:),'-ok',LW,1.3,MS,3)
grid on
xlabel('Dimensionless Time','fontsize',14)
ylabel('Theta','fontsize',14)
set(gca,'xscale','log')
hold off
```

```
% dimensionless temp cool
THETAcool = figure;
hold on
title('Theta After Pulse @ Tip','fontsize',16)
plot(Ta2,TempA(1,:),'-ok',LW,1.3,MS,3)
grid on
xlabel('Dimensionless Time After Pulse','fontsize',14)
ylabel('Theta','fontsize',14)
set(gca,'xscale','log')
hold off

% actual temp rise
TEMPrise = figure;
hold on
title('Temperature During Pulse @ Tip','fontsize',16)
plot(timeD,tempD(1,:),'-ok',LW,1.3,MS,3)
grid on
xlabel('Time (ps)','fontsize',14)
ylabel('Temp (K)','fontsize',14)
set(gca,'xscale','log')
hold off

% actual temp cool
TEMPcool = figure;
hold on
title('Temperature After Pulse @ Tip','fontsize',16)
plot(timeA2,tempA(1,:),'-ok',LW,1.3,MS,3)
grid on
xlabel('Time After Pulse (ns)','fontsize',14)
ylabel('Temp (K)','fontsize',14)
set(gca,'xscale','log')
hold off
```

```
if cond
    % dimensionless temp at tip
    THETA = figure;
    hold on
    title('Theta @ Tip','fontsize',16)
    plot(Time,Temp(1,:),'-ok',LW,1.3,MS,3)
    grid on
    xlabel('Dimensionless Time','fontsize',14)
    ylabel('Theta','fontsize',14)
    set(gca,'xscale','log')
    hold off

    % actual temp at tip
    TEMP = figure;
    hold on
    title('Temperature @ Tip','fontsize',16)
    plot(time,temp(1,:),'-ok',LW,1.3,MS,3)
    grid on
    xlabel('Time (ns)','fontsize',14)
    ylabel('Temp (K)','fontsize',14)
    set(gca,'xscale','log')
    hold off
end

lenRes = len/1000;
Len = 0:lenRes:len; % Wire length vector in nm
LenUm = Len./1000; % In um
sizeTd = size(Td);
sizeTd = sizeTd(2);
sizeTa = size(Ta);
sizeTa = sizeTa(2);
plotRes = round(sizeTd/3);
```

```
ind1 = plotRes;
str1 = ['Time = ' num2str(time(ind1)*10^3,3) ' ps'];
ind2 = plotRes*2;
str2 = ['Time = ' num2str(time(ind2)*10^3,3) ' ps'];
ind3 = sizeTd+1;
str3 = ['Time (pulse width) = ' num2str(time(ind3)*10^3,3) ' ps'];
plotRes = ceil(sizeTa/50);
ind4 = sizeTd+plotRes;
str4 = ['Time = ' num2str(time(ind4),3) ' ns'];
ind5 = sizeTd+plotRes*2;
str5 = ['Time = ' num2str(time(ind5),3) ' ns'];
ind6 = sizeTd+plotRes*3;
str6 = ['Time = ' num2str(time(ind6),3) ' ns'];

% axial actual temperatures
WIRE = figure;
hold on
title('Axial Temperature Profile','fontsize',16)
plot(LenUm(1:301),temp(1:301,ind1),LenUm(1:301),temp(1:301,ind2),...
    LenUm(1:301),temp(1:301,ind3),LenUm(1:301),temp(1:301,ind4),...
    LenUm(1:301),temp(1:301,ind5),LenUm(1:301),temp(1:301,ind6),LW,2)
grid on
xlabel('Wire Length (um)','fontsize',14)
ylabel('Temp (K)','fontsize',14)
legend(str1,str2,str3,str4,str5,str6)
hold off

disp(' ')
disp('Finished')
```

A.3 HBM analysis file

```
% This code is used to extract temperatures from QPD photovoltage signals
% acquired during laser trapping experiments by using power spectrum
% and hot Brownian motion analysis. This script assumes that the data was
% acquired while oscillating the piezostage, which results in a spike in
% the power spectrum used to calibrate the signal and obtain absolute
% temperatures.

% Written by Paden Roder
% Pauzauskie NanoOptoMechanical Group
% University of Washington, Department of Materials Science and Engineering
% Created: 06/18/2014
% Last Updated: 02/09/2015

%% Administrative
clear all
close all
warning('off','all') % Turn off warnings
% Change default axes fonts.
set(0,'DefaultAxesFontName', 'Arial')
set(0,'DefaultAxesFontSize', 12)
% Change default text fonts.
set(0,'DefaultTextFontname', 'Arial')
set(0,'DefaultTextFontSize', 12)

%% Open QPD Voltage Trace
% Get folder where data is located
dataLoc = 'C:\Users\PBR\Documents\MATLAB\YLF\Data';
[FileName,PathName] = uigetfile('*.*','Select the QPD Trace File',dataLoc);
open([PathName FileName]);
% Get morphology of the particle
choice = questdlg('Is the particle 1D or 3D?', ...
    'Particle Geometry', ...
```

```
    '3D','1D','3D');
% Handle response
switch choice
    case '3D'
        wire = 0;
        sphere = 1;
    case '1D'
        wire = 1;
        sphere = 0;
end
% Get particle number (for record keeping)
prmt='What is the trial number?: ';
name='Trial number';
numlines=1;
defaultanswer={'1'};
particle=inputdlg(prmt,name,numlines,defaultanswer);
% Get QPD data channel
choice = questdlg('Is this X or Y QPD Data?', ...
    'Data Type', ...
    'X','Y','X');
% Handle response
switch choice
    case 'X'
        type = 0;
        typeS = '-x';
    case 'Y'
        type = 1;
        typeS = '-y';
end
% What is the laser wavelength? (Can replace with other wavelengths)
choice = questdlg('What is the laser wavelength?', ...
    'Laser Wavelength', ...
    '975nm','1020nm','1064nm','1020nm');
```

```
% Handle response
switch choice
    case '975nm'
        laser = '-975nm';
    case '1020nm'
        laser = '-1020nm';
    case '1064nm'
        laser = '-1064nm';
end
% What is the irradiance? (for record keeping, avoid using a period)
prmt='What is the laser irradiance?: ';
name='Irradiance';
numlines=1;
defaultanswer={'-5_27'}; % The '-' is a separator, the '_' replaces decimal
irrad=inputdlg(prmt,name,numlines,defaultanswer);
% What is the surrounding fluid temperature?
prmt='What is the bath temperature (C)?: ';
name='Bath Temperature';
numlines=1;
defaultanswer={'25'}; % Default is 25C
roomTemp=inputdlg(prmt,name,numlines,defaultanswer);

% What is the sample frequency?
sampFreq = 100000; % Sample frequency in Hz

% Input stage oscillation amplitude
if type
    stage = 0.1602; % X-oscillation, in microns
else
    stage = 0.1638; % Y-oscillation, in microns
end

% Input sample time
```

```
sampTime = 3; % 3 second acquisition

%% Get QPD data from figure
h = gcf; %current figure handle
axesObjs = get(h, 'Children');  %axes handles
dataObjs = get(axesObjs, 'Children');
% Get Data
xdata = get(dataObjs, 'XData'); % Time data
ydata = get(dataObjs, 'YData'); % QPD voltage data
close(h);

%% Get the power spectrum
% Take QPD voltage signal and find the power spectrum (x~timesx~*/time)
% using Welch's method. pwelch(signal,# of windows,amount of window
% overlap,# points in the FFT calculation, sampling frequency).
[psdSig0,psdSigFreq0]=pwelch(ydata,max(size(ydata)),...
    max(size(ydata))-1,2^nextpow2(max(size(ydata))),...
    100000); % True PSD/low SNR
[psdSig,psdSigFreq]=pwelch(ydata,max(size(ydata))/4,...
    (max(size(ydata))/4)*.9,2^nextpow2(max(size(ydata))),...
    100000); % Processed PSD/higher SNR

% Get indices when frequency > 15 Hz and < 10 kHz.
minf = 1;
while psdSigFreq(minf) < 15
    minf = minf + 1;
end
maxf = 50000;
while psdSigFreq(maxf) < 2000
    maxf = maxf + 10;
end

% We now find the frequency spike from the piezostage oscillation.
```

```
oscGuess = 32; % Replace this with the oscillation frequency
startInd = 1;
while psdSigFreq0(startInd) < oscGuess
    startInd = startInd+1;
end
finInd = startInd + 20;
startInd = startInd-20;
[oscPeak,peakInd] = max(psdSig0(startInd:finInd));
peakID = peakInd+startInd-1; % Peak frequency index
actFreq = psdSigFreq0(peakID); % Actual oscillation frequency

% We need the contribution of the total power of the oscillation peak.
% Ideally, this would be a delta function, however, using the Welch method,
% the spike is broadened over a couple of points. Thus, we need to
% integrate under the curve to get the total power. Using the pwelch method
% parameters above, the peak should be
% around 7 indices wide (+- 3 points).
oscAmp = trapz(psdSig0(peakID-3:peakID+3)); % Total oscillation power

% Find index to help fit
startInD = minf;
while psdSigFreq0(startInD) < actFreq
    startInD = startInD+1;
end
startFitInd = startInD+10;

% Get fit guesses
figure()
loglog(psdSigFreq(minf:maxf),psdSig(minf:maxf)) % Plot PSD
hold on
disp('Click on graph your best guess at the corner frequency.')
[fcGuess,y] = ginput(1);
disp('Click on graph on the flat/constant part where the linear region ends.')
```

```
[fEnd,Sguess] = ginput(1);
hold off
close(gcf);

% We now use that data as starting points for our nonlinear least-squares
% fitting of the Lorentzian.
Dguess = 2*(pi^2)*(fcGuess^2)*Sguess; % Guess for diffusion coefficient (D)
guess = [Dguess,fcGuess]; % Guesses for D and corner frequency

%% Define PSD fit function
% Set the fitting options.
foP = fitoptions('Method','NonlinearLeastSquares',...
    'StartPoint',guess,...
    'Lower',[0,0],...
    'MaxFunEvals',1e4,...
    'MaxIter',1e4,...
    'TolFun',1e-14,...
    'TolX',1e-14,...
    'Robust','LAR');

% Set the fit function. The function is the function described in
% Berg-Sorenson ”Power spectrum analysis for optical tweezers”.
Fits = fittype(@(D,fc,f)...
    (((1 - exp(-(4*pi*fc)/sampFreq))*D)./...
    (2*pi*fc*sampFreq*(1 + exp(-(4*pi*fc)/sampFreq) - ...
    2*exp(-(2*pi*fc)/sampFreq)*cos(2.*pi.*f./sampFreq)))),...
    'coefficients',{'D','fc'},... % What we are optimizing
    'independent','f',... % X data
    'options',foP); % Include options above.

output = fit(psdFreq',psdData,Fit);
%% Plot PSD and fit
loglog(psdSigFreq(minf:maxf),psdSig(minf:maxf),'r')
```

```
hold on
Fit = fit(psdFreq',psdData,Fits);
% Get corner frequencies & Diffusion constants from best fit parameters.
Coeff = coeffvalues(Fit);
CoeffI = confint(Fit);
D = Coeff(1);
fc = Coeff(2);
% Fit functional form
psdFunFit = (((1 - exp(-(4*pi*fc)/sampFreq))*D)./...
    (2*pi*fc*sampFreq*(1 + exp(-(4*pi*fc)/sampFreq) - ...
    2*exp(-(2*pi*fc)/sampFreq)*cos(2.*pi.*psdSigFreq(minf:maxf)./sampFreq))));
loglog(psdSigFreq(minf:maxf),psdFunFit,'b')
fitX = psdSigFreq(minf:maxf);
% Help the program fit the data
check = 1;
while check
    % Construct a questdlg with three options
    choice = questdlg('Is the fit good?', ...
        'Goodness of Fit', ...
        'Yes','No','Yes');
    % Handle response
    switch choice
        case 'Yes'
            check = 0;
        case 'No'
            % Exclude noisy low-frequency data if needed.
            msg = msgbox(['Click on points on the graph after the'...
                ' oscillation spike to fit. Then hit Return']...
                ,'Fitting help');
            uiwait(msg);
            X=[];
            Y=[];
            [X,Y] = ginput;
```

```
            % Find index to start concatination
            cat = 1;
            while psdSigFreq(cat) < max(X)
                cat = cat + 10;
            end

            % Concatenate dataset
            fitX = vertcat(X,psdSigFreq(cat:maxf));
            fitY = vertcat(Y,psdSig(cat:maxf));

            % Fit concatenated data
            Fit = fit(fitX',fitY,Fits);

            % Get corner frequencies & D from best fit parameters.
            Coeff = coeffvalues(Fit);
            CoeffI = confint(Fit);
            D = Coeff(1);
            fc = Coeff(2);
            % Plot functional fit
            psdFunFit = (((1 - exp(-(4*pi*fc)/sampFreq))*D)./ ...
                (2*pi*fc*sampFreq*(1 + exp(-(4*pi*fc)/sampFreq) - ...
                2*exp(-(2*pi*fc)/sampFreq)*cos(2.*pi.*fitX./sampFreq))));
            loglog(fitX,psdFunFit,'g')

            check = 1;
    end
end
hold off
close all

%% Calculate calibration coefficient
% Theoretical oscillation power
```

```
Wth = (0.5*((stage*10^(-6))^2))/(1 + ((fc^2)/(actFreq^2)));
% Experimental oscillation power
Wex = oscAmpdiff*(1/sampTime);
beta = sqrt(Wth/Wex); % Beta calibration coefficient in m/V.
% Inverse calibration coefficient in V/um (ballpark ~0.4)
invBeta = (1/beta)*10^(-6);
Dexp = D*(beta^2); % Calibrated D, in m2/s

%% Get size info
if sphere
    % Get sphere radius (nm)
    prmt={'What is the particle diameter (nm)?: ',...
        'What is the diameter standard deviation (nm)?: '};
    name='Particle Diameter';
    numlines=1;
    defaultanswer={'1010','0'};
    pSize=inputdlg(prmt,name,numlines,defaultanswer);
    % Particle radius in nm
    radM = str2double(pSize(1))/2; % In nm
    radMm = radM*10^(-9); % In m
    % Particle radius standard deviation in nm
    radSD = str2double(pSize(2))/2; % In nm
    radSDm = radSD*10^(-9); % In m
    % Placeholder for temperature calculations
    lenM = 0;
    lenMm = 0;
    % Placeholder for temperature calculations
    lenSD = 0;
    lenSDm = 0;
elseif wire
    % Get wire diameter and length (nm)
    prmt={'What is the particle diameter (nm)?: ',...
        'What is the diameter standard deviation (nm)?: ',...
```

```
        'What is the particle length (nm)?: ',...
        'What is the length standard deviation (nm)?: '};
    name='Particle Size';
    numlines=1;
    defaultanswer={'700','50','3000','100'};
    pSize=inputdlg(prmt,name,numlines,defaultanswer);
    % Particle diameter in nm
    radM = str2double(pSize(1)); % In nm
    radMm = radM*10^(-9); % In m
    % Particle radius standard deviation in nm
    radSD = str2double(pSize(2))/2; % In nm
    radSDm = radSD*10^(-9); % In m
    % Particle length in nm
    lenM = str2double(pSize(3)); % In nm
    lenMm = lenM*10^(-9); % In m
    % Particle length standard deviation in nm
    lenSD = str2double(pSize(4))/2; % In nm
    lenSDm = lenSD*10^(-9); % In m
end

%% Calculate hot Brownian motion temperature
kB = 1.3806488*10^(-23); % Boltzmann constant
T0c = str2double(roomTemp); % Room temperature in C
% Ask what typ of solvent is used
choice = questdlg('What solvent was used?', ...
    'Solvent typ', ...
    'DI','D2O','D2O');
% Set VTF viscosity fit parameters
switch choice
    case 'DI' % H2O
        ninf = (2.721*10^(-5)); % In Pa*s
        A = 528.8; % In K
        Tvft = 146.7; % In K
```

```
        solvent = '-DI';
    case 'D2O'
        ninf = (3.548*10^(-5)); % In Pa*s
        A = 470.1; % In K
        Tvft = 161.3; % In K
        solvent = '-D2O';
end

% Temperature conversions
KtoC = @(T) T - 274.15;
CtoK = @(T) 274.15 + T;

% Viscosity temperature dependence functional form
Visc = @(T) ninf.*exp(A./(T-Tvft)); % VFT equation for viscosity

% Stokes drag geometrical factor
if sphere
    G = @(L,R) (6*pi*R); % For sphere
elseif wire
    G = @(L,R) (4*pi*L)./(log(L./(2*R))+0.84); % For cylinder
end

% Room temperature and viscosity
T0 = CtoK(T0c);
n0 = Visc(T0);

% Dimensionless temperature parameter
Theta = @(T) (T-T0)./(T0-Tvft);
% First order HBM viscosity correction
NhbmFO = @(T) (193/486)*log(n0/ninf).*Theta(T);
% Second order HBM viscosity correction
NhbmSO = @(T) (((56/243)*log(n0/ninf)) - ...
    ((12563/118098)*(log(n0/ninf)^2))).*(Theta(T).^2);
```

```
% HBM viscosity function (FO + SO corrections)
Nhbm = @(T) n0./(1 + NhbmFO(T) - ((2/3).*NhbmSO(T)));
% HBM temperature function (valid for temperature rises < 400 C)
Thbm = @(T) T0 + ((T-T0)/2) + ...
    ((2/3)*((A.*((T-T0).^2))./(12*((T0-Tvft)^2))));

% HBM diffusion coefficient
Dhbm = @(T,L,R) ((kB*Thbm(T))./ ...
    (Nhbm(T)*G(L,R))); % For sphere, In m^2/s
% Classic diffusion coefficient (assuming thermal equilibrium)
Dold = @(T,L,R) ((kB*T)./ ...
    (Visc(T)*G(L,R))); % For sphere, In m^2/s

% Set temperature range to probe for temperature determination
Tc = -100:0.1:400;
Tk = CtoK(Tc);
% Constant diffusion vector for plot. In m^2/s.
DexpV = Dexp*ones(size(Tk));

% Get temperatures
% HBM
% For average radius
[DhbmMin,IhbmMin] = min(abs(DexpV-Dhbm(Tk,lenMm,radMm)));
Tphbm = Tc(IhbmMin);
if radSD || lenSD
    % Minus radius standard deviation
    [DhbmMinSDm,IhbmMinSDm] = ...
        min(abs(DexpV-Dhbm(Tk,lenMm-(lenSDm/2),radMm-(radSDm/2))));
    TphbmSDm = Tc(IhbmMinSDm);
    % Plus radius standard deviation
    [DhbmMinSDp,IhbmMinSDp] = ...
        min(abs(DexpV-Dhbm(Tk,lenMm+(lenSDm/2),radMm+(radSDm/2))));
    TphbmSDp = Tc(IhbmMinSDp);
```

```
end

% Classic
% For average radius
[DoldMin,IoldMin] = min(abs(DexpV-Dold(Tk,lenMm,radMm)));
Tpold = Tc(IoldMin);
if radSD || lendSD
    % Minus radius standard deviation
    [DoldMinSDm,IoldMinSDm] = ...
        min(abs(DexpV-Dold(Tk,lenMm-(lenSDm/2),radMm-(radSDm/2))));
    TpoldSDm = Tc(IoldMinSDm);
    % Plus radius standard deviation
    [DoldMinSDp,IoldMinSDp] = ...
        min(abs(DexpV-Dold(Tk,lenMm+(lenSDm/2),radMm+(radSDm/2))));
    TpoldSDp = Tc(IoldMinSDp);
end

%%% Add data to plots and save
%%% Plot PSD and Fit %%%
PSD = loglog(psdSigFreq(minf:maxf),psdSig(minf:maxf),'k');
hold on
loglog(fitX,psdFunFit,'r')
xlabel('Frequency (Hz)')
ylabel('PSD (V^2/sec)')
if type
    if radSD || lenSD
        title({['Y PSD Data for trial' particle{1}];['D (um^2/s) = ' ...
            num2str(Dexp*10^12) '; Beta (V/um) = ' num2str(invBeta) '.'];...
            ['Troom = ' roomTemp{1} '; Wavelength' laser '; Irrad' irrad{1} ';
    Solvent' solvent];
            ['Thbm = ' num2str(Tphbm) 'C, Thbm+ = ' num2str(TphbmSDp-Tphbm) 'C
  , '...
```

```
             'Thbm- = ' num2str(Tphbm-TphbmSDm) 'C'];['Told = ' num2str(Tpold)
   ...
             'C, Told+ = ' num2str(TpoldSDp-Tpold) 'C, Told- = ' num2str(Tpold-
   TpoldSDm)...
             'C']})
    else
        title({['Y PSD Data for ' particle{1}];['D (um^2/s) = ' ...
            num2str(Dexp*10^12) '; Beta (V/um) = ' num2str(invBeta) '.'];...
            ['Troom = ' roomTemp{1} '; Wavelength' laser '; Irrad' irrad{1} ';
    Solvent' solvent];
            ['Thbm = ' num2str(Tphbm) 'C, Told = ' num2str(Tpold) 'C']})
    end
else
    if radSD || lenSD
       title({['X PSD Data for ' particle{1}];['D (um^2/s) = ' ...
            num2str(Dexp*10^12) '; Beta (V/um) = ' num2str(invBeta) '.'];...
            ['Troom = ' roomTemp{1} '; Wavelength' laser '; Irrad' irrad{1} ';
    Solvent' solvent];
            ['Thbm = ' num2str(Tphbm) 'C, Thbm+ = ' num2str(TphbmSDp-Tphbm) 'C
   , '...
             'Thbm- = ' num2str(Tphbm-TphbmSDm) 'C'];['Told = ' num2str(Tpold)
   ...
             'C, Told+ = ' num2str(TpoldSDp-Tpold) 'C, Told- = ' num2str(Tpold-
   TpoldSDm)...
             'C']})
    else
        title({['X PSD Data for ' particle{1}];['D (um^2/s) = ' ...
            num2str(Dexp*10^12) '; Beta (V/um) = ' num2str(invBeta) '.'];...
            ['Troom = ' roomTemp{1} '; Wavelength' laser '; Irrad' irrad{1} ';
    Solvent' solvent];
            ['Thbm = ' num2str(Tphbm) 'C, Told = ' num2str(Tpold) 'C']})
    end
end
```

```
hold off
```

Appendix B

MEEP FDTD FILES

B.1 Introduction

Finding solutions of Maxwell's equations can be a pestiferous task and it is often the case that there is no analytical solution. Therefore, determining how light interacts with materials and generates internal electric fields necessitates the use of numerical methods. To simulate light-matter interactions, a free finite-difference time domain (FDTD) package called MEEP (which stands for MIT Electromagnetic Equation Propagation) was used for its robust capabilities to simulate 1-dimensional, 2-dimensional, and 3-dimensional problems. MEEP has capabilities to treat anisotropic, dispersive, and nonlinear media with electric and magnetic conductivities. This appendix chapter includes tutorial files and instructions for using MEEP with the Linux distribution on the Pauzauskie simulation PC.

The control file (with extension .ctl) is what MEEP reads and uses during a simulation. However, it is convenient to interface with the control file via a bash script which allows for running of multiple simulations, parameter sweeping, and post-processing and saving of each simulation. The following sections include instructions for using these files on the Linux distribution on the Pauzauskie simulation PC, a commented tutorial control file and a corresponding script file.

B.2 Operation instructions

1. To read and run the MEEP tutorial files, open up a terminal (Applications → Accessories → Terminal).
2. Type 'ls' (without the apostrophes) in the terminal and press enter. This shows the directory you are currently in. You need to navigate to the folder where you either

downloaded or placed the tutorial control (.ctl) and bash script (.sh) files. To do this, type ‘cd foldername’ into the terminal, where the folder name is a folder that was shown after typing ‘ls’ in step 1.

3. Once in the right folder, type ‘ls’ again to check that you can see the .ctl and .sh files are in fact in that folder.

4. Now open these files up in a text editor. I recommend gedit, since it has syntax formatting for MEEP. The formatting needs to be downloaded from the internet, but it should already be installed on the simulation PC.

   (a) To open up the files, type ‘gedit filename.* &’.

      i. If it doesn’t allow you to open the documents, it’s because the privacy settings need to be reset.

         A. To reset this, in the terminal, type: ‘sudo chmod 777 PauzauskieMEEPtutorial.*’, then try to reopen it.

      ii. For the tutorial case, it will look like: ‘gedit PauzauskieMEEPtutorial.* &’

      iii. The * is called a wildcard and will open both the .sh and .ctl files.

      iv. The & tells the terminal to open this program in the background, allowing you to keep using the terminal.

5. With both files open in gedit (two tabs should be open up top), start by reading through both the bash script file (PauzauskieMEEPtutorial.sh) and the control file (PauzauskieMEEPtutorial.ctl), in that order, before running the bash script and performing a simulation.

B.3 Processing script file

```
#!/bin/bash

# This script is meant to be used for tutorial purposes. Feel free to use this as a template, but don't save over this file.

# This is a bash script that automatically runs, updates, and analyzes a control file (.ctl) that is read by MEEP. I'll comment step-by-step through this code for instructional purposes.

# NOTE1: If you create a new bash script, or control file, you'll likely need to reset the files' permissions in order to access them. To do so, type: sudo chmod 777 filename.* The asterisk (*) is called a wildcard and it means "Include any file that contains anything before it". Thus, it will include filename.sh and filename.ctl. Also, since 'sudo' is used, it will prompt you for your password. Lastly, the '777' sets open access permission to read and write by anybody. If you'd like to set different permissions, you can read more about the 'chmod' function (or any function) by typing: 'man function' into the terminal. 'man' stands for manual. In this case, you'd type: man chmod. To exit the manual, press the 'q' button on the keyboard.

# NOTE2: In order for the operating system to recognize that your bash script file (.sh) is what it is, the first line of every script file must be: #!/bin/bash

# NOTE3: A bash script is just like a Matlab script. That is, any line in a bash script you can just as well type line-by-line into the terminal. Bash scripts (like Matlab scripts) just makes it easy to automate a repetitive task.

# NOTE4: Make sure you read through this whole document as well as the tutorial control file (PauzauskieMEEPtutorial.ctl) first before running the
```

```
    script.

# NOTE5: To start the simulation, navigate to the folder of the script and
   control file you'd like to run in the terminal. You can navigate in the
   terminal by typing 'ls' and hitting enter to see where you are currently
   and typing 'cd folder' and hitting enter to move to a folder you see listed
   . When there, type: ./filename.sh and hit enter. In this case, you'd type:
   ./PauzauskieMEEPtutorial.sh

# Written by Paden Roder
# Pauzauskie NanoOptoMechanical Group
# University of Washington Department of Materials Science and Engineering
# Created: 03/19/2014
# Last Updated: 05/28/2015
#----------------------------------------#

# This section will prompt a question in the terminal and wait for the user to
    input an answer. Once an input is entered, it is stored in the variable on
    the right. You can ask for start and stop lengths, radius, index of
   refraction, wavelength, etc.

# Example: read -p 'Question goes here: ' variableName
read -p 'Please enter the name of desired directory WITH QUOTATION MARKS!!! (
   Example: "Directory"): ' directory # This creates the name of the folder
   results are placed.
read -p 'Please enter the same name WITHOUT quotation marks (Example: "
   Directory" -> Directory): ' direct # This is the same, just withough quotes
    (for simplicity).
read -p 'What increments do you want to step the imaginary part of the index
   of refraction of the NW?: ' step # This is asking for resolution of
   refractive index steps.
read -p 'How many runs would you like to take?: ' steps # This is asking how
   many steps at the above resolution to run.
```

```
#——————————————————————————————————————————#

# Now that we have the information that we need, we refer to the variable by
    placing a dollar sign in front of it. We create a variable by making a name
     followed immediately by an equal sign.

mkdir $direct # Make a directory in the current folder you are in (named using
     the name you gave it above) to place the results.

holder=0 # This creates a variable called 'holder' as a place holder for our
    while loop.
#——————————————————————————————————————————#

# Below is the start of a while loop. It asks the question "If $holder is less
     than the number of steps we're supposed to increment, then do what's below
     it. You can put whatever conditional statement you want to test for in the
     while loop.
while test $holder -lt $steps
do
#——————————————————————————————————————————#

# This is the line that runs your MEEP control file. The syntax is: meep
    meepVariable1=value1 meepVariable2=value2 ... meepVariableN=valueN filename
    .ctl | tee outputFile.out

# The 'meepVariableN' is a variable that is present in your control file. This
     is nice, since this allows you to update the variables between runs in the
     while loop without having to manually go into the control file to update
    it. Any variable defined in the control file can be changed here.

# The 'valueN' can either be a numerical value, string, or script variable.
    Example: meepVariableN=1 or meepVariableN=$scriptVariable
```

```
# The output file (.out) is where all of the information from the simulation
    gets dumped into. So, information like how long the simulation took,
    absorption and scattering coefficients using flux planes, etc.
meep output_directory=$directory holder=$holder step=$step
    PauzauskieMEEPtutorial.ctl | tee PauzauskieMEEPtutorial.out
#———————————————————————————————————————#

# This section simply outputs text or values to the terminal screen. "" is
    simply a new line.
echo ""
echo "Simulation finished. Moving results to proper folder..."
echo ""
#———————————————————————————————————————#

# This section creates folders and moves files generated from the simulations.

# In this case, the folder that contains the script and control file for this
    tutorial is: ~/MEEP/Scheme/Tweezer/Tutorial. This is where I would start
    the simulation from. NOTE: the '~' just means whatever account you are
    logged on to's home directory.

# The 'cd' says go to the following directory. In this case, the directory is
    the script variable we prompted the user to supply above. If this tutorial
    file is moved out of this directory, simply replace the preceding directory
     to wherever you have the tutorial files located. Example: If you moved the
     tutorial files to a folder on your Desktop called 'MEEPtutorial', then the
     line would read: cd ~/Desktop/MEEPtutorial/$direct/
cd ~/MEEP/Scheme/Tweezer/Tutorial/$direct/

# Within this folder, make a new folder that will hold all the output files
    from this step in the while loop. I've named it here such that I can easily
     identify which step in the loop it corresponds to.
mkdir "step=$holder*steps=$step"
```

```
cd ~/MEEP/Scheme/Tweezer/Tutorial/ # Move back to your starting directory.

# In the corresponding control file, you can elect to output data files that
    contains data such as the x-, y-, and z-components of the electric field,
    as well as the energy density. Here, we move all of those data files, as
    well as the output file, to the subfolder we created above.

# NOTE: The syntax is: mv file1.extension file2.extension ... fileN.extension
    finalFolderDirectory

# NOTE: In the corresponding control file, you choose the name of the output
    files. For instance, I've chosen to name the x-component of electric field
    as 'Ex'. The file type it saves as is a Hierarchical Data Format (HDF5),
    which has the extension '.h5' (this file can be read by Matlab, FYI). MEEP
    always saves its output data as: controlFilename-
    outputNameSpecifiedInControlFile.h5

# NOTE: The file with the (-eps-*) is the data files that represent the
    dielectric constants of the materials in the simulation space.
mv PauzauskieMEEPtutorial.out PauzauskieMEEPtutorial-Ez.h5
    PauzauskieMEEPtutorial-Ey.h5 PauzauskieMEEPtutorial-Ex.h5
    PauzauskieMEEPtutorial-eps-* PauzauskieMEEPtutorial-EF-Energy-Density.h5 ~/
    MEEP/Scheme/Tweezer/Tutorial/$direct/step=$holder*steps=$step

# This relocates you into the subfolder your made for the simulation results.
cd ~/MEEP/Scheme/Tweezer/Tutorial/$direct/step=$holder*steps=$step
#-----------------------------------------------------------#

# Again, this lets you know that the simulation is done, the files have been
    moved, and it is now time to analyze the results.
echo ""
echo "Making .png files"
echo ""
```

```
#--------------------------------------------------------------------#

# As mentioned above, the .h5 files that are output can be opened in Matlab
    and subsequent 2D/3D/time dependent plots can be made. However, here, we
    can make our own movies and pictures automatically using software that has
    been installed on the SimPC. For more information on this software, refer
    to the MEEP tutorial online.

# The .h5 file is a 3- or 4-dimensional matrix (depending on if you ran a 2-
    or 3-dimensional simulation, respectively). 2/3 dimensions correspond to
    the spatial dimensions for every time step.

# Here, we use a function called 'h5topng' which converts data in a .h5 file
    to a PNG. For detailed info, type 'man h5topng' in the terminal and hit
    enter. Again, exit the manual by pressing 'q'. For this function, it needs
    to be told which time slices you'd like to turn into .png files. The syntax
     is:

# h5topng -t timeslice0:timesliceN -spatialSlice -colorOptions1 -colorOptions2
     ... -colorOptionsN filename-eps* filename-datafile.h5

# '-t' corresponds to the timeslice. To know how many time steps you have, you
     can look in the output file filename.out

# The '-0x0' says "Take the center x-slice (yz-plane)". The .h5 file will
    index the very first slice in any direction as 0. To make it index the
    center slice as 0, you use '-0'. Then, you need to choose which plane to
    look at. This is chosen using either '-x' (yz-plane), '-y' (xz-plane), or
    '-z' (xy-plane). Directly following the spatial slice, enter which slice
    you'd like to look at (Example: -x 0). So, the shorthand to index the
    center slice as 0, choose the yz-plane, and pick the center slice is '-0x0
    '.
```

```
# The '-R', '-Zc dkbluered', '-a yarg', and '-A' are all aesthetic color
    options for the generated pictures that can be looked up in the manual
    using 'man h5topng'.

# The 'filename-eps*' places an outline of the material in your simulation
    into the picture for aesthetic purposes.

# The 'filename-datafile.h5' is the data file you'd like to make PNG images
    from.

# NOTE: If you don't need images and would rather just look at the results in
    Matlab, you can comment out these lines below by placing a hashtag in front
     of them. This will save a lot of time in the simulation.
h5topng -t 0:95 -0x0 -R -Zc dkbluered -a yarg -A PauzauskieMEEPtutorial-eps*
    PauzauskieMEEPtutorial-Ex.h5 # Looks at x-component of electric field
h5topng -t 0:95 -0x0 -R -Zc dkbluered -a yarg -A PauzauskieMEEPtutorial-eps*
    PauzauskieMEEPtutorial-EF-Energy-Density.h5 # Looks at energy density
#-----------------------------------------------------------#

# Again, this lets you know that the PNG images have been made, and now its
    time to create a movie out of those images.
echo ""
echo "Finished making .png files. Now making .gif movies"
echo ""
#-----------------------------------------------------------#

# Now, we are going to take the images created from each time slice above and
    make a movie from it. The syntax is:

# convert filename-datafile.t*.png gifname.gif

# To learn about the 'convert' function, type 'man convert' into the terminal.
```

```
# The 'filename-datafile.t*.png' part is choosing each time slice image that
    was made above. The h5topng automatically saves the images with the time
    slice appended to the name: filename-datafile.t0.png, filename-datafile.t1.
    png, ... filename-datafile.tN.png Thus, to choose all of them, we use the
    wildcard (*) again.

# NOTE: This part can't be done if you decided to not make any images. In that
     case, you would want to comment out these lines as well by adding hashtags
     before the lines.
convert PauzauskieMEEPtutorial–Ex.t*.png PauzauskieMEEPtutorial–Ex.gif
convert PauzauskieMEEPtutorial–EF–Energy-Density.t*.png PauzauskieMEEPtutorial
    –EF–Energy-Density.gif
#-----------------------------------------------------------------------#

# Again, this lets you know that the movie has been made. Since the images
    take up a lot of space and the movie is usually all that we want anyways,
    we go ahead and simply delete the images. If this is not what you want, you
     can comment out these lines.
echo ""
echo ".gif made. Removing .png images"
echo ""

# These lines simply remove the image files you created above.
rm PauzauskieMEEPtutorial–EF–Energy-Density.t*.png
rm PauzauskieMEEPtutorial–Ex.t*.png

# This line puts you back into the original folder where your control and
    script files are located.
cd ~/MEEP/Scheme/Tweezer/Tutorial/
#-----------------------------------------------------------------------#

# Lastly, this part updates the variable 'holder' by increasing its value by
    one. The new vaule of this variable is then evaluated at the top of the for
```

```
    loop to decide to do another iteration or not.
holder=`expr $holder + 1`
done

# If the for loop is done, this lets you know in the terminal by outputing "
   Done!"
echo "Done!"
echo ""
```

B.4 The .ctl file

```
; This control file is meant to be used for tutorial purposes. Feel
   free to use this as a template, but dont save over this file.

; This is a control file that contains all of the MEEP variables
   and functions for a given simulation. This control file is
   executed by a bash script with the same name
   (PauzauskieMEEPtutorial.sh). Id recommend reading that script
   file first before reading this file. Ill comment step-by-step
   through this code for instructional purposes.

; NOTE1: If you create a new bash script, or control file, you will
   likely need to reset the file permissions in order to access
   them. To do so, type: sudo chmod 777 filename.* The asterisk (*)
   is called a wildcard and it means "Include any file that
   contains anything before it". Thus, it will include filename.sh
   and filename.ctl. Also, since "sudo" is used, it will prompt you
   for your password. Lastly, the "777" sets open access permission
   to read and write by anybody. If you would like to set different
   permissions, you can read more about the "chmod" function (or
   any function) by typeing: "man function" into the terminal.
   "man" stands for manual. In this case, you would type: man
   chmod. To exit the manual, press the "q" button on the keyboard.

; NOTE2: All of the MEEP functions that can be used can be found on
   the MEEP tutorial website under the "Reference" section.
   Moreover, there are plenty of examples of different uses on the
   website as well.
```

```
; NOTE3: All of the variables defined here are the default values.
   As mentioned in the corresponding bash script file, any variable
   defined here can be overriden in the bash script call to meep.

; NOTE4: Make sure you read through this whole document as well as
   the tutorial bash script file (PauzauskieMEEPtutorial.sh) first
   before running the script.

; NOTE5: To start the simulation, navigate to the folder of the
   script and control file you would like to run in the terminal.
   You can navigate in the terminal by typing "ls" and hitting
   enter to see where you are currently and typing "cd folder" and
   hitting enter to move to a folder you see listed. When there,
   type: ./filename.sh and hit enter. In this case, you would type:
   ./PauzauskieMEEPtutorial.sh

; NOTE6: This language used by MEEP is called Scheme. It is a lot
   like LISP. I wont go into the syntax of this language because I
   believe anybody reading this should just be able to reuse/alter
   whatever I have here. However, I do want to mention that math
   operations (+,-,*,/) are performed with the syntax: (operation
   value1 value2 ... valueN). Example: 1 + 1 --> (+ 1 1).

; Written by Paden Roder
; Pauzauskie NanoOptoMechanical Group
; University of Washington Department of Materials Science and
   Engineering
; Created: 03/19/2014
; Last Updated: 05/28/2015
```

```
;;;-----------------------------------;;;

; If you do not define the output_directory in the bash script,
   your files will show up in a folder named "default".
(define-param output_directory "default")

; I have created 2 variables, holder and step, that can be used to
   update whatever parameter you wish through the bash script. For
   instance, in the bash script, if you wanted to update the
   imaginary index of refraction for each iteration in the while
   loop, you could update the value of "holder" and "step" after
   the meep call.
(define-param holder 0)
(define-param step 0)
;;;-----------------------------------;;;

; This section defines the material properties to be used in the
   simulation. Again, all of these parameters can be changed in the
   bash script. These are just default values.

; NOTE: MEEP has weird units. Essentially, you need to just pick a
   unit and stay consistent with those units. For more information,
   see the MEEP tutorial website.
(define-param r 50)                                 ; Radius of
   NW in nm
(define-param len 5000)                             ; Length of
   NW in nm
(define-param n 3.60142)                            ; Real part
   of index of refraction for Si @ 980 nm
```

```
(define-param k .00054377)                                     ; Imaginary
   part of index of refraction for Si @ 980 nm
; "k_use" is set up like this as an example of how you can update
   the imaginary refractive index by changing the vaules of
   "holder" and "step" from the bash script. If the default values
   are kept, "k_use" equals "k"
(define-param k_use (+ k (* holder step)))
(define-param eps_real_mat (- (* n n) (* k_use k_use))) ; Real part
   of dielectric constant
(define-param eps_imag_mat (* 2 n k_use))                      ; Imaginary
   part of dielectric constant
(define-param n_env 1.33)                                      ; Index of
   refraction of trap environment
;;;-----------------------------------;;;

; This section defines the EM source properties in the simulation.
(define-param wvlen 980)                                       ; Vacuum
   wavelength of source
(define-param fcen (/ 1 wvlen))                                ; Vacuum
   frequency of source
; NOTE: Make sure you read the MEEP tutorial website about how MEEP
   handles things like wavelength, frequency, and irradiance.
   Essentially, a lot of constants are dropped and values are
   normalized to the source.
;;;-----------------------------------;;;

; This section defines the simulation space.
(define-param s_xy 150)                                        ; Size of
   cell in x & y dimensions
```

```
(define-param s_z 8000)                                   ; Size of
   cell in z dimension

; In general, the thickness of the PML should be at least the
   wavelength of the light you are using in the simulation.
(define-param tpml 1000)                                  ; Thickness
   of the perfectly matched layer (PML)
;;;-----------------------------------------;;;

; Now that we have defined all of our parameters, we can start
   setting up the simulation. Here, we set up the lattice.
(set! geometry-lattice (make lattice (size s_xy s_xy s_z))) ; Set
   the size of the simulation box (size x y z).

(set! default-material (make medium (index n_env))) ; Set the index
   of refraction of that simulation box.

; Now we add whatever type of particle we want in the simulation
   box. If you look on the MEEP tutorial website, there are
   predifined geometries you can use, such as "block" and "sphere".
   Each type has its own syntax, so make sure you look it up before
   using it. Moreover, you can make porous/interesting materials by
   setting up a shape, and then "punching holes" through that shape
   by defining smaller cylinders or spheres within the main
   geometry with properties the same as the surrounding mediums
   properties.

;Make a cylinder at the center of the simulation box. Default long
   axis is along Z.
```

```
(set! geometry  (list (make cylinder (center 0 0 0) (radius r)
   (height len)
  (material (make medium (epsilon eps_real_mat) ; Give it proper
   material properties.
  (D-conductivity (/ (* 2 pi fcen eps_imag_mat) eps_real_mat))
)))))
; NOTE: MEEP assumes no absorption (k=0). To program in the
   imaginary index of refraction, you need to set the electrical
   conductivity with the real and imaginary dielectric constants at
   that frequency, as shown above.

; Now we place the PML layers. You can either just specify a
   thickness (which places PML layers on all sides of the
   simulation box), or you can pick which sides to put the layers
   on. The "direction" and "side" functions are specifying that I
   want PMLs on the bottom (-Z) and top (+Z) of the simulation box.
(set! pml-layers (list (make pml (thickness tpml) (direction Z)
   (side Low) (side High))))

; Here we set our source of the EM fields that we are simulating. I
   am showing a continuous source here, but a pulsed source can
   also be used (see MEEP tutorial website for details). Also, the
   source can be over a range of frequencies instead of being
   monochromatic. Here we just use one wavelength. Lastly, make
   sure that your source is not buried inside of a PML, or no
   radiation will make it out.

; NOTE: According to Maxwells equations, EM waves correspond to
   oscillations of charges. The source is essentially a metal
```

```
   plate/wire that oscillates charges at the desired frequency.
(set! sources (list
               (make source
                 (src (make continuous-src      ; Continuous source
           (frequency fcen)))             ; Monochromatic
                 (component Ex)             ; Polarization
     (center 0 0 (* (- (/ s_z 2) tpml) (- 1 2)))    ; Where is the
   source placed in the simulation box
     (size s_xy s_xy 0)          ; Size of the source (size x y z).
   In this case, a xy-plane.
)))

; If your source, simulation box, and particle all have a type of
   symmetry, a great amount of time can be saved by specifying the
   type of symmetry it has. The types of symmetry that MEEP
   recognizes can be found on the MEEP tutorial Reference page. If
   you simulation does not have symmetry, this can be commented out.
(set! symmetries (list (make mirror-sym (direction Y))))

; Resolution is given in (pixels)/(distance unit). The larger the
   resolution, the longer it will take. Also, you need to have at
   least >= 8 (pixels)/(wavelength in the highest dielectric).
(set! resolution .4)

; This lets MEEP know you want to deal with real and imaginary
   fields in the simulation. If you do not need this, you can
   comment it out and it will save computation time.
(set! force-complex-fields? true)
;;;-----------------------------------;;;
```

```
; Now that we have set up our simulation, we need to run it. There
   are multiple ways to run the simulation: stopping after a
   certain amount of time (shown here), stopping after a pulse has
   decayed by x%, etc. For more information, see the MEEP tutorial
   website Reference page.
(run-until 100000             ; Run for 100,000 nm --> roughly 100
   wavelengths
  (at-beginning output-epsilon)         ; Output the dielectric
   makeup of the simulation box
  ; At roughly every wavelength of time, output electric field
   components.
  (to-appended "Ex" (at-every 1000 output-efield-x))    ; X
   component, with a data name "Ex"
  (to-appended "Ey" (at-every 1000 output-efield-y))    ; Y
   component, with a data name "Ey"
  (to-appended "Ez" (at-every 1000 output-efield-z))    ; Z
   component, with a data name "Ez"
  ; At roughly every wavelength of time, output the energy density
   (E*E multiplied by a constant).
  (to-appended "EF-Energy-Density"  (at-every 1000 output-dpwr))
)
```